technische universität
dortmund

Non-Stationary Optical Homodyne Tomography

Dissertation

submitted in partial fulfillment of
the requirements for the degree of

Dr. rer. nat.

to the Institute of Physics of the
TU Dortmund University, Germany

by

Johannes Thewes

Dortmund, November 2018

Examination board:

Jun.-Prof. Dr. Marc Aßmann
Prof. Dr. Mirko Cinchetti
Prof. Dr. Gudrun Hiller
Dr. Christian Sternemann

Contents

Summary

The ability to measure the quantum state of light is an important ingredient in the development of photonic quantum technologies such as optical quantum computing or secure quantum communication. A quantum state comprises all information one can have about a quantum system. Since quantum physics is a statistical theory, a quantum state cannot be captured with a single measurement. Therefore, usually, measurements on an ensemble of identically prepared copies of the quantum system under study must be performed for quantum state reconstruction. Optical homodyne tomography (OHT) is a well established technique frequently used to reconstruct the quantum state of a light field. It requires a reference beam, which is called the local oscillator (LO), that is interfered with the signal light field on a beam splitter before being recorded with homodyne detection. For light fields in pure quantum states, OHT reconstructs the full quantum state. Light fields in mixed states, however, consist of a hidden instantaneous state at every instant, but adopt several such states over time due to an unknown coupling to the environment. In such cases, OHT reconstructs the weighted average of all underlying instantaneous states. In an experiment, light fields in pure states provide a fixed phase relationship between the LO and the signal light field, which is required for OHT to reconstruct the complete quantum state. If a signal field is not phase-locked to the LO, for instance in the case of thermal light, the aforementioned averaging takes place. In order to overcome the limitations of stationary OHT with respect to mixed states, this work introduces the technique of non-stationary OHT. It features two additional homodyne detection channels that aim at recording the required phase information. Since these two channels measure the light field's complete Husimi-Q phase space function, including information about its amplitude, time-resolved measurements are possible. They can be achieved by introducing a delay between the original homodyne detection channel and the additional two channels.

First, a stationary OHT setup was developed. Besides its tomographic capabilities, its high acquisition speed allows one to apply it as a fast equal-time second-order correlation function $g^{(2)}(0)$ monitor with a sampling rate of up to 100 kHz. It was used to discover bistabilities and possible multimode emission in the output of a diode laser operated across the threshold region. The results from applying the subsequently developed detector for non-stationary OHT on a thermal light field are twofold: first, by splitting the signal field in multiple parts, additional noise is introduced into the measurement. The detector can be operated close to the theoretical noise limit and successfully revealed the hidden states in the light field closely resembling coherent states. Second, the evolution of these hidden states in time were tracked and can be attributed to dephasing due to inhomogeneous broadening. The successful implementation of non-stationary OHT may support the development of photonic quantum devices and may allow for the complete characterization of arbitrary light fields in amplitude and phase.

Zusammenfassung

Die Möglichkeit, den Quantenzustand von Licht zu messen, ist eine wichtige Komponente in der Entwicklung photonischer Quantentechnologien wie der optischen Quanteninformationsverarbeitung oder der sicheren Quantenkommunikation. Ein Quantenzustand beinhaltet alle Informationen, die jemand über ein Quantensystem besitzen kann. Da Quantenphysik eine statistische Theorie ist, kann ein Quantenzustand nicht mit einer einzelnen Messung ermittelt werden. Deshalb müssen zur Quantenzustandsrekonstruktion üblicherweise Messungen an einem Ensemble identisch präparierter Kopien eines Quantensystems erfolgen. Optische homodyne Tomographie (OHT) ist eine etablierte und oft genutzte Technik, um den Quantenzustand eines Lichtfelds zu rekonstruieren. Sie benötigt einen Referenzstrahl, den Lokaloszillator (LO), der mit dem Signalfeld auf einem Strahlteiler überlagert wird, bevor er homodyn detektiert wird. Für Lichtfelder in reinen Zuständen rekonstruiert OHT den kompletten Quantenzustand. Lichtfelder in gemischten Zuständen bestehen jedoch zu jedem Zeitpunkt aus versteckten instantanen Zuständen und nehmen verschiedene solcher Zustände aufgrund einer unbekannten Wechselwirkung mit der Umgebung an. In solchen Fällen rekonstruiert OHT den gewichteten Mittelwert der zugrundeliegenden instantanen Zustände. Im Experiment stellen Lichtfelder in reinen Zuständen eine feste Phasenbeziehung zwischen dem LO and dem Signalfeld zur Verfügung, die benötigt wird, um mittels OHT den vollständigen Quantenzustand zu rekonstruieren. Die Mittelung findet statt, falls das Signalfeld keine feste Phasenbeziehung zum LO hat, beispielsweise im Fall von thermischem Licht. Um die Grenzen stationärer OHT in Bezug auf gemischte Zustände zu überwinden, wird in dieser Arbeit die Technik der nicht-stationären OHT eingeführt. Sie weist zwei zusätzliche homodyne Detektionskanäle auf, die darauf abzielen, die benötigte Phaseninformation zu messen. Da diese beiden Kanäle die vollständige Husimi-Q Phasenraumfunktion des Signallichts, inklusive der Amplitudeninformation, aufnehmen, sind zeitaufgelöste Messungen damit möglich. Sie können umgesetzt werden, indem eine zeitliche Verzögerung zwischen dem ursprünglichen und den beiden neuen Kanälen eingeführt wird.

Zuerst wurde ein Aufbau zur stationären OHT entwickelt. Zusätzlich zur OHT konnte er aufgrund seiner hohen Geschwindigkeit zur schnellen Beobachtung der gleichzeitigen Korrelationsfunktion zweiter Ordnung $g^{(2)}(0)$ mit Abtastraten bis zu 100 kHz eingesetzt werden. Dies wurde genutzt, um Bistabilitäten und mögliche multiple Moden in der Emission eines Diodenlasers nachzuweisen, der über die Laserschwelle hinweg betrieben wurde. Mit dem nachfolgend entwickelten Detektor zur nicht-stationären OHT konnten zwei Ergebnisse erzielt werden: Erstens wird durch die Aufspaltung des Signallichtfelds in mehrere Teile zusätzliches Rauschen in die Messung eingebracht. Der Detektor konnte nahe an diesem theoretischen Rauschlimit betrieben werden und wir konnten erfolgreich zeigen, dass die im Lichtfeld versteckten Zustände kohärenten Zuständen ähneln. Zweitens wurde die Zeitentwicklung dieser Zustände ermittelt und konnte der Dephasierung aufgrund von inhomogener Verbreiterung zugeordnet werden. Die erfolgreiche Implementierung nicht-stationärer OHT ist ein Schritt hin zur Entwicklung photonischer Quantengeräte und könnte die vollständige Charakterisierung beliebiger Lichtfelder in Phase und Amplitude erlauben.

1. Introduction

The invention of the laser in 1960 [1] marked the starting point of photonics, the science and technical application of light. Today, it is a broad field of research, backing up a well established industry with a global market of EUR 447 billion in revenue in 2015 [2]. Photonics covers a large and diverse range of mature applications such as laser material processing [3], refractive surgery [4], wind field measurements [5], and inter satellite laser communication [6]. Besides these mature applications, mostly using the classical properties of light as an electromagnetic wave, photonics also plays a major role in the emerging field of quantum technologies. In 2016, European scientists argued in the "Quantum Manifesto" that such technologies are expected to lead to transformative applications in the areas of communication, simulation, sensors, and computers [7]. Responding to the "Manifesto", the European quantum technologies flagship programme started in 2018 to support research in quantum technologies with about EUR 1 billion for 10 years, almost twice the amount of about EUR 550 million invested in the 20 years before [8]. Photonic quantum technologies [9] deliberately employ the quantum nature of light and play important roles in all four areas with applications such as optical quantum information processing [10] and quantum key distribution [11].

At their heart, photonic quantum technologies deal with the generation, manipulation, and detection of quantum states of light [9]. By definition, a quantum state contains the maximum amount of information one can have about a quantum system [12]. Therefore, in order to develop and debug photonic quantum devices, researchers and engineers need to reconstruct unknown quantum states from measurements. This process is called quantum state tomography (QST) or, more briefly, quantum tomography [13, 14]. In many advanced applications requiring a highly sensitive optical readout, homodyne or heterodyne detection are the methods of choice. They allow one to measure the phase-resolved field quadratures of even a weak signal light field by first interfering it with a reference light field, the local oscillator (LO), on a beam splitter, and then detecting both output beams with a balanced detector. This approach was used, for instance, in the Laser Interferometer Gravitational-Wave Observatory (LIGO) that found the first observational evidence of a black hole merger [15]. Hence, optical quantum state tomography is often performed using balanced homodyne detection (BHD) by first measuring quadrature statistics on the light field of interest and subsequently reconstructing the underlying quantum state. This process is called optical homodyne tomography (OHT) [16].

Although OHT allows one to perform a complete state reconstruction of light fields in even complex pure states, such as Schrödinger cat states [17, 18], it is not possible to capture the time dependencies present in mixed quantum states by means of this method. Therefore, we refer to it as stationary OHT in this work. An ubiquitous example of a

light field in a pure quantum state is perfectly coherent light from a laser source. An incandescent bulb, in contrast, emits thermal light, which is in a mixed quantum state. Both types of light are closely related, since a thermal state can sometimes be interpreted as a coherent state in phase space changing amplitude and phase over time [19]. For such a thermal light field in a mixed state, stationary OHT results in the ensemble average over all instantaneous states the light field may adopt at any given time and the dynamics of the hidden coherent state remain inaccessible.

This work introduces the technique of non-stationary OHT that allows one to investigate these usually hidden dynamics of light fields. Since most real optical systems are open systems, because they interact with an unknown environment, non-stationary OHT adds a new dimension to quantum state tomography for a large class of quantum systems. For instance, even coherent light from a real laser source has a finite coherence time, and therefore its phase fluctuates on that timescale. Stationary OHT routinely overcomes this problem by deriving signal and LO from the same laser source so that they are stable in phase with respect to each other. Non-stationary OHT circumvents this problem by measuring the relative phase between LO and signal instead of relying on a priori assumptions about the phase. When using a pulsed LO, as in this work, the most challenging scenario is a phase of the signal light field that fluctuates randomly from one LO pulse to the next. Hence, in order to test the capabilities and limitations of the newly introduced non-stationary OHT technique, thermal light is used, because the dynamics of the hidden coherent state appear on the femtosecond timescale, while two LO pulses are delayed by nanoseconds.

Chapters 2 and 3 present the theoretical foundations of OHT in the form of a brief introduction into quantum states of light and the mathematical background of homodyne detection and quantum state reconstruction. Non-stationary OHT can be understood as an extension of stationary OHT. Accordingly, chapter 4 provides the technological details of the stationary OHT setup together with a detailed description of its characteristics. It is possible to use this setup for real time measurements of a light field's equal-time second-order correlation function $g^{(2)}(0)$, which is discussed in detail in chapter 5. The setup was applied to monitor the dynamics of a diode laser operated across the threshold region, which yielded insights into its coherence dynamics. Bistabilities as well as possible multimode emission were identified successfully. The technique of non-stationary OHT is presented in chapter 6. The method's capabilities and limitations are demonstrated with the help of measurements on a light field in a thermal state. There are two main results: First, since the signal light field is split up into two parts for the technique to work, additional quantum noise is introduced in the reconstructed state, and the setup could be operated close to this fundamental limit. Second, the reconstructed hidden quantum state behaves like a coherent state, despite the slightly larger quantum noise, and its temporal dynamics, which are dominated by dephasing, could be retrieved. I anticipate this work to open up the way for complete characterization of arbitrary light fields in amplitude and phase. It may serve as a useful tool in the research and development of future photonic quantum technologies tackling the challenges of an increasingly interconnected world.

2. Quantum States of Light

The primary subject in this thesis is to develop an experimental scheme for **non-stationary optical homodyne tomography**, which measures the quantum states of repetitive optical fields. Before the specific theoretical and experimental implications of that scheme are presented in later chapters, light is introduced as the fundamental and ubiquitous phenomenon under study. In this regard, several models to describe optical fields in the classical and quantum picture are presented. Afterwards, these models are used to explain what is understood as a **quantum state** of light.

2.1. Light as an Electromagnetic Wave

In everyday life, people restrict the term **light** to the visible spectrum of electromagnetic radiation. In the present work, the word light is used more loosely by also including the near-infrared spectrum. Classically, the behavior of electromagnetic radiation is governed by **Maxwell's equations** describing the electromagnetic response of some medium [20, 21]. Surprisingly, there are still solutions to these equations if no free charges or currents are present, which allows for the propagation of light in any medium including vacuum. In that case, we obtain a relationship from Maxwell's equations describing the propagation of electromagnetic waves [21, p. 10]:

$$\nabla^2 \vec{E} = \mu_0 \epsilon_0 \epsilon_r \frac{\partial^2 \vec{E}}{\partial t^2} \tag{2.1}$$

This is a **wave equation** for the electric field vector $\vec{E}$ that depends on time t. The constants are the electric permittivity ϵ_0 of vacuum, the relative permittivity ϵ_r of the medium and the magnetic permeability μ_0 of vacuum. They also define the speed $v = 1/\sqrt{\epsilon_0 \mu_0 \epsilon_r}$ of waves described by this wave equation. In free space ($\epsilon_r = 1$) this results in the **speed of light** $c = 299\,792\,458\,\mathrm{m\,s^{-1}}$ [22].

Typical solutions to this wave equation are transverse oscillating waves where the electric and magnetic fields are perpendicular to each other and to the propagation direction. Figure 2.1, for example, illustrates a wave propagating in the x-direction while the electric field vector $\vec{E}$ is oriented along the z-direction. As described by Maxwell's equations, the magnetic field vector $\vec{B}$ is in this case perpendicular to the electric field vector $\vec{E}$ and therefore oriented along the y-direction. Expressions of the following form are solutions of the wave equation (2.1) for the electric field in the z-direction, but only

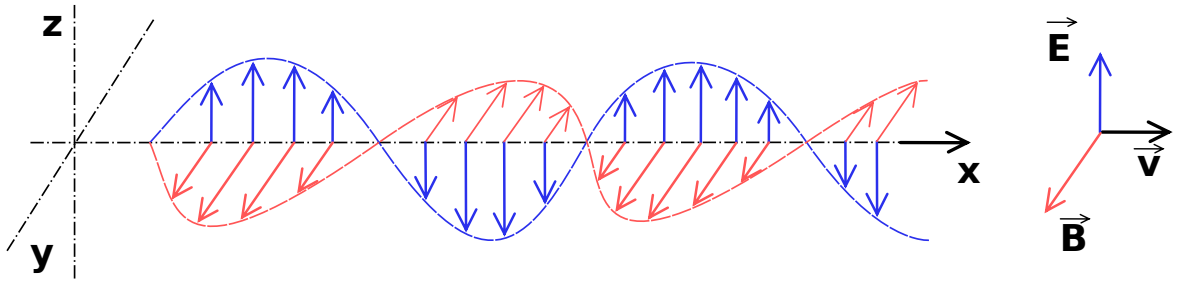

Figure 2.1.: Scheme of a transverse oscillating electromagnetic wave. The electric field vector $\vec{E}$ and the magnetic field vector $\vec{B}$ are perpendicular to each other. Taken from [23].

their real parts are considered as physical solutions (e.g. [21, p. 11]):

$$E_z(x,t) = E_0 e^{i(kx-\omega t+\phi)}, \tag{2.2}$$

$$\mathrm{Re}\left\{E_z(x,t)\right\} = E_0 \cos\left(kx-\omega t+\phi\right). \tag{2.3}$$

The constants are the **amplitude** E_0, the **angular frequency** ω, the wave vector $k = \omega/v$ and the **phase** ϕ of the wave. The complex notation is primarily used in this work, since calculations are easier with it. If there is only one frequency ω present with only small deviations $\Delta\omega$, it is called **monochromatic** light.

2.1.1. Polarization and Coherence

In the previous section, some basics about the wave model of light were introduced. With this model, it is possible to understand two important properties of electromagnetic waves that play a prominent role in later chapters. The first of them is the **polarization** of a light wave, which is simply defined as the direction of its electric field vector. In Fig. 2.1, for instance, the light is polarized along the z-direction and therefore has a well defined **linear** polarization. The other type of polarization referred to is found in **unpolarized** light that is randomly polarized and may include **elliptically** polarized parts where the electric field vector is rotating around the propagation direction [20, p. 267].

The second important property of light is its **coherence**. Real light sources cannot produce waves that are perfectly defined by equation (2.2), because they exhibit technical noise from imperfect parts and also noise due to the quantum nature of light. For example, Schawlow and Townes calculated the fundamental quantum limit for the linewidth of a laser even before the first laser was built [24]. As a result of the additional noise, real light always has some phase distribution $\Delta\phi$, amplitude distribution ΔE_0 and frequency distribution $\Delta\omega$ (also affecting the wave vector k). When the phase ϕ of a light wave can be described by equation (2.2) at time $t = t_1$ and position $x = 0$, it may be predicted for any time $t = t_2$ at the same place. In practice, however, this prediction is not accurate because of the additional noise. The frequency distribution $\Delta\omega$, for example, leads to overlapping waves with different frequencies, that result in a changing phase ϕ over time. Such influences reduce the **coherence time** τ_c, which carries the

Figure 2.2.: Phasor diagrams for (a) an ideal and (b) a noisy classical light field. $\mathcal{E}$ is the complex electric field amplitude.

information that it is possible to predict the wave parameters for times $|t_2 - t_1| \ll \tau_c$ with high certainty.

2.1.2. Field Quadratures

When measuring the properties of light, the number of its free parameters is often reduced. In a typical experiment, some kind of photodetector may be placed at a specific position $x = x_0$ along the propagation direction of the light field that can be described, for example, by equation (2.2). Additionally, its polarization may be fixed by the optical setup and its frequency $\omega = \omega_0$ could already been measured with a spectrometer. This leaves only two free parameters, the amplitude E_0 and the phase ϕ. Equation (2.2) can now be simplified by substituting $\varphi = \phi + kx_0$:

$$E_z(x_0, t) = E_0 e^{i(\varphi - \omega t)} = E_0 e^{i\varphi} e^{-i\omega t} = \mathcal{E} e^{-i\omega t} \tag{2.4}$$

It is helpful to introduce the **phasor diagram** in Fig. 2.2a as a means to visualize any light field with these two free parameters (see for example [21, p. 130]). Shown in this diagram is the newly introduced complex amplitude $\mathcal{E}$ of the time-dependent electric field as a vector in the complex plane. The real and imaginary parts of that amplitude are called the **field quadratures** $\mathcal{E}_1 = \mathrm{Re}\{\mathcal{E}\}$ and $\mathcal{E}_2 = \mathrm{Im}\{\mathcal{E}\}$. By measuring the values of $\mathcal{E}_1$ and $\mathcal{E}_2$ for an ideal light source, it is possible to achieve perfect knowledge of the classical state of the light field. In practice, however, different noise sources impair the measurement, and therefore the quality of the information about the light field. In figure 2.2b, for instance, the presence of such uncertainties is depicted by a circle around the arrow tip that indicates the standard deviation of the measured values. The two field quadratures as well as the variables amplitude and phase are two equivalent ways to describe the same two free parameters of a light field.

2.2. Light as a Harmonic Oscillator

This work is situated in the broader field of **quantum optics**, which deals with the effects resulting from the quantum nature of light. Therefore, it is necessary to understand light within the quantum picture, as well. The transition can be made by first

considering a classical light wave as a harmonic oscillator and then using this knowledge to infer the properties of quantized light from the properties of the quantized harmonic oscillator. The first step can be accomplished because the field quadratures introduced in section 2.1.2 can be mapped onto generalized and dimensionless position q and momentum p coordinates that correspond to the position and momentum variables of a harmonic oscillator (see [21, p. 129 ff.] for details).

In the second step, some important results of treating light as a quantum harmonic oscillator are discussed. As a first result, a light wave can be represented in the **number state representation**. This means, the number of excited energy quanta, the **photons**, are counted instead of using a wave function expressed in position and momentum variables. A monochromatic quantized light field with frequency ω, containing n photons is then described by the photon number state $|n\rangle$. The well known **bosonic creation** and **annihilation operators** $\hat{a}$ and $\hat{a}^\dagger$ of the quantum harmonic oscillator then add or subtract a photon[1]. Next, the **quadrature operators** $\hat{q}$ and $\hat{p}$ can be rewritten[2] in terms of $\hat{a}^\dagger$ and $\hat{a}$:

$$\hat{q} = A\left(\hat{a}^\dagger + \hat{a}\right) \tag{2.5}$$

$$\hat{p} = iA\left(\hat{a}^\dagger - \hat{a}\right) \tag{2.6}$$

In the quantum optics literature, different conventions regarding the commutator $[\hat{q}, \hat{p}]$, which depend on the specific normalization chosen to generalize the electric field quadratures, can be found. The most common conventions are $[\hat{q}, \hat{p}] = i$, $[\hat{q}, \hat{p}] = i/2$, and $[\hat{q}, \hat{p}] = 2i$ (see for example [14, p. 303]). As a reference point for users of different conventions, the real-valued factor A is introduced and used to calculate all quantities of interest in this section. Moreover, the convention $\hbar = 1$ is used throughout this work.

Most of the time, there is no such thing as an absolute phase. Hence, one can often choose an arbitrary phase offset when describing the quantum state of a light field. Therefore it is useful to define general quadrature operators[3] $\hat{q}_\theta$ and $\hat{p}_\theta$ for some phase offset θ by $\hat{q}_\theta = \hat{q}\cos\theta + \hat{p}\sin\theta$ and $\hat{p}_\theta = \hat{q}_{\theta+\pi/2}$. The general quadrature operator $\hat{q}_\theta$ can also be expressed in terms of the annihilation and creation operators:

$$\begin{aligned}\hat{q}_\theta &= \hat{q}\cos\theta + \hat{p}\sin\theta \\ &= A\left\{\hat{a}^\dagger(\cos\theta + i\sin\theta) + \hat{a}(\cos\theta - i\sin\theta)\right\} \\ &= A\left(e^{i\theta}\hat{a}^\dagger + e^{-i\theta}\hat{a}\right)\end{aligned} \tag{2.7}$$

As it turns out, the commutators $[\hat{q}_\theta, \hat{p}_\theta]$ and $[\hat{q}, \hat{p}]$ are the same:

$$\begin{aligned}[\hat{q}_\theta, \hat{p}_\theta] &= [-\hat{q}, \hat{q}]\cos\theta\sin\theta + [\hat{q}, \hat{p}]\cos^2\theta - [\hat{p}, \hat{q}]\sin^2\theta + [\hat{p}, \hat{p}]\sin\theta\cos\theta \\ &= [\hat{q}, \hat{p}]\left(\cos^2\theta + \sin^2\theta\right) = [\hat{q}, \hat{p}]\end{aligned} \tag{2.8}$$

In order to compute $[\hat{q}, \hat{p}]$, the usual commutator

$$[\hat{a}, \hat{a}^\dagger] = 1 \tag{2.9}$$

[1] for a treatment of these ladder operators see for example [25, p. 136 ff.] or [21, p. 151 ff.]
[2] see for example [21, p. 175]
[3] see for example [14, p. 303], [26, p. 279 ff.]

of the bosonic annihilation and creation operators is used:

$$\begin{aligned}[\hat{q},\hat{p}] &= iA^2\left([\hat{a}^\dagger,\hat{a}^\dagger]-[\hat{a}^\dagger,\hat{a}]+[\hat{a},\hat{a}^\dagger]-[\hat{a},\hat{a}]\right)\\ &= i2A^2[\hat{a},\hat{a}^\dagger] = i2A^2\end{aligned} \tag{2.10}$$

A very important quantity describing a light field is the average number $\bar{n} = \langle n|\,\hat{n}\,|n\rangle$ of photons composing the field. An operator that is well known from the harmonic oscillator is the **number operator**[4] $\hat{n} = \hat{a}^\dagger\hat{a}$. It is now possible to express $\hat{n}$ in terms of $\hat{q}$ and $\hat{p}$, which is useful because $\hat{q}$ and $\hat{p}$ are observables that can be measured with the experimental setup presented in chapter 4. To start with, $\hat{a}$ and $\hat{a}^\dagger$ are expressed in terms of the quadrature operators:

$$\hat{a} = \frac{1}{2A}\left(\hat{q}+i\hat{p}\right) \tag{2.11}$$

$$\hat{a}^\dagger = \frac{1}{2A}\left(\hat{q}-i\hat{p}\right) \tag{2.12}$$

Equations (2.11) and (2.12) result from adding and subtracting equations (2.5) and (2.6). Next, $\hat{n}$ can be directly computed:

$$\begin{aligned}\hat{n} = \hat{a}^\dagger\hat{a} &= \frac{1}{(2A)^2}\left(\hat{q}-i\hat{p}\right)\left(\hat{q}+i\hat{p}\right) = \frac{1}{(2A)^2}\left(\hat{q}^2+i\hat{q}\hat{p}-i\hat{p}\hat{q}+\hat{p}^2\right)\\ &= \frac{1}{(2A)^2}\left(\hat{q}^2+\hat{p}^2+i[\hat{q},\hat{p}]\right) \overset{(2.10)}{=} \frac{1}{(2A)^2}\left(\hat{q}^2+\hat{p}^2\right)-\frac{2A^2}{(2A)^2}\\ &= \frac{1}{4A^2}\left(\hat{q}^2+\hat{p}^2\right)-\frac{1}{2}\end{aligned} \tag{2.13}$$

The same relationship holds true for the more general quadrature operators $\hat{q}_\theta$ and $\hat{p}_\theta$, which means that the parameters phase and amplitude of a light field are independent of each other:

$$\begin{aligned}\hat{q}_\theta^2+\hat{p}_\theta^2 &= \left(\cos^2\theta+\sin^2\theta\right)\left(\hat{q}^2+\hat{p}^2\right)+\cos\theta\sin\theta\left(\hat{q}\hat{p}-\hat{q}\hat{p}+\hat{p}\hat{q}-\hat{p}\hat{q}\right)\\ &= \hat{q}^2+\hat{p}^2.\end{aligned} \tag{2.14}$$

With this relationship it is possible to calculate the number of photons in a given light field by performing measurements of $\hat{q}_\theta$ and $\hat{p}_\theta$.

Measurements of **non-commuting** operators like $\hat{q}_\theta$ and $\hat{p}_\theta$, which means that their commutator is not zero, suffer from a fundamental quantum mechanical uncertainty. The two quadrature values of a quantum system cannot both be known at the same time with arbitrary precision. This phenomenon was first discussed by Heisenberg for the position and momentum of a particle [27]. For any pair of non-commuting operators, a general uncertainty principle[5] formalizes this relationship. The uncertainty relation

[4] see for example [21, p. 154]
[5] see for example [28, p. 104] or [29, p. 190]

of $\hat{q}_\theta$ and $\hat{p}_\theta$ is therefore a fundamental constraint on the experiments discussed in this work:

$$\begin{aligned} & \Delta q_\theta \Delta p_\theta \geq \frac{|[\hat{q}_\theta, \hat{p}_\theta]|}{2} \\ \overset{(2.10)}{\Rightarrow} \quad & \Delta q_\theta \Delta p_\theta \geq A^2 \end{aligned} \tag{2.15}$$

Note, if the uncertainty is equally distributed among both quadratures, the factor A is simply the standard deviation of one of the quadratures, for example $\Delta q_\theta = A$. In section 2.1.2, it is emphasized that quadratures are just another way to express the amplitude and phase variables of a light wave. Thus amplitude and phase of a light wave are also subject to a similar uncertainty relationship.

2.3. Quantum Descriptions of Light

In this section, it is stated more formally what is generally understood under a **quantum state** of light. A quantum state contains the maximum amount of information one can have about a quantum system [12]. It is emphasized in the previous section that, in quantum physics, the properties of any physical system, such as a light field, cannot all be perfectly determined at the same time. This is at the core of the statistical nature of quantum physics. The maximum amount of information one can possess about an observable, such as $\hat{n}$, is the statistical distribution of possible measurement outcomes. It is possible that the measurement outcome $\bar{n} = \langle\Psi| \hat{n} |\Psi\rangle$ for some quantum state $|\Psi\rangle$ is exactly the same for each measurement. But then it follows from the uncertainty principle in Eq. (2.15) that it is not possible to know the value of an observable that is not commuting with $\hat{n}$ with any certainty at the same time. In this section, two different ways to represent a quantum state mathematically are introduced along with several examples of quantum states of a light fields.

2.3.1. Wigner Function Formalism

The effects of uncertainties were already discussed on the phasor diagram in section 2.1.2. The uncertainty relation in Eq. (2.15) is one way to describe quantum noise for the quadrature operators $\hat{q}$ and $\hat{p}$ mathematically. Another way is to draw an uncertainty area in a phasor diagram for a quantized light field in analogy to Fig. 2.2b, which is shown in Fig. 2.3a. The two-dimensional plane spanned by the measurement axes q and p is called **phase space**, and it is still possible to talk about an amplitude $|\alpha|$ and a phase ϕ of the light field that correspond to the classical amplitude E_0 and phase φ. If the uncertainty area in Fig. 2.3a is at the quantum limit defined by the uncertainty relation in Eq. (2.15), such a state is called a **coherent state** $|\alpha\rangle$ with the **coherent amplitude** $\alpha = \alpha_r + i\alpha_i = |\alpha|e^{i\phi}$ [21, p. 134].

However, there are some differences to a classical light state. First, the uncertainty relation allows for light states which contain quantum noise that is asymmetrically distributed among conjugate observables. Since amplitude and phase are such a pair of

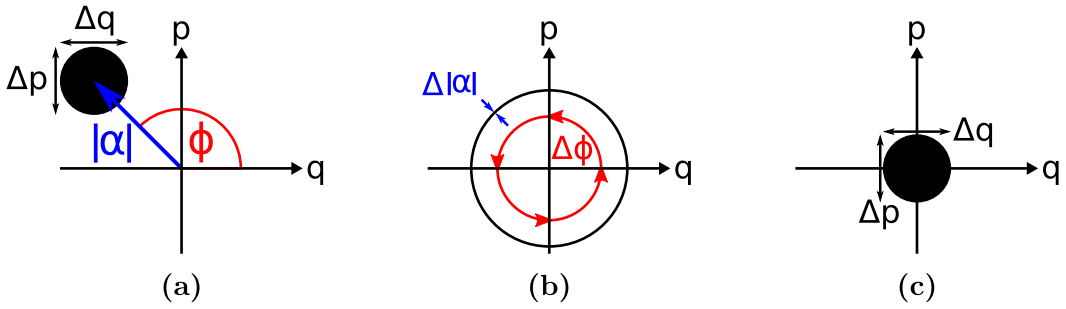

Figure 2.3.: Phasor diagrams for (a) a coherent state, (b) a Fock state, and (c) a vacuum state. Δ indicates the standard deviation of the corresponding variable. α and ϕ are the amplitude and phase of a light state.

conjugate observables, it is possible, for example, to have states with a well defined photon number. Those states are called **photon number states** or **Fock states** [21, p. 139]. Unfortunately, any information about the phase of a Fock state is lost, as depicted in Fig. 2.3b. Secondly, there is also noise present if there is no light at all, shown in Fig. 2.3c. This state is called a **vacuum state** and still carries energy, the **zero point energy** [21, p. 133].

Phasor diagrams are well suited to discuss qualitative differences of quantum states of light and to understand them in the context of amplitude and phase of classical light waves. However, a good theory must also provide quantitative predictions about measurement outcomes. In the case of a classical mechanical system, measuring all generalized coordinates and momenta once at time t_0 and knowing the equations of motion is sufficient to accurately predict the outcome of measurements at times $t > t_0$. In statistical mechanics, incomplete information about such a system is modeled by a statistical ensemble, which consists of identical copies of the actual real system and each copy is in one of all possible states of the real system [30, p. 11 ff.]. The prediction of a measurement is then handled by a probability density function in the phase space spanned by the generalized coordinates and momenta. Since quantum mechanics is also a statistical theory, it is possible to define a similar function in the phase space spanned by conjugate observables of the quantum system under study with similar characteristics. This is the **Wigner function** $W(q, p)$ that was first introduced by Eugene Wigner [31]. It is a complete quantitative description of a light state in the phase space spanned by q and p and a phasor diagram for quantized light can be seen as a two-dimensional projection of the Wigner function. While it is close in meaning to the probability density function in statistical mechanics, there are some major differences.

The similarities between the Wigner function and the phasor diagram can be recognized by comparing the Wigner functions of a coherent state and a vacuum state in Fig. 2.4 with the corresponding phasor diagrams in Fig. 2.3. The two Wigner functions are two–dimensional Gaussian distributions with the same width but different positions in the p–q–plane. The uncertainty areas in the phasor diagrams may be interpreted as circles around the central position with a radius of one standard deviation. However, there are also features of the Wigner function not represented in a phasor diagram. If

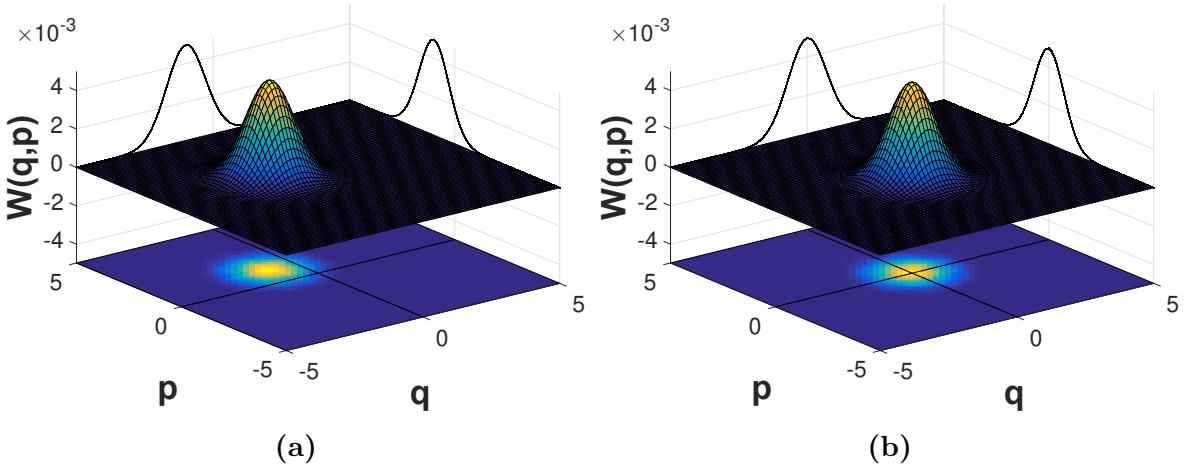

Figure 2.4.: Wigner functions of (a) a coherent state with $n = 1$ photons and (b) a vacuum state with $n = 0$ photons. The integral projections $\mathrm{pr}(q)$ and $\mathrm{pr}(p)$ on the walls are scaled to fit into the plot.

we compare, for example, the Wigner function of a Fock state in Fig. 2.5 with its counterpart in Fig. 2.3b, some differences become apparent. First, the Wigner function is not Gaussian anymore and has negative values at the origin of the p–q–plane. Second, there is no clear interpretation of the uncertainty area in a phasor diagram as a standard deviation. Especially the ability of the Wigner function to have negative values prevents its interpretation as a probability distribution.

Nevertheless, the Wigner function can be interpreted as a **quasiprobability distribution**, because its **integral projections**

$$\mathrm{pr}(q_\theta) = \int W(q,p) dq_{\theta+\pi/2} \tag{2.16}$$

are probability distributions for measurements of the quadrature operator $\hat{q}_\theta$. The projections $\mathrm{pr}(q) = \mathrm{pr}(q_{\theta=0})$ and $\mathrm{pr}(p) = \mathrm{pr}(q_{\theta=\pi/2})$ are shown on the walls of Figs. 2.4 and 2.5. Even though the Wigner function itself can be negative, its integral projections never are. Also, as such integral projections represent probability distributions, the Wigner function has to be normalized to one:

$$\int W(q,p) dq dp = 1 \tag{2.17}$$

The connection between the integral projections of the Wigner function and measurements of the operator $\hat{q}_\theta$ also motivates a scheme to reconstruct the Wigner function of a quantum state from measurements: If it is possible to measure the projections $\mathrm{pr}(q_\theta)$ as histograms from measurements of $\hat{q}_\theta$ on identically prepared copies of the same light field for sufficiently many θ values, it should be possible to reconstruct the underlying Wigner function and therefore the full quantum state of the investigated light field. Another application of the Wigner function is the computation of the overlap of two quantum

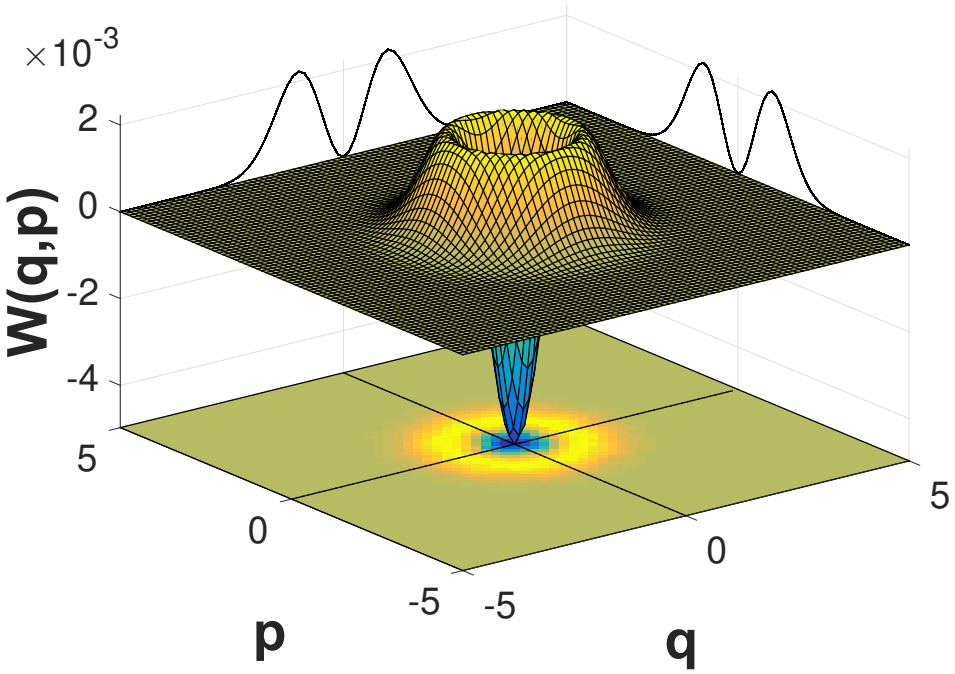

Figure 2.5.: Wigner function of a Fock state with $n = 1$ photons. The integral projections $\mathrm{pr}(q)$ and $\mathrm{pr}(p)$ on the walls are scaled to fit into the plot.

states in phase space. The product between two quantum states $|\Psi\rangle$ and $|\Phi\rangle$ is given by the product of their Wigner functions integrated over phase space [26, p. 71]:

$$|\langle\Psi|\Phi\rangle|^2 = 2\pi \int_{-\infty}^{\infty}\int_{-\infty}^{\infty} W_\Psi(q,p)W_\Phi(q,p)dqdp \tag{2.18}$$

2.3.2. Density Matrix in Fock Basis

The Wigner function is only one of many ways to describe a quantum state of light. Its graphical representation in phase space is very useful to get a phenomenological understanding of the studied quantum state, and the connection of its projections to measurements of the quadrature operator $\hat{q}_\theta$ can be grasped quite intuitively. The second quantitative representation of a quantum state used in this work is the **density operator** $\hat{\rho}$. This section reviews some of its properties and how it is connected to the amplitude and phase of a classical light wave.

If a quantum system can be described by some Hilbert vector $|\Psi\rangle$, it is in a **pure state**, and its density operator is

$$\hat{\rho} = |\Psi\rangle\langle\Psi| \tag{2.19}$$

Pure states only describe completely prepared quantum states where a complete set of commuting observables was already measured. In the general case this information is not available, and another way to represent the available information about such **mixed**

states is needed [29, p. 185 ff.]. This case becomes relevant when not only a single quantum system is considered, but an ensemble of states $\{|\Psi_k\rangle\}$. Such an ensemble can also be in a pure state when all of the constituents are in the same state $|\Psi\rangle$. It is in a mixed state, if they are not all in the same state $|\Psi\rangle$. It is possible to define the probability p_k for a specific quantum system of the ensemble being in the state $|\Psi_k\rangle$. The new density operator is now a weighted sum of pure state density operators[6]:

$$\hat{\rho} = \sum_k p_k \left|\Psi_k\right\rangle \left\langle\Psi_k\right| \tag{2.20}$$

The density operator can now be expressed in any complete orthonormal basis, such as the discrete Fock basis $\{|n\rangle, n \geq 0\}$ [26, p. 47]:

$$\hat{\rho} = \sum_{m,n,k=0}^{\infty} p_k \left|m\right\rangle \left\langle m|\Psi_k\right\rangle \left\langle\Psi_k|n\right\rangle \left\langle n\right| = \sum_{m,n=0}^{\infty} \rho_{m,n} \left|m\right\rangle \left\langle n\right| \tag{2.21}$$

The complex valued factors $\rho_{m,n}$ constitute the **density matrix** of the quantum state in the Fock representation and can completely describe any quantum state of light under study. Since both, the density operator and the Wigner function, are complete representations of light states, they are equivalent to each other. For example, the Wigner function of a light state can be calculated from the density matrix via [26, p. 68]:

$$W(q,p) = \frac{1}{2\pi} \int_{-\infty}^{\infty} \exp\left(-ip\xi\right) \left\langle q + \frac{1}{2}\xi \right| \hat{\rho} \left| q - \frac{1}{2}\xi \right\rangle d\xi \tag{2.22}$$

It is also possible to calculate the expectation value of any operator $\hat{O}$ in a quantum system described by the density operator $\hat{\rho}$ by tracing over their product [26, p. 50]:

$$\left\langle \hat{O} \right\rangle = \mathrm{Tr}(\hat{O}\hat{\rho}) \tag{2.23}$$

As an example, the operator $\hat{O}$ in Eq. (2.23) is replaced by the photon number operator $\hat{n} = \sum_{l=0}^{\infty} l \left|l\right\rangle \left\langle l\right|$:

$$\begin{aligned} \bar{n} = \mathrm{Tr}\left[\hat{n}\hat{\rho}\right] &= \mathrm{Tr}\left[\sum_{l=0}^{\infty} l \left|l\right\rangle \left\langle l\right| \sum_{m,n=0}^{\infty} \rho_{m,n} \left|m\right\rangle \left\langle n\right|\right] \\ &= \mathrm{Tr}\left[\sum_{l,n=0}^{\infty} l\rho_{l,n} \left|l\right\rangle \left\langle n\right|\right] = \sum_{l=0}^{\infty} l\rho_{l,l} \end{aligned} \tag{2.24}$$

The expected photon number $\bar{n}$ is now the sum over terms consisting of the photon number l multiplied with the diagonal element $\rho_{l,l}$ of the density matrix which corresponds to the probability of measuring l photons. This demonstrates two things. First, a clear link

[6] it is assumed that $\langle\Psi_m|\Psi_n\rangle = \delta_{m,n}$, for details see [29, p. 186]

between the diagonal elements of the density matrix of a light field and its amplitude. And second, that the diagonal elements of the density matrix in the Fock basis inform us about the photon statistics of this light field. Therefore, states that carry no phase information, such as Fock states, require only the diagonal of the density matrix to be described. Other states, however, also have non vanishing off–diagonal elements in the density matrix carrying additional information about the phase.

2.3.3. Discrete and Continuous Variables

The quantum variables discussed so far can be divided into two groups: **discrete** and **continuous variables**. Discrete variables, such as the photon number n, only take discrete values, while continuous variables, such as the quadrature q_θ, are real numbered values. It is now possible to choose the description of a quantum state according to what kind of variables are studied. The density matrix ρ_{mn} in the Fock basis, for example, is well suited to study the photon statistics of a quantum state, which are accessible via measurements of discrete variables. The Wigner function, however, is continuous by nature because it lives in the phase space spanned by the continuous quadrature variables p and q.

2.4. Coherent and Thermal States

In the previous sections, a basic foundation to understand quantum states of light was laid and two different methods to describe them were introduced. In this section, two special light states are discussed in more detail: Coherent states and thermal states. Both of them can be created fairly simple and they are used as test states in later chapters.

The term **coherent state** was already mentioned in section 2.3.1 for Hilbert vectors of the form $|\alpha\rangle$ with a complex number $\alpha = \alpha_r + i\alpha_i = |\alpha|e^{i\phi}$. They were first introduced by Erwin Schrödinger in 1926 [32] and are eigenstates of the annihilation operator $\hat{a}$, which means [21, p. 158]:

$$\hat{a}\,|\alpha\rangle = \alpha\,|\alpha\rangle \tag{2.25}$$

Coherent states resemble Gaussian wave packets with minimum uncertainties in both quadratures and are a very good description of light fields from coherent light sources such as lasers.

Next, relationships between the amplitude α of a coherent state $|\alpha\rangle$, the photon number $\bar{n} = \langle\alpha|\,\hat{n}\,|\alpha\rangle$ and the quadrature operator $\hat{q}_\theta$ are derived. First, there is a simple relationship between the number of photons in a coherent state and its amplitude α:

$$\bar{n} = \langle\alpha|\,\hat{a}^\dagger\hat{a}\,|\alpha\rangle = \langle\alpha|\,\bar{\alpha}\alpha\,|\alpha\rangle = |\alpha|^2 \tag{2.26}$$

To find a relationship between $\bar{n}$ and the quadrature operator $\hat{q}_\theta$, some product terms of $\hat{a}^\dagger$ and $\hat{a}$ are necessary. Therefore, the expectation value of $\hat{q}_\theta^2$ is analyzed first as it

includes such terms. $\bar{\alpha}$ is the complex conjugate of α:

$$\begin{aligned}
\langle\alpha|\,\hat{q}_\theta^2\,|\alpha\rangle &= \langle\alpha|\left[A\left(e^{i\theta}\hat{a}^\dagger + e^{-i\theta}\hat{a}\right)\right]^2|\alpha\rangle \\
&= A^2\,\langle\alpha|\,e^{i2\theta}\hat{a}^\dagger\hat{a}^\dagger + \hat{a}^\dagger\hat{a} + \hat{a}\hat{a}^\dagger + e^{-i2\theta}\hat{a}\hat{a}\,|\alpha\rangle \\
&= A^2\,\langle\alpha|\,e^{i2\theta}\hat{a}^\dagger\hat{a}^\dagger + 2\hat{a}^\dagger\hat{a} + 1 + e^{-i2\theta}\hat{a}\hat{a}\,|\alpha\rangle \\
&= A^2\left(\left\langle e^{i2\theta}\right\rangle\bar{\alpha}\bar{\alpha} + 2\bar{\alpha}\alpha + 1 + \left\langle e^{-i2\theta}\right\rangle\alpha\alpha\right) \\
&= A^2\left(2\,|\alpha|^2 + 1 + \bar{\alpha}^2\left\langle e^{i2\theta}\right\rangle + \alpha^2\left\langle e^{-i2\theta}\right\rangle\right) \qquad (2.27)
\end{aligned}$$

In the next step, the expression is simplified by splitting the coherent amplitude α into its absolute value $|\alpha|$ and a constant phase component $e^{i\phi}$. This makes it possible to combine the exponential phase factors:

$$\begin{aligned}
\langle\alpha|\,\hat{q}_\theta^2\,|\alpha\rangle &= A^2\left(2\,|\alpha|^2 + 1 + |\alpha|^2\,e^{-i2\phi}\left\langle e^{i2\theta}\right\rangle + |\alpha|^2\,e^{i2\phi}\left\langle e^{-i2\theta}\right\rangle\right) \\
&= A^2\,|\alpha|^2\left(2 + \left\langle e^{i2(\theta-\phi)}\right\rangle + \left\langle e^{-i2(\theta-\phi)}\right\rangle\right) + A^2 \\
&= 2A^2\,|\alpha|^2\left(1 + \langle\cos\left(2(\theta-\phi)\right)\rangle\right) + A^2 \qquad (2.28)
\end{aligned}$$

This expression can be further simplified by making assumptions about θ. There are two cases of interest for this work:

1. θ is chosen with equal probability in the interval $[0, 2\pi[$. Then, the ensemble average over the cosine term becomes zero and the result is

$$\left\langle\hat{q}^2_{\text{random }\theta}\right\rangle = 2A^2\,|\alpha|^2 + A^2 \qquad (2.29)$$

2. θ has a constant value. The extremal cases then are:

$$\begin{aligned}
\left\langle\hat{q}^2_{\theta=\phi}\right\rangle &= 4A^2\,|\alpha|^2 + A^2 \qquad (2.30)\\
\left\langle\hat{q}^2_{\theta=\phi+\pi/2}\right\rangle &= A^2
\end{aligned}$$

With this knowledge, it is now possible to calculate the photon number of a coherent state from measurements of $\hat{q}_\theta$. The formulas are obtained by applying equation (2.26) to equations (2.29) and (2.30):

$$\bar{n} = \frac{1}{2A^2}\left(\left\langle\hat{q}^2_{\text{random }\theta}\right\rangle - A^2\right) \qquad (2.31)$$

$$\bar{n} = \frac{1}{4A^2}\left(\left\langle\hat{q}^2_{\theta=\phi}\right\rangle - A^2\right) \qquad (2.32)$$

The term A^2 that is subtracted from the averaged squared quadrature values $\langle\hat{q}_\theta^2\rangle$ takes into account the uncertainty and energy of the vacuum state.

Instead of computing $\langle\alpha|\,\hat{q}_\theta^2\,|\alpha\rangle$, the photon number of a coherent state is also accessible by computing the simpler expectation value $\langle\alpha|\,\hat{q}_\theta\,|\alpha\rangle$:

$$\begin{aligned}
\langle\alpha|\,\hat{q}_\theta\,|\alpha\rangle &= \langle\alpha|\,A\left(e^{i\theta}\hat{a}^\dagger + e^{-i\theta}\hat{a}\right)|\alpha\rangle \\
&= A\left(\bar{\alpha}e^{i\theta} + \alpha e^{-i\theta}\right) = A\,|\alpha|\left(e^{-i\phi}e^{i\theta} + e^{i\phi}e^{-i\theta}\right) \\
&= A\,|\alpha|\left(e^{i(\theta-\phi)} + e^{-i(\theta-\phi)}\right) \overset{(2.26)}{=} 2A\sqrt{\bar{n}}\cos\left(\theta-\phi\right) \qquad (2.33)
\end{aligned}$$

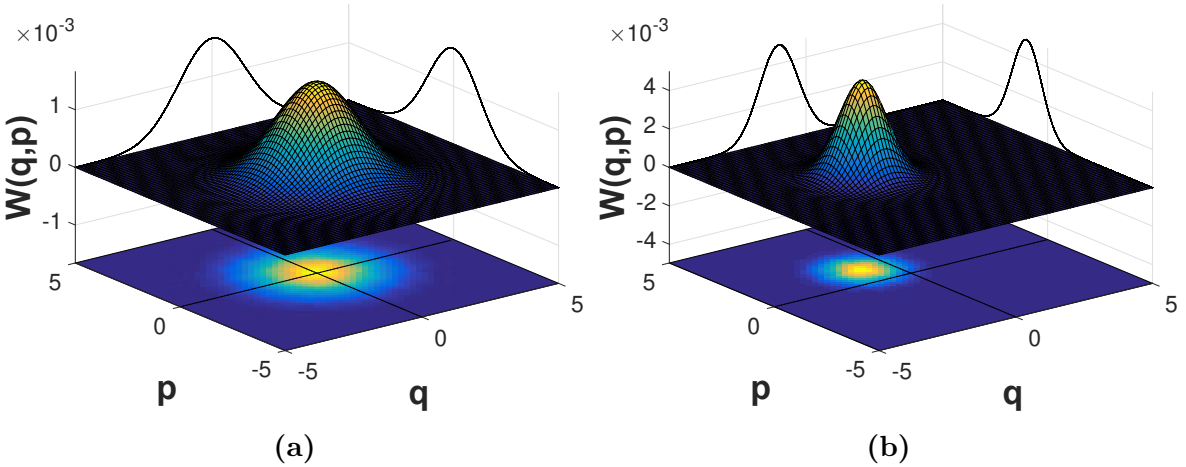

Figure 2.6.: Wigner functions of (a) a thermal state with $n = 1$ photons and (b) a coherent state with $n = 1$ photons. The integral projections $\mathrm{pr}(q)$ and $\mathrm{pr}(p)$ on the walls are scaled to fit into the plot.

This can be solved for $\bar{n}$:

$$\bar{n} = \frac{\langle \hat{q}_\theta \rangle^2}{4A^2 \cos^2(\theta - \phi)} \tag{2.34}$$

For a random phase θ, equation (2.33) is not useful, because the right side $\cos(\theta - \phi)$ becomes zero when averaging over randomly chosen phases. A similar problem appears, when $\theta = \phi + \pi/2$ is chosen. However, for $\theta = \phi$, a meaningful result is obtained:

$$\bar{n} = \frac{\langle \hat{q}_{\theta=\phi} \rangle^2}{4A^2} \tag{2.35}$$

In the Wigner function picture, $\theta = \phi$ means that the plane of the integral projection $\mathrm{pr}(q_\theta)$ is parallel to the vector describing the displacement of the Gaussian coherent state Wigner function from the origin. For $\theta = \phi + \pi/2$, the plane of the integral projection is orthogonal to this displacement. In case of the Wigner function shown in Fig. 2.6b, $\theta = \phi$ would mean that $\theta = \phi = 3\pi/4$. In the rest of this work, the convention $A = 1/\sqrt{2}$ is used.

The second type of quantum states extensively studied in this work is the **thermal state**. It is a good description for **thermal light** from light sources such as light bulbs or lasers operated below the lasing threshold. In contrast to coherent light, thermal light has very low coherence times, typically in the femtosecond regime. The Wigner function of a thermal state with $n = 1$ photons is shown in Fig. 2.6. It is always positive and rotationally symmetric around the z-axis, which means its phase is maximally uncertain, similar to a Fock state. In contrast to a coherent state it is not a minimum uncertainty state but much broader. This is a clear sign that its amplitude and therefore the number of photons is subject to more uncertainty than in a coherent state.

To discuss this uncertainty in amplitude, **photon statistics** of coherent and thermal states can be investigated. If multiple measurements with the photon number operator

$\hat{n}$ are performed, the results n_i are distributed in a certain way. This distribution is called the photon statistics of a light field. For a coherent state, the photon statistics are described by the **Poisson distribution**. This means the probability to measure n photons in a single measurement for a light state with an average photon number of $\bar{n}$ is [21, p. 80]:

$$P(n) = \frac{\overline{n}^n}{n!} e^{-\overline{n}} \tag{2.36}$$

For a Poisson distribution, the variance $(\Delta n)^2$ of the photon number is exactly the average photon number $\bar{n}$ [21, p. 81]:

$$\Delta n = \sqrt{\overline{n}} \tag{2.37}$$

But for a thermal state, the photon statistics are described by the **Bose–Einstein distribution** [21, p. 85]:

$$P(n) = \frac{1}{\overline{n}+1} \left(\frac{\overline{n}}{\overline{n}+1} \right)^n \tag{2.38}$$

This distribution has a larger standard deviation than the Poisson distribution with

$$(\Delta n)^2 = \overline{n} + \overline{n}^2 \tag{2.39}$$

which quantifies the difference in the uncertainties between coherent and thermal states that were already discussed qualitatively.

3. Optical Homodyne Tomography

The previous chapter focused on answering the question what a quantum state of light is and how it can be described. This chapter focuses on the actual methods used to measure the quantum state of a light field. In the framework of this thesis, the well established technique of **optical homodyne tomography** (OHT) is used to measure the quantum state of light. This technique was first suggested by Vogel and Risken [33], first demonstrated by Smithey et al. [34], and makes use of **balanced optical homodyne detection** developed by Yuen and Chan [35, 36]. Balanced homodyne detection allows the direct application of the quadrature operator $\hat{q}_\theta$, introduced in section 2.2, to the light field of interest. With optical homodyne tomography, the measured data points are then used to reconstruct the quantum state of the light field.

3.1. Balanced Homodyne Detection

The basic scheme of balanced homodyne detection is depicted in Fig. 3.1. Its goal is to directly measure the quadrature amplitudes of the **signal light field**. In order to achieve this, the signal light field is first interfered with a strong coherent light field, the **local oscillator (LO)**, by means of a 50 : 50 beam splitter ($BS_{50:50}$) and then detected by two separate photodiodes PD1 and PD2. The photocurrents of the two diodes are finally subtracted to get the difference photocurrent I_- which is subsequently recorded. It is not obvious, but I_- carries information about the signal light amplified by the amplitude of the LO.

The relationship between I_- and the quadrature operator $\hat{q}_\theta$ can be motivated by considering the electric field amplitudes $\mathcal{E}_{\mathrm{SIG}}$ and $\mathcal{E}_{\mathrm{LO}}$ of the signal and local oscillator light fields, respectively[1]. The light fields on the output ports of the beam splitter are:

$$\mathcal{E}_1 = \frac{1}{\sqrt{2}}\left(\mathcal{E}_{\mathrm{LO}} e^{i\theta_{\mathrm{LO}}} + \mathcal{E}_{\mathrm{SIG}}\right) \tag{3.1}$$

$$\mathcal{E}_2 = \frac{1}{\sqrt{2}}\left(\mathcal{E}_{\mathrm{LO}} e^{i\theta_{\mathrm{LO}}} - \mathcal{E}_{\mathrm{SIG}}\right) \tag{3.2}$$

The minus sign in Eq. (3.2) indicates a phase shift of π between the two output ports. This phase shift is a fundamental property of each beam splitter that arises, for example, as a consequence of energy conservation [37]. Since the power of a light beam is proportional to the square of its electric field and a 50 : 50 beam splitter is used, a factor $1/\sqrt{2}$ arises in Eqs. (3.1) and (3.2). The connection to the quadratures can be

[1] the motivation used in this section was taken from [21, p. 141 ff.]

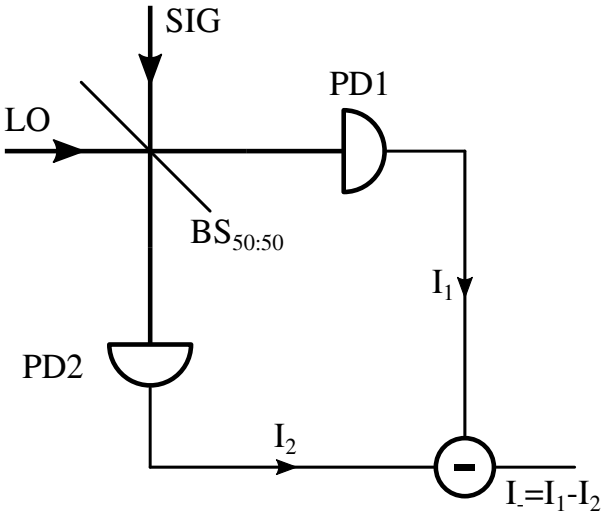

Figure 3.1.: Balanced Homodyne Detection. The signal light field (SIG) is interfered with the local oscillator light field (LO) on a 50 : 50 beam splitter and then detected by two photodiodes PD1 and PD2. Finally, the difference photocurrent of the diodes is recorded. A similar scheme is discussed in [21, p. 139 ff.].

drawn by additionally splitting $\mathcal{E}_{\mathrm{SIG}} = \mathcal{E}^q_{\mathrm{SIG}} + i\mathcal{E}^p_{\mathrm{SIG}}$ into its real and imaginary parts that correspond to the two field quadratures q and p:

$$\mathcal{E}_1 = \frac{1}{\sqrt{2}} \left\{ \left(\mathcal{E}_{\mathrm{LO}} \cos(\theta_{\mathrm{LO}}) + \mathcal{E}^q_{\mathrm{SIG}} \right) + i \left(\mathcal{E}_{\mathrm{LO}} \sin(\theta_{\mathrm{LO}}) + \mathcal{E}^p_{\mathrm{SIG}} \right) \right\} \tag{3.3}$$

$$\mathcal{E}_2 = \frac{1}{\sqrt{2}} \left\{ \left(\mathcal{E}_{\mathrm{LO}} \cos(\theta_{\mathrm{LO}}) - \mathcal{E}^q_{\mathrm{SIG}} \right) + i \left(\mathcal{E}_{\mathrm{LO}} \sin(\theta_{\mathrm{LO}}) - \mathcal{E}^p_{\mathrm{SIG}} \right) \right\} \tag{3.4}$$

The most interesting part of homodyne detection takes place when the light is detected with photodiodes. Since the photodiodes generate photocurrents I_1 and I_2 proportional to the optical power $p = \mathcal{E}\mathcal{E}^* = |\mathcal{E}|^2$ of the electric field[2], the difference photocurrent I_- is proportional to terms linear in $\mathcal{E}_{\mathrm{LO}}$ and $\mathcal{E}_{\mathrm{SIG}}$:

$$\begin{aligned} I_- &\propto I_1 - I_2 \\ &\propto \left|\mathcal{E}_1^2\right| - \left|\mathcal{E}_2^2\right| \\ &\propto 2\mathcal{E}_{\mathrm{LO}} \left(\mathcal{E}^q_{\mathrm{SIG}} \cos(\theta_{\mathrm{LO}}) + \mathcal{E}^p_{\mathrm{SIG}} \sin(\theta_{\mathrm{LO}}) \right) \end{aligned} \tag{3.5}$$

Therefore, the difference current I_- is proportional to the quadrature of the signal field that is in phase with the local oscillator. For example, if $\theta_{\mathrm{LO}} = \pi/2$, then the field quadrature of the signal field corresponding to p is amplified by the LO amplitude $\mathcal{E}_{\mathrm{LO}}$. If homodyne detection is treated quantum mechanically, the qualitative behavior is the same and the quantitative behavior is expressed by a measurement operator $\hat{N}_-$ for homodyne detection in the limit of a strong coherent LO field[3]:

$$\hat{N}_- = |\alpha_{\mathrm{LO}}| \left(e^{i\theta_{\mathrm{LO}}} \hat{a}_S^\dagger + e^{-i\theta_{\mathrm{LO}}} \hat{a}_S \right) \tag{3.6}$$

[2] the star denotes complex conjugation

[3] see, for example, Raymer [38], Lvovsky and Raymer [14], or Roumpos et al. [39]

Here, $\hat{a}_S$ is the annihilation operator of the quantized signal light field and $\hat{a}_S^\dagger$ its creation operator. The amplitude $|\alpha_{\mathrm{LO}}| = \sqrt{N_{\mathrm{LO}}}$ of the LO field is equal to the square root of the number of photons N_{LO} in the field. There is a simple connection between the measurement operator $\hat{N}_-$ and the general quadrature operator $\hat{q}_\theta$ for the signal light field introduced in Eq. (2.7):

$$\hat{q}_\theta = \frac{1}{\sqrt{2}}\left(e^{i\theta}\hat{a}_S^\dagger + e^{-i\theta}\hat{a}_S\right) = \frac{\hat{N}_-}{\sqrt{2N_{\mathrm{LO}}}} \tag{3.7}$$

So far, an outline for the method of balanced homodyne detection used to perform direct measurements with the quadrature operator $\hat{q}_\theta$ was given. In all experiments presented in this work, a pulsed local oscillator is used. Since homodyne detection is based on the interference of the LO and the signal, it is necessary to be careful about the operators in Eq. (3.7). They can only act on the part of the signal field that is able to interfere with the LO field and therefore **overlaps with it spectrally, temporally, spatially and in polarization**. N_{LO} is the average number of photons in a single LO pulse. In the best case, the result of measuring $\hat{q}_\theta$ sufficiently often with a balanced homodyne detection setup is a data set of tuples (Q_i, θ_i) of measured quadratures Q_i and corresponding LO phases θ.

3.2. Reconstruction of the Density Matrix

This section covers the tomographical part of OHT, which means the reconstruction of the complete quantum state of a light field from measurements of $\hat{q}_\theta$. Chapter 2 discussed that, in an experiment, one can only access integral projections of the Wigner function or expectation values calculated from the density matrix. The final goal, however, is to get access to the complete density matrix or Wigner function. Hence, techniques are required to reconstruct them from measurements. For this purpose, the density matrix is always reconstructed first from the measured tuples (Q_i, θ_i) with a **maximum-likelihood algorithm**. The experimentally determined Wigner functions are then calculated from this reconstructed density matrix afterwards.

For the reconstruction of the density matrix, an iterative algorithm is used that was proposed by Alexander Lvovsky in 2004 [40], which is also the source for the information presented in this section, when not indicated otherwise. This maximum-likelihood algorithm aims at computing the density matrix of the quantum state that most likely produced the measured data. Initially, for a given data set $\{(Q_i, \theta_i), i \in \{1, .., N\}\}$ with N data points, a likelihood function $\mathcal{L}(\hat{\rho})$ is needed that provides the probability of measuring exactly this data set for a given quantum state $\hat{\rho}$. Additionally, an algorithm is needed that maximizes this likelihood function iteratively by generating density matrices of quantum states with a higher likelihood.

The likelihood function $\mathcal{L}$ is simply a product of the probabilities $\mathrm{pr}_{\theta_i}(Q_i)$ to measure

the quadratures Q_i at corresponding phases θ_i:

$$\mathcal{L}(\hat{\rho}) = \prod_{i=1}^{N} \mathrm{pr}_{\theta_i}(Q_i) \tag{3.8}$$

When the system is in the quantum state $\hat{\rho}$, these probabilities can be written as expectation values of the pure state $|Q_i, \theta_i\rangle$ describing a measurement outcome:

$$\mathrm{pr}_{\theta_i}(Q_i) = \langle Q_i, \theta_i | \, \hat{\rho} \, | Q_i, \theta_i \rangle = \mathrm{tr}\left(\hat{\Pi}(Q_i, \theta_i)\hat{\rho}\right) \tag{3.9}$$

In the last step, the expectation value property of the density operator from Eq. (2.23) was used and the projection operator $\hat{\Pi}(Q_i, \theta_i) = |Q_i, \theta_i\rangle \langle Q_i, \theta_i|$ was introduced.

Each iteration step of the algorithm starts with an initial density operator $\hat{\rho}^{(k)}$ and computes the next density operator $\hat{\rho}^{(k+1)}$ by

$$\hat{\rho}^{(k+1)} = \mathcal{N}\left[\hat{R}(\hat{\rho}^{(k)})\hat{\rho}^{(k)}\hat{R}(\hat{\rho}^{(k)})\right] \tag{3.10}$$

with the help of the **iteration operator** $\hat{R}(\hat{\rho})$:

$$\hat{R}(\hat{\rho}) = \sum_i \frac{\hat{\Pi}(Q_i, \theta_i)}{\mathrm{pr}_{\theta_i}(Q_i)} \tag{3.11}$$

The normalization operation $\mathcal{N}[\ldots]$ ensures that the trace of the resulting density operator is always 1. $\widetilde{\rho}$ denotes the density operator before the normalization:

$$\mathcal{N}(\widetilde{\rho}) = \frac{\widetilde{\rho}}{\mathrm{tr}\,\widetilde{\rho}} \tag{3.12}$$

So far, this algorithm is suitable for any density operator $\hat{\rho}$. To perform the reconstruction of the quantum state numerically, density matrices are represented in the Fock representation. Since the corresponding Hilbert space is of infinite dimension, the algorithm ignores Fock terms above a cutoff photon number n_{co}. The projection operator $\hat{\Pi}(Q_i, \theta_i)$ in the Fock basis is given by

$$\Pi_{mn}(Q_i, \theta_i) = \langle m | \, \hat{\Pi}(Q_i, \theta_i) \, | n \rangle = \langle m | Q_i, \theta_i \rangle \langle Q_i, \theta_i | n \rangle \tag{3.13}$$

where the overlap of quadrature and number eigenstates is given by the stationary solution of the Schrödinger equation for a particle in a harmonic potential:

$$\langle n | Q_i, \theta_i \rangle = e^{in\theta_i} \underbrace{\left(\frac{1}{\pi}\right)^{\frac{1}{4}} \frac{H_n(Q_i)}{\sqrt{2^n n\,!}} \exp\left(-\frac{1}{2}Q_i^2\right)}_{:=F_n(Q_i)} \tag{3.14}$$

The symbol H_n denotes the Hermite polynomials. Equation (3.14) is slightly different from the one introduced by Lvovsky [40]. In his paper, he uses the commutator convention $[\hat{q}, \hat{p}] = i/2$, while the convention $[\hat{q}, \hat{p}] = i$ is used in this work. Equation (3.14)

is also numerically unstable for higher values of n, because the faculty $n!$ becomes very large very quickly. To keep the computation numerically stable until higher values of n, the value of $F_n(Q_i)$ can be calculated via the following recurrence relation[4]:

$$F_0(Q_i) = \pi^{-\frac{1}{4}} \exp\left(-\frac{x^2}{2}\right) \tag{3.15}$$

$$F_1(Q_i) = \sqrt{2}\, Q_i\, F_0(Q_i) \tag{3.16}$$

$$F_{n>1}(Q_i) = \sqrt{\frac{2}{n}}\, Q_i\, F_{n-1}(Q_i) - \sqrt{\frac{n-1}{n}}\, F_{n-2}(Q_i) \tag{3.17}$$

The source code used to perform the density matrix reconstruction and most of the data analysis presented in this work can be found in an open source MatLab toolbox [42].

3.3. Computing the Wigner Function

Since the Wigner function and the density operator are equivalent descriptions of quantum states of light, it is possible to calculate one from the other. The Wigner function $W(q,p)$ corresponding to a quantum state $\hat{\rho}$ was already introduced in Eq. (2.22). To treat this conversion numerically, however, the equation needs to be adapted. Since the Fock basis is a complete orthonormal basis, the identity operator can be written as a sum of Fock projectors:

$$\mathbb{1} = \sum_{n=0}^{\infty} |n\rangle \langle n| \tag{3.18}$$

Adding two identity operators in Eq. (2.22) results in a more useful formula:

$$\begin{aligned} W(q,p) &= \frac{1}{2\pi} \int_{-\infty}^{\infty} \exp(-ip\xi) \left\langle q + \frac{1}{2}\xi \right| \mathbb{1}\hat{\rho}\mathbb{1} \left| q - \frac{1}{2}\xi \right\rangle d\xi \\ &= \frac{1}{2\pi} \sum_{m,n=0}^{\infty} \int_{-\infty}^{\infty} \exp(-ip\xi) \left\langle q + \frac{1}{2}\xi \middle| m \right\rangle \left\langle m \middle| \hat{\rho} \middle| n \right\rangle \left\langle n \middle| q - \frac{1}{2}\xi \right\rangle d\xi \\ &= \frac{1}{2\pi} \sum_{m,n=0}^{\infty} \rho_{mn} \int_{-\infty}^{\infty} \exp(-ip\xi) \left\langle q + \frac{1}{2}\xi \middle| m \right\rangle \left\langle n \middle| q - \frac{1}{2}\xi \right\rangle d\xi \\ &= \sum_{m,n=0}^{\infty} \underbrace{\rho_{mn}}_{(I)} \cdot \underbrace{\frac{1}{2\pi} \mathcal{FT}\left(\left\langle q + \frac{1}{2}\xi \middle| m \right\rangle \left\langle n \middle| q - \frac{1}{2}\xi \right\rangle \right)}_{(II)} \end{aligned} \tag{3.19}$$

Equation (3.19) is a numerical recipe to compute the Wigner function of a quantum state from its density matrix in the Fock basis. It can be split into part (II) that does not depend on the specific quantum state and part (I), the density matrix ρ_{mn}, containing

[4] this can be found, for example, in [41] by setting $\alpha = 1$ due to the conventions used here

all the specific information. In the previous section, the necessity to truncate the size of the Fock space to some maximum number state $|n_{\mathrm{co}}\rangle$, that also limits the size of the density matrix, was discussed. Therefore, the infinite sum in Eq. (3.19) has to be evaluated only up to $m, n = n_{\mathrm{co}}$. Part (II) is essentially a Fourier transformation of the product of two different overlaps between number and quadrature states. They can be calculated similar to Eq. (3.14) with $Q_i = q \pm \xi/2$ and $\theta_i = 0$.

The fact that part (II) is the same for each quantum state under study is very useful. This part has to be calculated only once for each possible pair ($m \leq n_{\mathrm{co}}, n \leq n_{\mathrm{co}}$) for appropriately discretized q and p variables, when the results are saved to disk. Afterwards, the calculated Fourier transforms can be used over and over again by reloading them from disk.

To sum up, this chapter outlined the basic strategy of optical homodyne tomography. The conceptual tools to perform quadrature measurements on a signal light field and to reconstruct the quantum state of the light field in terms of a density matrix and a Wigner function are now available for further use.

4. Stationary Optical Homodyne Tomography

In the OHT scheme explained in chapter 3, the relative phase θ between LO and signal plays a significant role. However, a single homodyne detector acquires only quadrature values and no phase values. Consequently, it is a usual property of typical OHT experiments to have a fixed phase relationship between LO and signal, which allows one to modulate the phase deterministically and therefore to infer the phase values either by the modulation alone or by combining information about the modulation with the general behavior of the acquired quadrature values. For light fields in pure states, assuming a perfectly coherent LO, such **a priori information** about the phase of the signal light is available. This is because light fields in pure quantum states are stationary, which means that they can be completely described by a single density matrix or Wigner function at any point in time with no temporal dynamics. Hence, this kind of optical homodyne tomography is called **stationary OHT** in this work.

In general, though, mixed states are non-stationary and can provide fluctuating phases. As outlined in chapter 1, the main goal of this thesis is to report an advance in the field of optical homodyne tomography, which will be called **non-stationary OHT**, may providing a solution to this problem. To get rid of the need for a priori information, a **12-port homodyne detector** was implemented instead of the usual 4-port homodyne detector for stationary OHT. An n–port homodyne detector is a device that transforms $n/2$ input modes into $n/2$ output modes and detects them with $n/4$ balanced detectors. This definition is close to [26, p. 361] and such devices can also be called n–port interferometers. A sketch of a 4–port homodyne detector is shown in Fig. 3.1, where the whole device only consists of one beam splitter and one balanced detector.

The focus of this chapter lies on the detailed description of the 4-port detector technology used throughout this work, as the technology of a 12-port homodyne detector is derived from it. It is based on the works of Kumar et al. [43] and Roumpos and Cundiff [39], but also includes several differences. To provide a comprehensive overview, the hardware and alignment of the system is presented first, followed by measurements of typical performance parameters. Afterwards, measurements of coherent and thermal states are discussed to benchmark the setup consisting of the hardware, the specific measurement routine and the software for data analysis. The meaning of **a priori information about the phase** is illustrated on these examples. Last, a major and common problem with **correlations** between consecutively measured quadrature values is evaluated. So far, a satisfying solution to remove them on the software side was found.

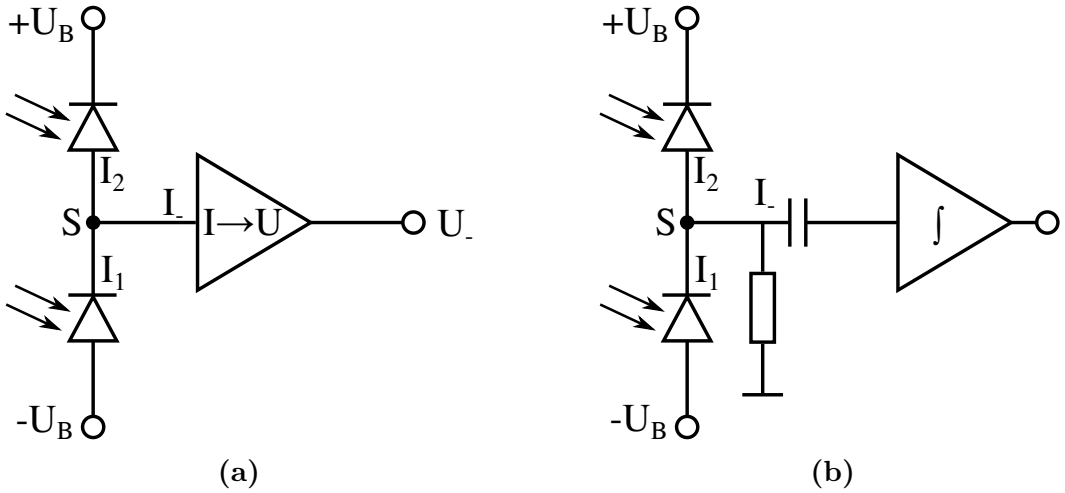

Figure 4.1.: Two common designs of balanced detectors that are (a) based on a transimpedance amplifier and (b) based on a RC circuit. In this work only type (a) detectors are used because of their speed advantage.

4.1. Building a 100 MHz 4-Port Homodyne Detector

It is often beneficial to use a pulsed laser to generate the LO, because it provides a high time resolution. As explained in section 3.1, only the part of the signal light that overlaps spatially, spectrally and **temporally** with the LO is amplified with balanced homodyne detection. Therefore, a pulsed LO allows the user to probe the signal light field only during each pulse. Since there are pulsed lasers with pulse durations of picoseconds, femtoseconds and below [44], pulsed LOs provide a very good time resolution that would not be accessible with a continuous wave LO.

The pulsed laser system used as the LO in this work, is a Mira 900 titanium sapphire laser from the US based company *Coherent*. Its pulse repetition rate is 75.4 MHz and the pulse duration can be set to either approximately 1.5 ps or 120 fs. The presented data was exclusively taken with the shorter pulse duration. As discussed, for example, by Kumar et al. [43], the bandwidth of the required balanced detector should exceed the pulse repetition rate to be able to distinguish consecutive pulses. Kumar et al. also provide a detailed analysis of their own 100 MHz homodyne detector that is well suited to be used with the Mira 900. The balanced detectors used in this work were ordered from the German based company *FEMTO Messtechnik* with a bandwidth of 100 MHz and a transimpedance gain of $5000\,\mathrm{V\,A^{-1}}$, which are the same values as in the design by Kumar et al. [43].

While the details of the circuitry can be quite intricate, the fundamental idea behind these balanced detectors is quite simple. As shown in Fig. 4.1a, two biased photodiodes are wired in series and illuminated. The produced photocurrents I_1 and I_2 result in a difference photocurrent I_- according to Kirchhoff's current law in the summation point S. With the help of a **transimpedance amplifier**, this difference photocurrent is now converted to a voltage signal by $U_- = R_{\mathrm{trans}} I_-$ and the conversion ratio R_{trans} is

called **transimpedance gain**. Another detection principle commonly used for balanced homodyne detection[1] is shown in Fig. 4.1b. Here, the difference photocurrent charges (or discharges) a capacitor in front of the amplifier. The capacitor automatically translates the current signal into a voltage signal that is proportional to the photocurrent integrated over a certain time. For a pulsed laser system, this time should be lower than the time span between two pulses. The measured peak voltage is proportional to the difference photon number of the two pulses detected by the photodiodes. Unfortunately, this design is limited in speed by the characteristics of the RC circuit and is usually not suitable to work at 100 MHz.

The whole setup used for the experiments in this chapter is shown in Fig. 4.2 and all of its parts are discussed in the following paragraphs. The discussion starts with the parts corresponding to the balanced homodyne detection scheme from Fig. 3.1 that are enclosed in the dashed line rectangle titled HD1. In the original scheme in Fig. 3.1, there was only one non-polarizing 50:50 beam splitter with the LO and the signal beam entering the two input ports and the output beams being detected by a balanced detector. The two input ports of HD1 are the two input ports of the polarizing beam splitter PBS3. The LO beam (red) as well as the signal beam (green) leave PBS3 in the same direction, because they have linear polarizations that are orthogonal to each other. This is also the reason why they don't interfere with each other on the way from PBS3 to PBS4. Before entering PBS4, their polarizations are rotated by about 45° with a half-wave plate so that 50 % of the LO and 50 % of the signal exit each output port of PBS4. At the output ports, LO and signal are now able to interfere. Afterwards, both beams are focused on a balanced detector (BD) by means of the lens in front of PBS4. In the end, this slightly more complex scheme allows the user to balance the BD output voltage with the help of the half-wave plate which is necessary, for example, because the photodiodes are subject to production tolerances and there are possibly other imperfections in the setup.

The two elements in HD1 not mentioned so far are a CCD camera (CCD) and a piezo phase shifter (Piezo). The *mvBlueCOUGAR-X124G* CCD camera from the German based company *Matrix Vision* is connected to the computer and can be used to check the proper alignment of LO and signal. The Piezo can move the connected mirror back and forth by up to 2 µm with sub-nanometer precision and therefore tune the relative phase between LO and signal. The piezo actuator *S-303.CDI* from the German based company *Physik Instrumente (PI)* is controlled by a *E-725* piezo controller from the same company.

The LO light is generated by a Mira 900 laser system. A small part of it is then separated by a combination of a polarizing beam splitter (PBS1) and a half-wave plate to be detected by a photoreceiver (PR)[2]. The photoreceiver has a bandwidth of 200 MHz and is used to trigger the data acquisition electronics. The next combination of a half-wave plate and a beam splitter (PBS2) splits off a part of the LO that can be fed into the signal beam path (LO as signal). This is essential for the alignment process and also useful as a coherent state for benchmarking purposes. Finally, before entering the

[1] see, for example, [21, p. 140]

[2] model *HCA-S-200M-SI-FS* manufactured by *FEMTO Messtechnik*

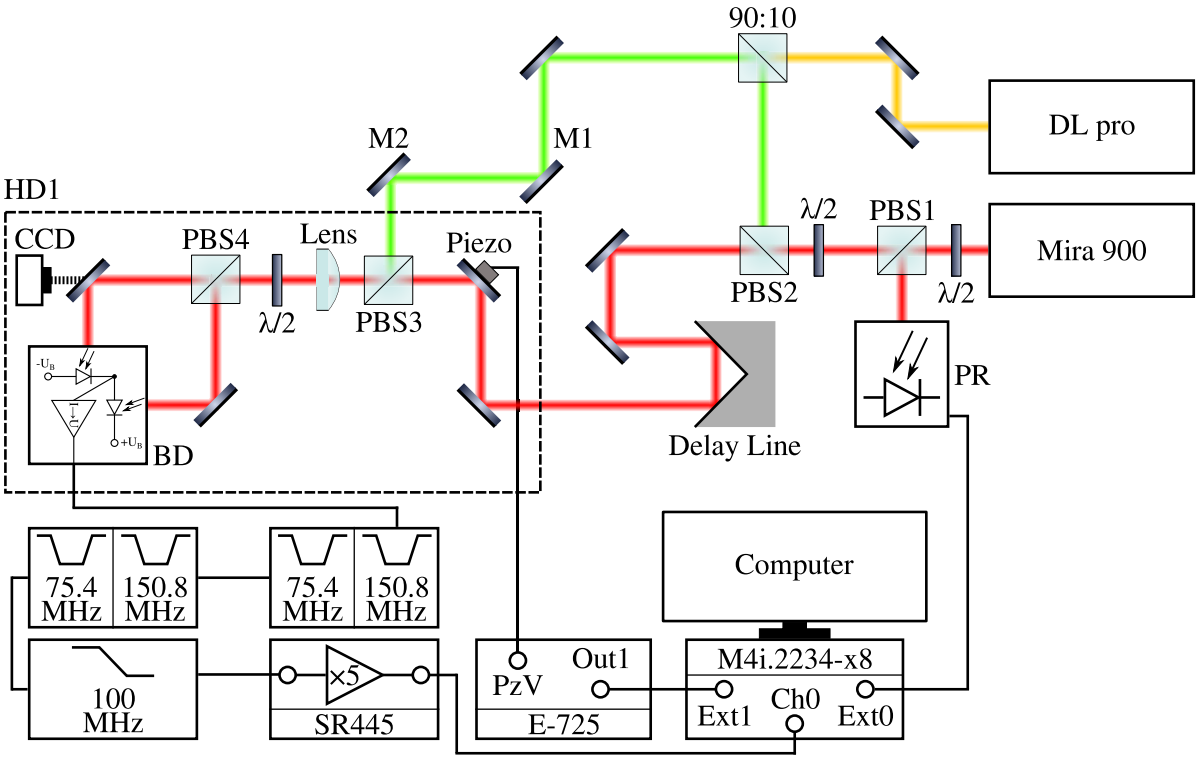

Figure 4.2.: Scheme of the 4-port homodyne detection setup used for stationary OHT. See text for details.

HD1 zone, the LO passes a **Delay Line**. It consists of a retroreflector mounted on a motorized translation stage and allows the user to change the length of the LO beam path by tens of centimeters without changing the optical axis in the HD1 zone. This is crucial for aligning the temporal overlap of the LO with the LO as signal.

Unless mentioned otherwise, the signal is either split off from the LO or generated by a *DL pro* Littrow-type external-cavity diode laser from the German based company *Toptica*. By employing a 90:10 non-polarizing beam splitter, the signals from the LO and from the DL pro can be aligned on exactly the same signal beam path. Hence, one can switch between them easily by either blocking one or the other. Since the signal light from the DL pro is weaker than the LO, the 90:10 beam splitter is oriented in such a way that the signal is transmitted with 90 % efficiency while the LO is reflected with 10 % efficiency.

The analog signal processing elements are discussed next. The voltage signal from the balanced detector (BD) first passes a sequence of filters before being amplified and digitized. The first filter, which is identical to the second one, is a combination of a 75.4 MHz and a 150.8 MHz band-stop filter, each suppressing its respective frequency by about 40 dB. These filters were manufactured by the German based company *Rittmann-HF-Technik* according to custom specifications. The goal of using these filters is to eliminate the first and second harmonic of the laser repetition rate from the voltage signal. There are two of them because a suppression by about 80 dB is required. All higher harmonics are eliminated with the help of a 100 MHz low-pass filter from the US based company *Crystek*. Before being digitized, the remaining signal is amplified by a factor of 5 by a 300 MHz *SR445* amplifier from the US based company *Stanford Research Systems*.

In the end, the amplified signal is fed into the *Channel0* input of the 8-bit digitizer *M4i.2234-x8* from the German based company *Spectrum Instrumentation* that provides acquisition speeds of up to 5 GS/s. This digitizer features two trigger inputs, the main external trigger *Ext0* (analog window trigger) and the secondary external trigger *Ext1* (analog comparator trigger), which are both in use for this setup. The *Ext0* input is connected to the photoreceiver (PR) monitoring the LO laser pulses while the *Ext1* input is connected to the programmed digital output *OUT1* of the *E-725* piezo controller. Section 4.2 provides more information about the specific piezo modulation and the trigger scheme used during measurements.

4.1.1. Optical Alignment

In this section, a basic alignment routine for the setup described above is discussed. A good alignment procedure should be fast, reproducible, and accurate enough for the measurements to be meaningful. The most critical part for a homodyne detection setup is the alignment of the LO and signal to **overlap spectrally, spatially, temporally and in polarization**. At least for the experiments in this chapter, the spectral overlap is easily achievable by tuning the central wavelengths of the *Mira 900* and the *DL pro*. In more advanced experiments, it may be necessary to control the spectra of LO and signal more strictly by employing, for example, an **optical filter** or a **pulse shaper**. Since

the alignment procedure always starts with the LO as signal, an ideal spectral overlap is guaranteed. The overlap in polarization is also easily achieved by first polarizing signal and LO linearly and then employing a combination of two polarizing beam splitters (PBS3 & PBS4) and a half-wave plate shown in the HD1 zone of Fig. 4.2.

The more time-consuming alignment steps are related to the spatial and temporal overlap of signal and LO. First, the spatial alignment of the beams is discussed. It aims at having the LO as well as the signal beam on the same optical axis, moving in the same direction and with the same beam diameters (or alternatively spatial intensity distributions). To begin with, the beam diameters can be manipulated with the help of telescope assemblies (not shown in Fig. 4.2), such as a combination of two lenses with a pinhole in between or commercially available beam expanders. If not done before, the delay line can be aligned with the help of the two mirrors in front of it to prevent any change of the optical axis of the reflected LO when changing its position. Next, the LO beam path has to be aligned to the optical axis defined by PBS3 and PBS4. In practice, the lens between them may be removed and the use of irises to define the optical axis is recommended before iteratively aligning the LO beam path with the help of the two mirrors in front of PBS3. Having two mirrors for such an alignment allows the user to independently control the two angular and the two spatial degrees of freedom of the beam. After that, the signal beam can be aligned with the help of the two signal mirrors in front of PBS3 to the same irises. After reducing the combined power of the beams, for example to 100 µW, 50 µW each, one can perform the next alignment step with the help of the CCD (after removing the mirror in front of it).

While the irises are useful to perform a coarse alignment, the **CCD** helps to align the signal beam path to the LO beam path more precisely. The alignment is performed iteratively in two steps utilizing the two mirrors in the signal beam path in front of PBS3. In the following paragraphs, the mirror that is closer to PBS3 is named M2 and the other one M1. In the first step, M1 is used to center the signal spot on the LO spot in the plane of the CCD sensor. In the second step, the lens in front of PBS4 is inserted again, adjusted on the optical axis of the LO, and then M2 is used to center the Fourier image of the signal spot on the Fourier image of the LO. When signal and LO are centered on each other with and without the lens, the fine spatial alignment is completed and the lens has to be removed for the temporal alignment.

Since the LO as well as the LO as signal are pulsed laser beams, it is highly unlikely that their pulses arrive on the CCD camera at the same time. Hence, no interference pattern is visible on the CCD chip. The optimal temporal overlap can be found by driving the **delay line** to a position where the pulses of the LO arrive at the same time as the pulses of the signal. When designing a homodyne detection setup, the signal and LO path lengths must be approximately equal. With a repetition rate of 75.4 MHz, two consecutive pulses from the *Mira 900* have a distance in optical path length of about 4 m and the delay line has to be able to modify the LO path length enough to overlap signal and LO pulses temporally. To find this overlapping position, the delay line has to be driven slowly while monitoring the combined signal and LO spot on the CCD for an interference pattern. The delay line was driven with a speed of $50\,\mu m\,s^{-1}$ and

additionally, the piezo mirror was driven with a slow 0.5 Hz sinusoidal modulation to find the interference pattern more easily. Usually, there are many positions that show weak interference patterns because of reflections in the beam paths but there is only one position with fringes that show ideal visibility.

Most of the time, a third round of spatial alignment is necessary. Initially, the interference pattern of LO and signal without the lens will probably consist of several stripes, because the light is linearly polarized. If the beams are perfectly aligned, there will only be one round spot with an intensity depending on the relative phase between LO and signal. Since the piezo mirror modulates this phase, the interference pattern will be a round spot that is "blinking". Again, one has to iteratively operate mirrors M2 and M1. M2 is used in the usual way, to center the signal spot on the LO spot, while M1 is used to minimize the number of stripes in the interference pattern. If there is only one blinking spot, the two beams will be overlapping and interfere with each other. Sometimes it is necessary to drive the delay line again, because the temporal overlap has slightly changed by tuning the mirrors.

After aligning LO and LO as signal, the beam path of the signal under investigation must be aligned. In case of the setup in Fig. 4.2, this is the beam path of the *DL pro*. Strictly speaking, if the signal is a continuous wave light source and one is not interested in measuring the LO as signal, the alignment process may be started with the signal of interest and the temporal alignment step can be skipped. Nevertheless, the alignment procedure with the LO as signal is mandatory when using an n-port homodyne detector with $n > 4$ because the temporal overlap has to be synchronized in all output ports, as described in chapter 6. Since most of the work was already done in the previous steps, the alignment of the *DL pro* only requires the two mirrors in front of the 90:10 beam splitter to be aligned. After blocking the LO, they are used iteratively to perform a fine spatial alignment of the signal beam path to the LO as signal beam path. The CCD and the lens serve the same purposes as in the fine alignment of the LO as signal to the LO. Alternatively, the signal from the *DL pro* can be aligned directly to the LO by blocking only the LO as signal.

4.1.2. Balanced Detector Alignment

As soon as the LO and signal are properly overlapped, the alignment of the balanced detector (BD) can be performed. In principle, the alignment of the BD can be done without first aligning the signal to the LO, because the signal is blocked during the whole procedure. It should however be done before, because the removal of the mirror in front of the CCD for the signal alignment and handling of the lens would certainly misalign the balanced detector again. As the bandwidth of the detector is high with 100 MHz, the round photosensitive area of the photodiodes[3] in the detector is comparatively small with a diameter of merely 0.8 mm. Therefore, the laser spots have to be focused onto the photodiodes of the BD by aligning the mirrors behind the beam splitter PBS4.

In the setup of Fig. 4.2, a 30 cm lens is used to achieve an optimal balance between

[3]the *S5972* photodiodes were provided by the Japan based company *Hamamatsu Photonics* [45].

a small spot size in the focus point and a high Rayleigh length with a thin beam waist, which makes the detector alignment easier. Before the actual alignment, some preparations are needed. All beams apart from the LO itself have to be blocked and the LO power has to be reduced, for example to about 100 µW. The output voltage of the BD must be monitored without the filter chain. The *M4i* digitizer together with the oscilloscope software *SBench*[4] is sufficient for monitoring purposes, but any oscilloscope with a 50 Ω input can be used. The BD itself should be positioned on the optical table in such a way that both photodiodes are at a distance of one focus length from the lens. Hence, it is useful to mount the detector on a xy-stage, which allows one to move the BD in parallel directions to both incoming light beams for later corrections. Also the half-wave plate must be adjusted to split the LO by roughly 50 % on PBS4.

For a coarse alignment, the focused spots are centered on the photodiodes of the BD by eye. From there, only the oscilloscope has to be monitored, which should be triggered by the pulse-monitoring photoreceiver (PR). Initially, it is likely that one sees a weak signal or no signal at all on the oscilloscope. By tuning the mirrors in front of the photodiodes, the signal should be maximized with one mirror and minimized with the other, because the difference photocurrent is amplified. Since the laser spot is smaller than the photosensitive area, a "plateau" can be found, where tuning the mirrors inside a narrow range only results in minor changes of the signal. Adjusting the mirrors to the middle of this plateau centers the spot on the photodiode, which makes the setup more robust to distortions like mechanical vibrations. Afterwards, the half-wave plate can be used to minimize the amplitude of the signal. One can now increase the LO power step by step and iterate the adjustments of the mirrors and the half-wave plate until the target power is reached with a minimal residual signal. In most experiments presented in this work a LO power of 5 mW was used.

An ideal detector would now only show a slightly noisy zero-line while a real detector still exhibits a strong residual signal appearing with each laser pulse. When the amplitude of this signal is too high, for example larger than ±500 mV, one can try to find a better distance between the photodiodes and the lens by driving the xy-stage and readjusting the mirrors. This may allow the user to minimize the difference signal further by about a factor of 2. It is important to note that the photodiodes have a certain damage threshold that should not be exceeded. In the case of the S5972 photodiodes the threshold amounts to 10 mW. After adjusting the balanced detector, the setup is completely aligned.

4.1.3. Phase-Averaged Quadrature Measurements

When the setup is properly aligned, measurements of the quadrature operator $\hat{q}_\theta$ are possible. As the LO is a pulsed laser, it obtains one quadrature value Q_i for each LO pulse. Basically, there are two types of measurements possible with this 4–port homodyne detector: **Phase-sensitive** and **phase-averaged** measurements for stationary OHT. The former case requires a well defined phase relationship between the LO and

[4] from the company *Spectrum Instrumentation* that manufactured the *M4i* digitizer

the signal that allows for the reconstruction of a relative phase value θ_i belonging to the measured quadrature value Q_i. In the latter case, there is no such relationship and the phase θ_i takes a random value for each LO pulse. The data acquisition and data analysis procedures are slightly different for each case as described below.

First, the **phase-averaged** measurements are discussed. The phase-sensitive measurements are an expansion of the phase-averaged ones and are discussed in a later section. Regardless of the phase relationship, the data acquisition is performed with the *M4i* digitizer triggered by the PR photoreceiver connected to the *Ext0* trigger input, which is terminated with 50 Ω to prevent reflections. The trigger level is set to 400 mV while the amplitude of the PR signal should be around 800 mV. The electronic hardware in the setup is controlled by a LabView[5] program that also saves the acquired data files to disk. In the *simple trigger* scheme for phase-averaged measurements, the digitizer starts to acquire the BD output voltage as soon as it receives a trigger signal. After a period of time corresponding to 1000 laser pulses, the acquisition stops, the trigger is rearmed and the procedure starts again with the next trigger signal. This behavior repeats until a predefined amount of data is acquired. After the measurement, the LabView program writes three files to disk: One **.raw* file containing the acquired 8-bit values, one **.raw.stamp* file containing the **timestamps** corresponding to the received trigger signals, and one **.raw.cfg* file containing the parameters of the LabView program used to perform the measurement.

The idea of the data analysis that follows is to first compute values n_i corresponding to measurements of the operator $\hat{N}_-$ introduced in section 3.1 and then to calculate quadrature values Q_i corresponding to measurements of the operator $\hat{q}_\theta$ with the help of Eq. (3.6). The second step requires the knowledge of N_{LO}, the average number of photons in one LO pulse. Accordingly, for each measurement with LO and signal (*LOwithSIG*), it is necessary to have a corresponding measurement with the same parameters but a blocked signal (*LOonly*). The data analysis is performed with the help of custom software written in MatLab [42]. The software identifies the centers of the LO pulses in the raw data and then performs an integration over a given window around each pulse. The resulting values n_i are proportional to the difference of the photon numbers detected by the two photodiodes for the corresponding LO pulses. To compute N_{LO} from a *LOonly* measurement, the average of the variance of each series of n_i values belonging to the same trigger signal is calculated. Afterwards, the quadrature values Q_i from a *LOwithSIG* measurement with integrated values n_i are calculated by

$$Q_i = \frac{n_i}{\sqrt{2N_{\mathrm{LO}}}} \tag{4.1}$$

and the final result is a set of phase-averaged quadrature measurements $\{Q_i\}$.

4.1.4. Detector Performance

Before discussing measurements on real quantum states, several characteristics of the balanced detector are demonstrated to establish its suitability for optical homodyne

[5]LabVIEW version 2014 provided by *National Instruments*

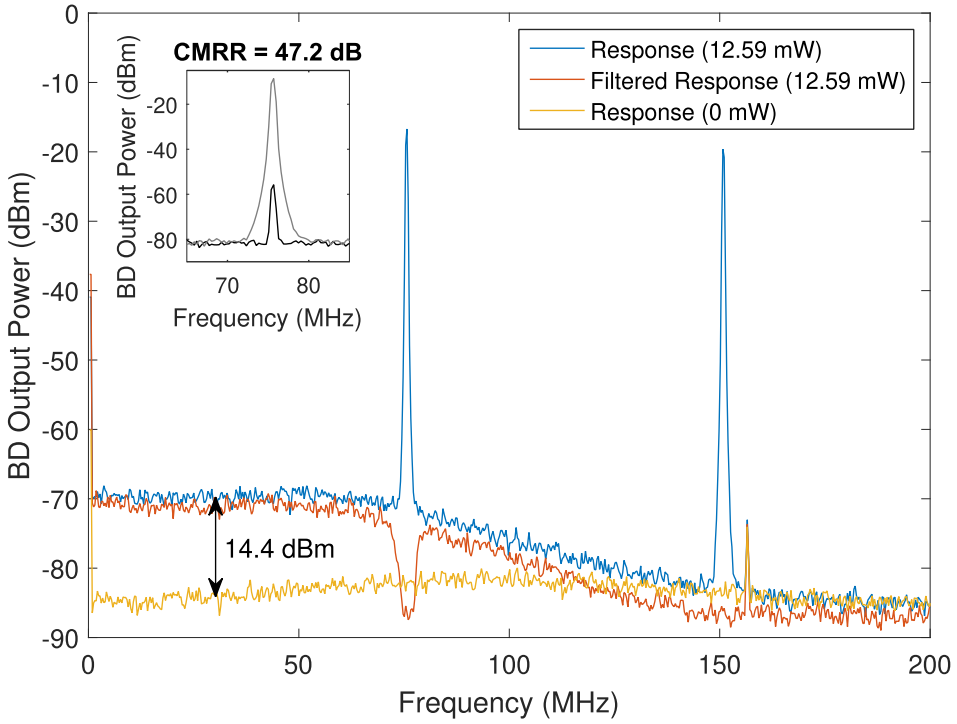

Figure 4.3.: Power spectra of the BD output voltage either with or without the filter chain for two different LO powers. The *SR445* amplifier was not used and there was no signal applied. Inset: Applying an LO power of only 100 µW and either using only one photodiode (gray, higher peak power) or both (black, lower peak power).

tomography. The most important characteristic of a balanced detector for OHT is its **shot-noise limited performance** under typical operating conditions. This means, if there is no signal light present in the homodyne detection setup, the photon number fluctuations Δn of the LO dominate the fluctuations in the output voltage of the balanced detector. As the LO is in a coherent state, its photon statistics are described by a Poissonian distribution and the fluctuations $\Delta n = \sqrt{\overline{n}}$ are proportional to the square root of its mean photon number $\overline{n}$ (see section 2.4). It is later shown that the fluctuations in the output voltage of the BD follow such a square root behavior in the range of LO powers used for measurements. Other important detector characteristics include the **shot noise clearance**, the **common mode rejection ratio** (CMRR) and the **linearity** of the balanced detector. While the shot noise clearance is the factor between shot noise and other noise sources, the CMRR defines the factor by which the detector suppresses a common mode optical signal that is applied to both photodiodes with the same amplitude at the same time. The linearity is a measure for how linear the detector amplifies the applied signals over the full range of applicable LO and signal powers.

In order to find a value for the CMRR, the common mode signal has to be estimated before it can be compared to the rejected common mode signal. Since the common mode signal is given by the LO, the amplitude of the BD output signal in the frequency domain at 75.4 MHz is a good approximation for the amplitude of the common mode

signal. As the shot noise clearance can also be easily estimated from the amplitudes of the flat shot noise background and the electronic noise background in the frequency domain, power spectra of the BD output voltage were taken for different LO powers and are shown in Fig. 4.3. The BD output voltage was recorded by the *M4i* digitizer either with or without the filter chain, but always without the *SR445* amplifier. The frequency spectra were calculated subsequently via a fast Fourier transform (FFT) by the *SBench* software. In all measurements, only the LO without a signal light field was applied. The CMRR measurements were performed with a LO power of 100 µW at a central wavelength of 835 nm. In the inset of Fig. 4.3, the power spectrum around the first harmonic of the LO repetition rate is shown. The CMRR of 47.2 dB corresponds to the difference between the peak powers of both curves. One curve shows the spectrum when only one photodiode is illuminated, while the other shows the spectrum for both diodes being illuminated and therefore suppressing their common mode. The measured CMRR is comparable to the 52.4 dB reported by Kumar et al. [43].

The yellow curve in Fig. 4.3 shows the electronic noise background with no light applied to the detector. In the frequency range of interest between 0 and 100 MHz it moves up from about −85 dBm to about −80 dBm. The blue curve represents the unfiltered detector response at an LO power of 12.59 mW. The residual common mode signal is visible at the laser repetition rate of 75.4 MHz and its first harmonic. Additionally, there is a roughly flat white background between 0 and 100 MHz with a strength of about −70 dBm, that represents the optical shot noise of the local oscillator. The shot noise clearance of 14.4 dB is calculated as the difference of the averaged electronic noise background and unfiltered detector response between 20 and 40 MHz. This number is comparable to the 13 dB reported by Kumar et al. [43]. The filtered detector response was recorded the same way as the unfiltered one but with the filter chain between the detector and the digitizer in place. It successfully removed the residual common mode signal which allows the flat shot noise background to be the dominant signal.

For each data point in the linearity tests shown in Fig. 4.4, the filtered and amplified BD output voltage was acquired 21 times during 1000 LO laser pulses. Afterwards, the average of the variances of the 21 time traces was calculated. The error bars indicate the standard deviation from this averaging procedure. The variance of the BD output voltage is a measure for the BD output power, because it represents the quadratic deviations from the mean output voltage, and a squared voltage corresponds to an electrical power. Both, the BD output power and the standard deviations are expected to grow linearly with the LO power because the power of the shot noise depends linearly on the photocurrent and, thus, linearly on the optical input power [21, p. 96]. Indeed, the linear regressions for the LO power series as well as the signal power series show good agreement with the measurements. This indicates two properties of the employed setup: First, the BD output power is dominated by optical shot noise. And second, the balanced detector has a linear amplification profile for the investigated powers. However, for signal powers above 1 mW, the shown standard deviations become stronger and fluctuate more. This is a sign for instabilities or non-linearities in the detection channel. Therefore, such high signal powers should be avoided for OHT.

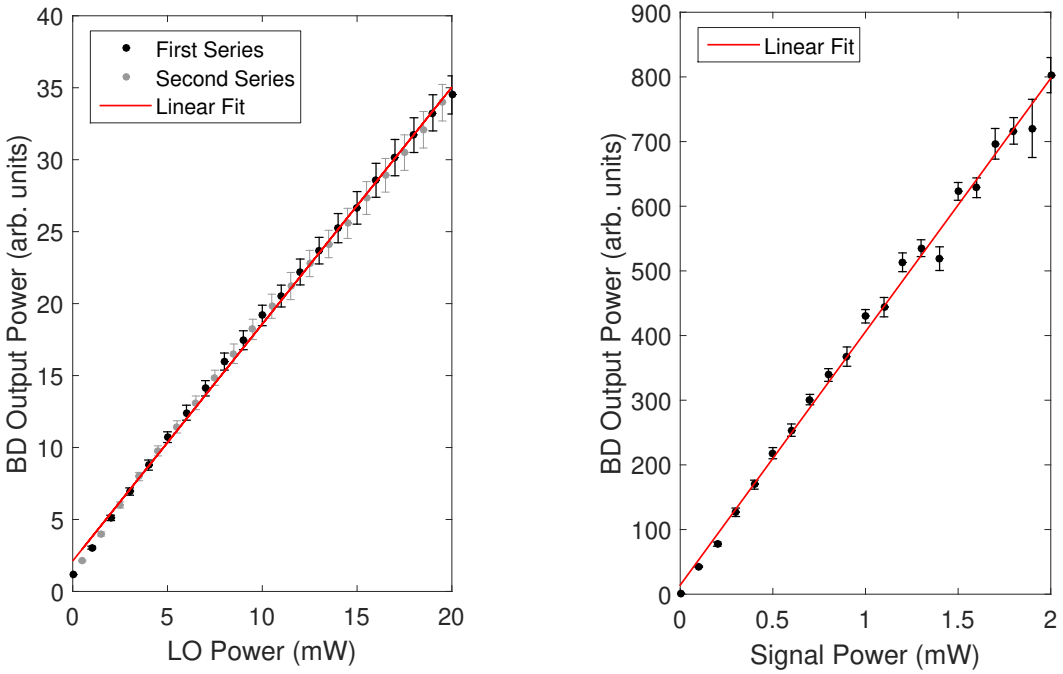

Figure 4.4.: Testing the dependence of the 100 MHz balanced detector's output power on (a) the LO power without applying a signal and (b) the signal power from a cw laser at a constant LO power of 5 mW. The second measurement series in (a) was taken directly after the first to verify the reproducibility of the results. Error bars indicate standard deviations. Both, the filter chain and the amplifier, were used in the setup.

An indicator for the proper LO power to use in experiments is, however, missing in previous tests. A shot noise clearance of 14.4 dBm at a LO power of 12.59 mW is known from Fig. 4.3 and operation in the shot noise limited regime is indicated by the linearity tests in Fig. 4.4. In order to find a range of LO powers where shot noise is dominant, we now analyze quadrature values Q_i obtained in measurements for different LO powers with no signal applied. Here, the quadrature values Q_i are the integrated values n_i introduced in section 4.1.3. The double logarithmic plot in Fig. 4.5 shows the standard deviation ΔQ of these quadrature values depending on the applied LO power. The LO powers were chosen equidistant on a logarithmic scale to achieve a linear spacing between data points in the plot. Above 1 mW, the data points clearly follow the square root behavior expected for shot noise that is indicated by the red line. Below 1 mW, other noise sources seem to result in deviations from this behavior. From the experiments it becomes apparent that the LO power should be above 1 mW in order to achieve **shot-noise limited** performance of the 4-port homodyne detector. Unless indicated otherwise, an LO power of 5 mW is used in this work.

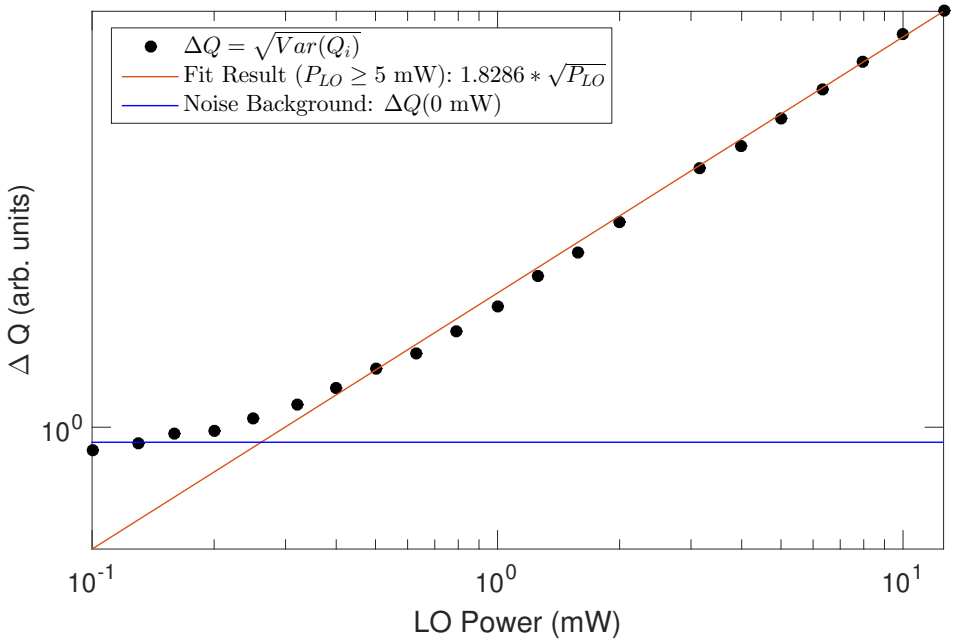

Figure 4.5.: Standard deviation ΔQ of quadrature values obtained at different LO powers. Starting from about 1 mW, ΔQ follows a square root behavior as expected for shot noise.

4.2. Benchmarking with Coherent and Thermal States

In the beginning of this chapter, all parts of the 4-port homodyne detector, its alignment procedure and its performance are discussed in detail. In the following section, measurements of two well known real quantum states are presented to benchmark the performance of this setup. In this context, **benchmarking** means that the measured coherent and thermal states are compared to the theoretical models describing them. The discussion starts with phase-averaged measurements of a thermal and a coherent state from a diode laser. Then, the procedures for phase-sensitive quadrature measurements are introduced and applied to a coherent state originating from the *Mira 900*.

4.2.1. Phase-Averaged Coherent and Thermal States

The setup shown in Fig. 4.2 allows one to perform phase-averaged measurements of thermal and coherent states. The *DL pro* diode laser can generate signal light fields in both states. If its drive current is below the lasing threshold, light with thermal characteristics is emitted, while coherent light is expected to be emitted at drive currents above the lasing threshold. Histograms of the acquired quadrature values Q_i are shown in Fig. 4.6a for the diode laser driven below the lasing threshold and in Fig. 4.6b for the diode laser driven above the lasing threshold. The central wavelength of the LO and the coherent signal light was chosen to be 835 nm. Each histogram contains data from 1 579 419 individual quadrature measurements.

The first value of interest is the average number of photons $\bar{n} = \langle \hat{n} \rangle$ of a quantum

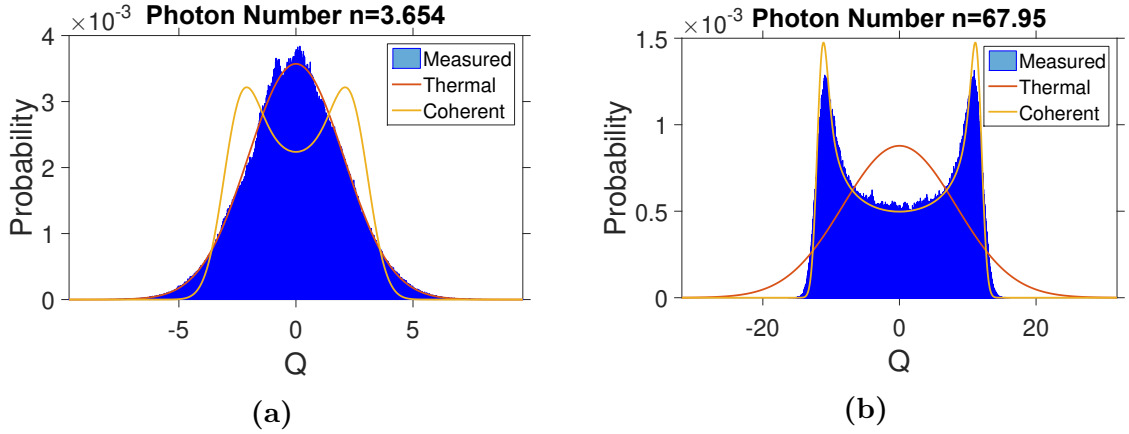

Figure 4.6.: Phase-averaged quadrature histograms for a thermal state (a) and a coherent state (b) together with the theoretically predicted distributions.

state. For a phase-averaged measurement of a coherent quantum state, $\bar{n}$ is given by Eq. (2.31) ($A = 1/\sqrt{2}$ has to be substituted):

$$\bar{n} = \left\langle \hat{q}^2_{\text{random }\theta} \right\rangle - \frac{1}{2} \tag{4.2}$$

The same formula gives the average number of photons for a thermal state, which can be seen from Eq. (2.13):

$$\langle \hat{n} \rangle = \frac{1}{2}\left(\hat{q}^2 + \hat{p}^2\right) - \frac{1}{2} = \left\langle \hat{q}^2_{\text{random }\theta} \right\rangle - \frac{1}{2} \tag{4.3}$$

In the last transformation, we used the observation that, regardless of the angle θ, all projections of a thermal state look the same due to its symmetry. Applying the fact that the Q_i are measurements of $\hat{q}_{\text{random }\theta}$, it is possible to compute a mean photon number of $\bar{n} = 3.65$ per LO laser pulse for the thermal state and $\bar{n} = 67.9539$ for the coherent state by averaging over all Q_i values.

In order to compare the measured histograms to the theoretically expected probability distributions, predictions for a thermal state (red) and a coherent state (yellow) are shown in Fig. 4.6. They were calculated for the average photon numbers computed in the previous paragraph. Due to its symmetry in phase space, the probability distribution of a phase-averaged thermal state is simply any of the integral projections of its Wigner function (see for example Fig. 2.6a). The prediction for a coherent state may look surprising at first, due to its two distinct peaks at both ends of the distribution. These can be explained when considering the histogram in Fig. 4.6b as a normalized sum of integral projections of coherent state Wigner functions with random phases, as illustrated in Fig. 4.7. In both cases, the measured histograms closely match the theoretical predictions.

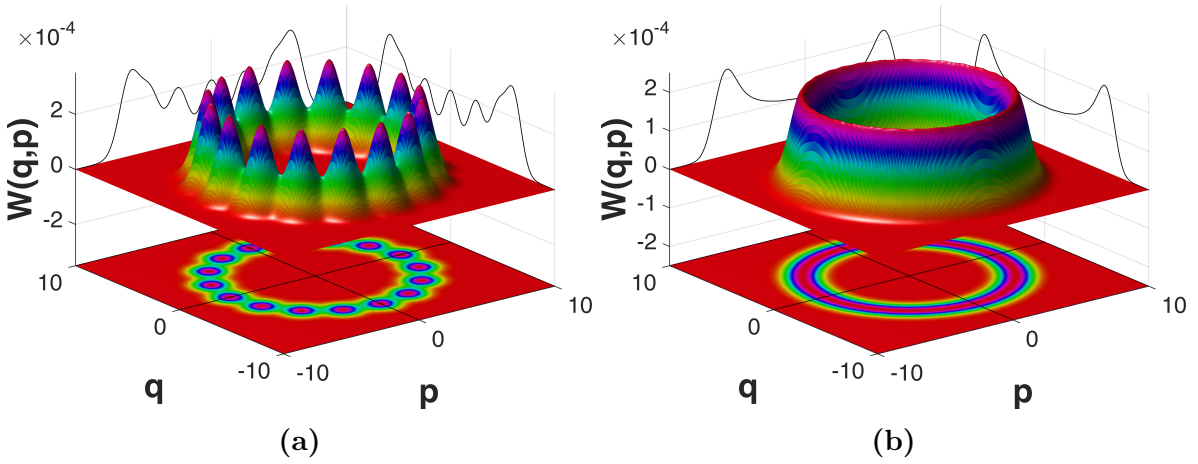

Figure 4.7.: Illustration of the phase-averaged measurement of a coherent state as a sum of 16 (a) and 32 (b) integral projections of coherent state Wigner functions with different phases.

4.2.2. Phase-Sensitive Quadrature Measurements

For many quantum states, such as a coherent state, phase-sensitive quadrature measurements are possible with stationary OHT. These states are not rotationally symmetric around the origin in phase space and therefore the measured quadrature distributions are different for different projection angles θ. The 4-port homodyne detection setup shown in Fig. 4.2 is capable of performing such measurements, when one *a priori* condition is met: The investigated signal light field must have a **fixed phase relationship** with respect to the local oscillator. In this case, it is possible to tune this relative phase

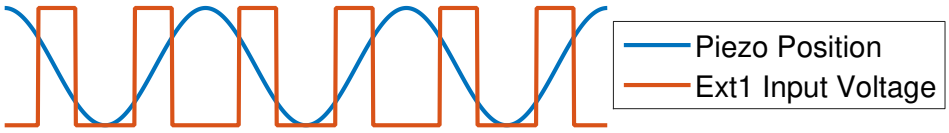

Figure 4.8.: The *Ext1* trigger signal (red) provided by the piezo controller is a TTL signal being in the high state if the piezo position (blue) lies between an upper and lower threshold. The thresholds are chosen asymmetrically, so rising and falling edges may be distinguished in the data processing step.

The phase-sensitive measurements are very similar to the phase-averaged measurements from section 4.1.3. The only difference lies in the additional piezo modulation and a different trigger scheme. In the following, this is called *complex trigger* scheme. The piezo mirror is driven either with a triangular or sinusoidal voltage at 50 Hz. In the data processing step, the position of the piezo mirror has to be estimated for the phase reconstruction. Thus, it is advantageous to only acquire quadrature values while the piezo movement is roughly linear in time. This condition is met in the middle of

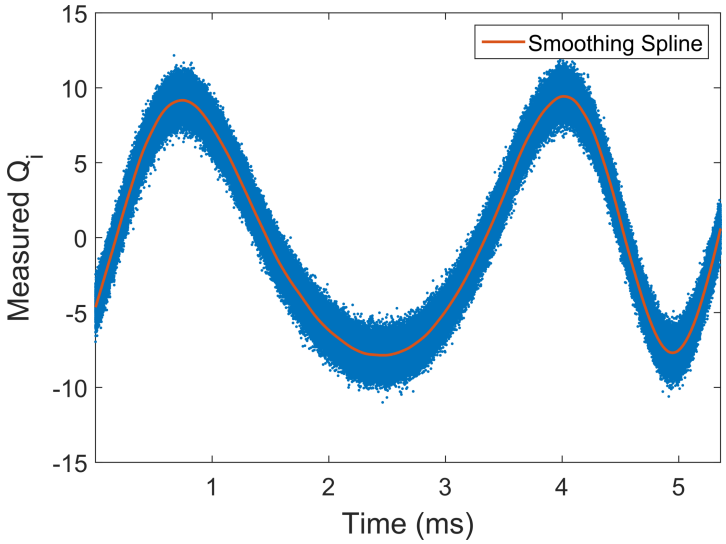

Figure 4.9.: Acquired quadrature values (blue) from a coherent state during one segment of the piezo modulation with an approximately constant speed. The coherent offset can be fitted quite well with a smoothing spline (red).

the movement from one extremal position to the other for both modulation patterns. Around the extremal points, the sinusoidal modulation results in nonlinear driving of the piezo, while the triangular modulation produces unwanted oscillations due to the abrupt change in direction. For the *complex trigger* scheme, the piezo controller is programmed to output a TTL signal that is only high when the piezo position is between an upper and lower threshold, as shown in Fig. 4.8. This signal is then fed to the *Ext1* input of the data acquisition card and used to "gate" the *simple trigger*. Accordingly, trigger signals from the *Ext0* input are only accepted when the *Ext1* input is high at the same time. In this way, the BD voltage is only acquired while the piezo modulation is in the desired range and the timestamps of the applied trigger signals allow us to estimate the piezo position and therefore the relative phase of LO and signal.

The reconstruction algorithm used to record a series of tuples (Q_i, θ_i) from a coherent state measurement is discussed next. Figure 4.9 shows in blue the quadrature values Q_i, acquired during one approximately linear piezo movement of about 1 µm. For a coherent state, the measured quadrature values consist of two parts. First, an offset that is called the **coherent offset**, depending on the phase θ, and fluctuations around this coherent offset. The coherent offset is expected to be proportional to $\sin(\theta + \theta_0)$ with an unknown phase offset θ_0. Moreover, θ should be linear in time in order to match the movement of the piezo actuator. The coherent offset in Fig. 4.9 is indeed sinusoidal, but still deviates significantly. These deviations probably result from drifts of the optical path lengths either induced by unwanted oscillations of the mechanics mounting the piezo actuator or other influences like wind from the air conditioning system. In the end, a simple sinusoidal fit does not match the data well enough to use it to reconstruct the phase values θ_i.

It is still possible to extract the phase with the following algorithm:

1. Calculate a smoothing spline fit $S(t)$ of the measured quadrature values that follows the coherent offset. This fit is shown in Fig. 4.9 as a red line.

2. Identify the maxima and minima m_i of $S(t)$ and divide $S(t)$ in intervals $S_i(t)$ covering all values from m_i to m_{i+1}.

3. Normalize the function $S_i(t)$ to the interval $]-1, 1[$.

4. Use either $\theta(t) = \arcsin(S_i(t))$ or $\theta(t) = \pi - \arcsin(S_i(t))$ to reconstruct the phase depending on the orientation of the edge (rising or falling).

This algorithm circumvents the problems described in the previous paragraph by assuming an underlying sinusoidal dependence of the coherent offset on the phase but doesn't need a linear behavior of this phase. The actual algorithm is slightly more complicated because it catches many possible exceptions like changing amplitudes and accounts for different boundary conditions. It was used for the phase reconstruction throughout the rest of this work.

4.2.3. Phase-Sensitive Coherent State

The simplest phase-sensitive measurement that can be performed with the setup in Fig. 4.2 is the measurement of the LO as signal. The *a priori* condition of a fixed phase relationship between the signal and the LO is met because the LO as signal is split off the LO itself. After performing quadrature measurements and a phase reconstruction according to the previous section, one has tuples (Q_i, θ_i) of measured quadratures Q_i at phases θ_i. These can be used to analyze and reconstruct the underlying quantum state.

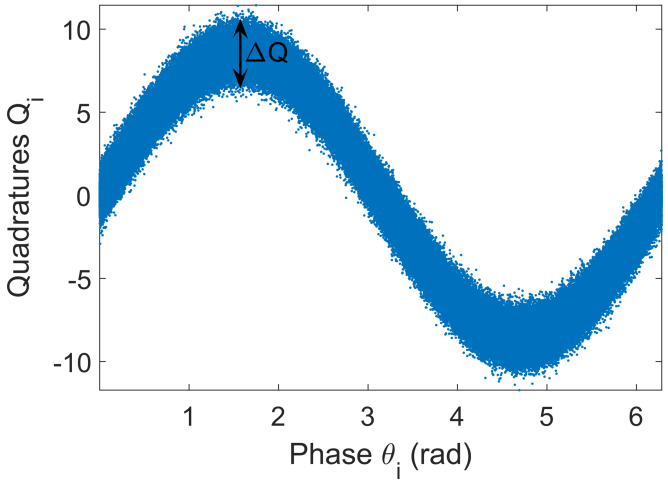

Figure 4.10.: Quadrature signals Q_i of a coherent state derived from the LO itself consist of two parts. First, a coherent offset with a sinusoidal dependence on the relative phase θ_i of the LO and the signal. And second, fluctuations around this offset with a standard deviation of ΔQ.

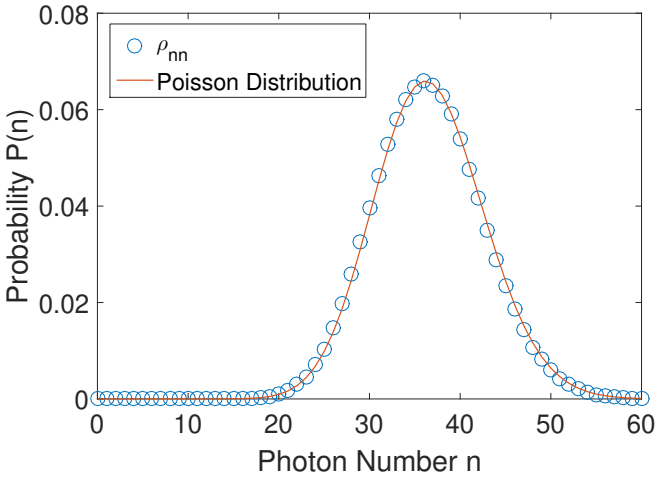

Figure 4.11.: Diagonal elements of the density matrix reconstructed from measurements of the LO as signal. As expected for a coherent state, they follow a Poisson distribution (red line).

First, we look at the question how Q depends on θ (shown in Fig. 4.10). The measured quadratures fluctuate around a sinusoidal offset, and the standard deviation ΔQ of these fluctuations seems to be the same for each phase value, which indicates an equal distribution of the uncertainty in the quadratures $\hat{q}_\theta$ and $\hat{p}_\theta$. The average variance $(\Delta Q)^2$ of 0.5072 is very close to the theoretical minimum of 0.5 for a coherent state given by the uncertainty relation in Eq. (2.15). This first analysis indicates the presence of a coherent state.

With the algorithm outlined in section 3.2 it is possible to reconstruct the density matrix ρ_{mn} in the Fock basis from this data set. As explained in section 2.3.2, its diagonal elements ρ_{nn} represent the photon statistics of the underlying quantum state. They are shown in Fig. 4.11. For a coherent state, ρ_{nn} follows the Poisson distribution from Eq. (2.36) with a mean photon number of $\overline{n} = a^2/2 \approx 36.66$ that can be calculated with the help of the amplitude $a = \langle Q(\theta = \pi/2)\rangle$ of the coherent offset following Eq. (2.35). The diagonal elements ρ_{nn} and the Poisson distribution agree very well.

The Wigner function is better suited for a visual representation of a quantum state than the density matrix and can be calculated from the density matrix according to the methods outlined in section 3.3. This is shown in Fig. 4.12 for the phase-sensitive measurements of the LO as signal. Similar to the coherent state with $n = 1$ photons presented in Fig. 2.4a, it is a symmetric Gaussian distribution in phase space that is displaced from the origin by a. The scaled-down integral projections of the Wigner function (black dots) and the integral projections of the theoretical Wigner function of a coherent state with $n \approx 36.66$ (red lines) are provided on the walls of the plot. The reconstructed Wigner function and the theoretical model agree very well. However, the small ripples distributed around the Gaussian peak are a sign of imperfections, either of the measured quantum state or of the measurement setup. Still, the measured quantum state closely resembles all characteristics of a coherent state.

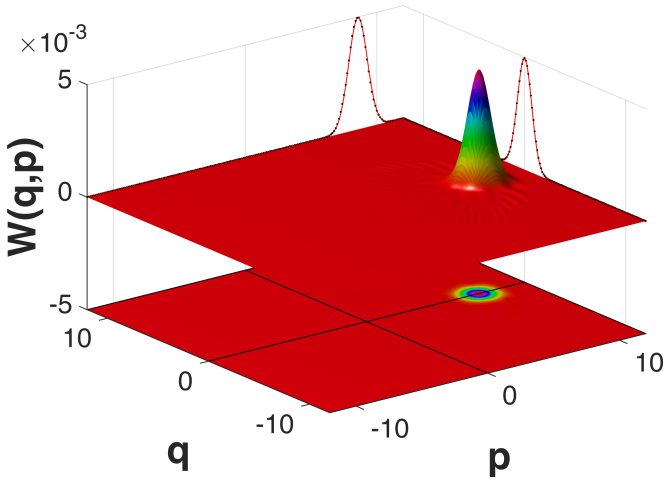

Figure 4.12.: Wigner function reconstructed from measurements of the LO as signal. Its scaled-down integral projections (black dots) are shown on the walls together with the theoretical integral projections (red lines) of a perfectly coherent Wigner function with $\overline{n} = 36.66$.

4.3. Correlated Quadratures

When performing phase-sensitive measurements on a coherent state, consecutive quadrature values Q_i are correlated due to the coherent offset discussed in the previous section. This means, for example, that Q_{i+1} probably has a high positive value when Q_i has one. There are other quantum states, such as the vacuum state or thermal states, where such correlations should not be present as all Q_i are drawn independently from the same symmetrical distribution centered at the origin of phase space. However, imperfections in the experimental setup can lead to unintended correlations among consecutive quadrature values. The 4-port homodyne detector discussed in this chapter introduces correlations of this sort as illustrated in the upper half of Fig. 4.13 for measurements on a thermal state. In this section, the correlations are quantified and an algorithm is presented that allows us to remove these correlations from the acquired quadrature values. After the application of this algorithm, no correlations are visible anymore, as shown in the lower half of Fig. 4.13.

For the calculation of the correlation coefficients, it is helpful to consider a series of quadrature measurements $\{Q_i\}$ as a series of vectors $\{\mathbf{a}_j\}$ with

$$\mathbf{a}_j = (Q_j, Q_{j+M}, Q_{j+2M}, \ldots, Q_{j+(N-1)\cdot M}) \tag{4.4}$$

and $j \in \{1, \ldots, M\}$. Modeling the data in this way is natural to the measurement process outlined in section 4.1.3, where M corresponds to the number of laser pulses acquired for a single trigger signal, and N corresponds to the total number of trigger signals used for the measurement. Mathematically, all expressions given for such vectors in this section are either drawn from or can be generalized for random variables, where normalized sums have to be replaced by expectation values.

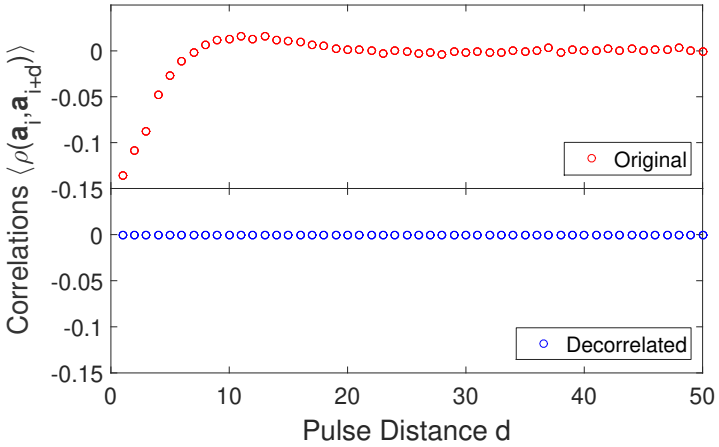

Figure 4.13.: Correlations between quadrature values from a thermal state measurement with a distance of d laser pulses. The original correlations are shown in the upper panel as red circles while the correlations after the compensation are shown in the lower panel as blue circles.

The correlation coefficient ρ between two vectors $\mathbf{a}$ and $\mathbf{b}$ is defined as[6]:

$$\rho(\mathbf{a},\mathbf{b}) = \mathrm{corr}(\mathbf{a},\mathbf{b}) = \frac{\sigma(\mathbf{a},\mathbf{b})}{\sqrt{\sigma(\mathbf{a},\mathbf{a})\sigma(\mathbf{b},\mathbf{b})}} \tag{4.5}$$

Here, $\sigma(\mathbf{a},\mathbf{b})$ is the covariance[6] of $\mathbf{a}$ and $\mathbf{b}$:

$$\sigma(\mathbf{a},\mathbf{b}) = \mathrm{cov}(\mathbf{a},\mathbf{b}) = \frac{1}{N-1}\sum_{i=1}^{N}(a_i-\mu_a)(b_i-\mu_b) \tag{4.6}$$

And μ_a is the arithmetic mean of the elements in $\mathbf{a}$:

$$\mu_a = \frac{1}{N}\sum_{i=1}^{N} a_i \tag{4.7}$$

The covariance of a vector with itself is simply the variance of this vector[6]:

$$\sigma(\mathbf{a},\mathbf{a}) = \mathrm{var}(\mathbf{a}) \tag{4.8}$$

The correlations $\langle\rho(\mathbf{a}_i,\mathbf{a}_{i+d})\rangle$ shown in Fig. 4.13 were calculated for different pulse distances d and averaged over all available vector pairs with the same distance in the data set. For small pulse distances, the correlation is negative with a minimum of about -0.14 for consecutive quadratures with a distance of only 1. It is monotonically increasing up to a pulse distance of about 10 where it becomes positive and from there approaches the zero line asymptotically. Around a distance of 20 pulses, correlations disappear, which justifies the use of $M = 1000 \gg 20$. This behavior is reproducible even for the vacuum

[6] e.g. [46, p. 93]

state and decreases the quality of the acquired quadrature values. The origin of those correlations probably lies within the electronics of the measurement setup but a detailed troubleshooting of the analog signal processing elements is out of the scope of this work.

Nevertheless, it is possible to model and remove such correlations in the digital data processing step. The following technique was adapted from Kumar et al. [43] and is analogous to the **Gram-Schmidt orthonormalization** method in linear algebra[7]. It starts with a set of correlated quadrature vectors $\mathbf{a}_j$ that consist of a weighted sum of the real quadrature vectors $\mathbf{b}_i$:

$$\mathbf{a}_j = \sum_{i=1}^{j} R_{i-j}\mathbf{b}_i = \sum_{i=1}^{j-1} R_{i-j}\mathbf{b}_i + R_0\mathbf{b}_j \tag{4.9}$$

The weights R_{i-j} describe by how much the value of the jth quadrature vector is affected by the value of the ith one. The sum in Eq. (4.9) starts at $i = 1$ because the set of measured values is finite and stops at j because it is assumed that a quadrature value is only affected by previously acquired quadrature values and not by future ones. Solving Eq. (4.9) for $\mathbf{b}_j$ results in a rule to calculate $\mathbf{b}_j$ as long as the vectors $\mathbf{b}_{i<j}$ are already known:

$$\mathbf{b}_j = \frac{1}{R_0}\left(\mathbf{a}_j - \sum_{i=1}^{j-1} R_{i-j}\mathbf{b}_i\right) \tag{4.10}$$

It is still necessary to find expressions for R_0 and R_{i-j}. An expression for R_{i-j} may be found by considering the **dot product** between a correlated quadrature vector $\mathbf{a}_j$ and a real quadrature vector $\mathbf{b}_i$:

$$\mathbf{a}_j \cdot \mathbf{b}_i \overset{(4.9)}{=} \sum_{k=1}^{j} R_{k-j}\ \mathbf{b}_k \cdot \mathbf{b}_i \approx R_{i-j}\ \mathbf{b}_i \cdot \mathbf{b}_i \tag{4.11}$$

This approximation holds true as long as $\mathbf{b}_k \cdot \mathbf{b}_i \ll \mathbf{b}_i \cdot \mathbf{b}_i$ for $k \neq i$. Even if the real quadratures are truly uncorrelated, $\mathbf{b}_k \cdot \mathbf{b}_i$ won't be exactly 0, because the random fluctuations of the quadratures always result in small random fluctuations of the dot product. The approximation gets better for higher vector lengths N because $\mathbf{b}_i \cdot \mathbf{b}_i$ grows faster than $\mathbf{b}_k \cdot \mathbf{b}_i$. Inserting Eq. (4.11) into Eq. (4.10) results in the final iterative compensation algorithm:

$$\mathbf{b}_j = \frac{1}{R_0}\left(\mathbf{a}_j - \sum_{i=1}^{j-1} \frac{\mathbf{a}_j \cdot \mathbf{b}_i}{\mathbf{b}_i \cdot \mathbf{b}_i}\mathbf{b}_i\right) \tag{4.12}$$

The final unknown quantity is the normalization factor R_0, which is a global scaling factor. The quadrature values shown in this work are normalized to the reference vacuum state measurements in order to conform to a variance of the vacuum state of 1/2

[7] see, for example, Landi and Zampini [47, p. 42 ff.]

(see section 4.1.3). This also defines R_0 as long as the correlation compensation is performed separately for the reference measurement ($LOonly$) and the signal measurement ($LOwithSIG$) before the scaling in Eq. (4.1) takes place. Therefore, $R_0 = 1$ can be assumed in the scope of this work. Applying this algorithm to the correlated quadrature measurements of a thermal state significantly reduces the observed correlations as shown in Fig. 4.13.

To summarize, this section shows that the 4-port homodyne detector described in this chapter adds small artificial correlations to the measured quadrature values. Furthermore, an algorithm is described which compensates these correlations in the data processing step. However, the algorithm can only be applied under special circumstances, when the acquired quadrature values are uncorrelated due to the nature of the underlying quantum state. This requirement is met, for example, for the vacuum state or a thermal state but not for a coherent state. As a rule of thumb, the compensation algorithm should not be applied when the investigated light field exhibits coherence times longer than the time between two LO pulses. In that case, consecutive quadrature measurements Q_i and Q_{i-1} are probably correlated because their phases θ_i and θ_{i+1} are correlated. In the scope of this work, the use of the compensation algorithm is always explicitly stated.

5. Real Time $g^{(2)}$ Monitoring

Apart from optical homodyne tomography, a 4-port homodyne detector is used in many other applications dealing with the amplitude or phase of a light field. In this chapter, for instance, quadrature measurements are used to gain insights into the coherence properties and photon statistics of light from a diode laser operated across the threshold region. If not indicated otherwise, the results presented in this chapter are based on the work published by Lüders, Thewes and Aßmann [48].

Photon statistics and coherence properties of light are studied in a broad range of areas in order to understand the characteristics and dynamics of light fields and their sources. By measuring temporal fluorescence correlations, for example, Magde et al. were able to obtain the chemical rate constants and diffusion coefficients for the reversible binding of ethidium bromide to DNA [49]. Another example is the observation of photon antibunching in light emitted from continuously excited sodium atoms by Kimble et al. [50], which is only understandable in terms of a quantized electromagnetic field. To distinguish photon bunching from antibunching, photon correlations have to be studied. Since photon correlations may correspond to classical intensity correlations, Hanbury Brown and Twiss called their device demonstrating photon bunching the first time an "intensity interferometer" [51]. Photon correlations can be quantified by the second-order correlation function $g^{(2)}(\tau)$ that can be interpreted as the conditional probability of detecting a second photon at time τ with respect to the detection of a first photon at time 0. This function is in detail discussed in section 5.1. With a 4-port homodyne detector, the equal-time second-order correlation $g^{(2)}(0)$ can be measured, which is already enough to distinguish different kinds of light with respect to their bunching behavior.

For meaningful $g^{(2)}(\tau)$ measurements, it is necessary to have a temporal resolution of $\Delta\tau$ that is smaller than the coherence time τ_c of the investigated light field. Otherwise, measurements of $g^{(2)}(0)$ do not correspond to the "real" values but to convolutions of the real values with $g^{(2)}(\tau > \tau_c) \approx 1$ [52]. Therefore, any investigated light field with $\Delta\tau \gg \tau_c$ would look the same with $g^{(2)}(\tau) = 1$. Many different experimental techniques have been developed to increase the temporal resolution into the femtosecond range. Among them are techniques based on two-photon absorption [53] or upconversion [54] as well as techniques using different detector technologies such as streak cameras [55] or balanced homodyne detectors [39].

These techniques are typically used to investigate light fields with stationary $g^{(2)}(\tau)$ values. Therefore comparatively long averaging times for a single $g^{(2)}(\tau)$ measurement are acceptable. There are, however, light fields where $g^{(2)}(\tau)$ may have an explicit time dependence. Such light may be emitted, for instance, by lasers that are subject to bistability or mode-hopping [56]. If the photon correlations change within the averaging time Δt of the detector, it is difficult to distinguish whether the measured $g^{(2)}(\tau)$ value

is fundamentally constant in time or a weighted average of a $g^{(2)}(\tau)$ function with an explicit time dependence. To make this distinction, techniques with short averaging times are needed.

The 4-port homodyne detector presented in chapter 4 provides both, a high temporal resolution of $\Delta\tau = 120\,\text{fs}$ and $g^{(2)}(0)$ averaging times down to $10\,\mu\text{s}$. This makes it possible to study multimode light fields that may show an explicit time dependence of $g^{(2)}(0)$. The capabilities of this technique are demonstrated in section 5.2 by monitoring the photon correlations and bistable emission of a diode laser across the threshold region. The high sampling rate of 100 kHz opens up the way to perform real time monitoring of $g^{(2)}(0)$.

5.1. The Second-Order Correlation Function $g^{(2)}(\tau, t)$

The second-order correlation function[1] is given by:

$$g^{(2)}(\tau,t) = \frac{\left\langle \hat{a}^\dagger(t)\hat{a}^\dagger(t+\tau)\hat{a}(t+\tau)\hat{a}(t)\right\rangle}{\left\langle \hat{a}^\dagger(t)\hat{a}(t)\right\rangle \left\langle \hat{a}^\dagger(t+\tau)\hat{a}(t+\tau)\right\rangle} \tag{5.1}$$

Here, $\hat{a}^\dagger$ and $\hat{a}$ are the bosonic creation and annihilation operators for the light mode under investigation. The expectation values in Eq. (5.1) may be interpreted differently for pulsed and continuous wave light fields. For pulsed fields, they may be considered as ensemble averages over statistical ensembles of identically prepared pulses. Aßmann et al., for instance, tracked the evolution of $g^{(2)}(0,t)$ during the course of the emission pulse of quantum-dot microresonator lasers in this way [57]. For continuous wave light fields, those expectation values may be considered as time averages over a time interval Δt. This interval can be chosen differently for different applications depending on the required precision of the averages.

Moreover, it should be emphasized that Eq. (5.1) features two relevant timescales. The first timescale corresponds to the delay τ and the temporal resolution $\Delta\tau$ in τ of the experimental setup. As discussed earlier, $g^{(2)}(\tau > \tau_c, t) = 1$ applies for any light field and therefore $\Delta\tau \leq \tau_c$ should be guaranteed for meaningful measurements. The second relevant timescale corresponds to the time t and the sampling time Δt. For pulsed light fields, the sampling time is often equal to the time resolution, because the averaging occurs over identically prepared pulses without losing precision during a single pulse. For continuous wave light fields, however, the sampling time $\Delta t \gg \Delta\tau$ is usually much longer than the temporal resolution. In such cases it is mainly determined by the sampling rate of the quantities inside the brackets $< \ldots >$ of Eq. (5.1) used for averaging and the necessary number of samples to achieve the required precision. The 4-port homodyne detector from Fig. 4.2, for example, allows for one phase-dependent photon number measurement every 13.3 ns. As 754 of them are used to obtain one $g^{(2)}(0)$ value presented in section 5.2, the sampling time of the setup in this configuration is about $10\,\mu\text{s}$.

[1] see, for example, the textbook by Fox [21, p. 161]

With the 4-port homodyne detector used for the results in this chapter, only the equal-time second-order correlation function $g^{(2)}(0,t)$ of the signal light is accessible. It is given by:

$$g^{(2)}(\tau = 0) = \frac{\left\langle \hat{a}^\dagger \hat{a}^\dagger \hat{a} \hat{a} \right\rangle}{\left\langle \hat{a}^\dagger \hat{a} \right\rangle \left\langle \hat{a}^\dagger \hat{a} \right\rangle} \tag{5.2}$$

The dependencies of $g^{(2)}$ and different quantum mechanical operators on t are often omitted to improve readability. Light from an ideal diode laser is usually in one of two quantum states. Above the lasing threshold, it is in a coherent state, and below the lasing threshold in a thermal state. As $g^{(2)}(0)$ measurements were performed across the lasing threshold, it is important to know the predicted $g^{(2)}(0)$ values for both cases.

As discussed in section 2.4, a coherent state can be described by a Dirac ket vector $|\alpha\rangle$, which is an eigenstate of the annihilation operator $\hat{a}$. This property is already sufficient to compute the two expectation values $\left\langle \hat{a}^\dagger \hat{a}^\dagger \hat{a} \hat{a} \right\rangle$ and $\left\langle \hat{a}^\dagger \hat{a} \right\rangle$ needed to work out Eq. (5.2):

$$\langle \alpha | \, \hat{a}^\dagger \hat{a}^\dagger \hat{a} \hat{a} \, | \alpha \rangle \overset{(2.25)}{=} \bar{\alpha} \bar{\alpha} \alpha \alpha = |\alpha|^4 \tag{5.3}$$

$$\langle \alpha | \, \hat{a}^\dagger \hat{a} \, | \alpha \rangle \overset{(2.25)}{=} \bar{\alpha} \alpha = |\alpha|^2 \tag{5.4}$$

The resulting equal-time second-order correlation function is then equal to one:

$$g^{(2)}_{\text{coh}}(0) = \frac{\langle \alpha | \, \hat{a}^\dagger \hat{a}^\dagger \hat{a} \hat{a} \, | \alpha \rangle}{\langle \alpha | \, \hat{a}^\dagger \hat{a} \, | \alpha \rangle \langle \alpha | \, \hat{a}^\dagger \hat{a} \, | \alpha \rangle} = \frac{|\alpha|^4}{|\alpha|^2 \cdot |\alpha|^2} = 1 \tag{5.5}$$

For a thermal state, it is possible to compute $g^{(2)}(0)$ with the help of the thermal density operator $\hat{\rho}^{\text{th}}$. The corresponding density matrix ρ^{th}_{mn} in the Fock basis is a diagonal matrix and the diagonal elements $\rho^{\text{th}}_{nn} = P(n)$ are probabilities given by the Bose-Einstein distribution from Eq. (2.38). To simplify the calculation, it is useful to express Eq. (5.2) in terms of the well known photon number operator $\hat{n} = \hat{a}^\dagger \hat{a}$:

$$\hat{a}^\dagger \hat{a}^\dagger \hat{a} \hat{a} \overset{(2.9)}{=} \hat{a}^\dagger \hat{a} \hat{a}^\dagger \hat{a} - \hat{a}^\dagger \hat{a} = \hat{n}^2 - \hat{n} \tag{5.6}$$

$$\Rightarrow \qquad g^{(2)}_{\text{th}}(0) = \frac{\langle \hat{n}^2 \rangle - \langle \hat{n} \rangle}{\langle \hat{n} \rangle^2} \tag{5.7}$$

According to Eq. (2.23) expectation values can be computed as traces over the product of the density operator with the operator of interest. In the following, $\bar{n}$ is the average number of photons in the considered quantum state:

$$\begin{aligned} \langle \hat{n} \rangle &\overset{(2.23)}{=} \text{tr}\left[\hat{n} \hat{\rho}^{\text{th}}\right] \overset{(2.24)}{=} \sum_{l=0}^{\infty} l \rho^{\text{th}}_{l,l} \\ &\overset{(2.38)}{=} \sum_{l=0}^{\infty} l \frac{\bar{n}^l}{(\bar{n}+1)^{l+1}} \overset{(A.2)}{=} \bar{n} \end{aligned} \tag{5.8}$$

$$\left\langle \hat{n}^2 \right\rangle = \sum_{l=0}^{\infty} l^2 \rho_{l,l}^{\mathrm{th}} \overset{(A.3)}{=} 2\bar{n}^2 + \bar{n} \tag{5.9}$$

The infinite sums are calculated with the help of the formulas given in appendix A. The equal-time second-order correlation function of a thermal state then amounts to two:

$$g_{\mathrm{th}}^{(2)}(0) = \frac{\left\langle \hat{n}^2 \right\rangle - \left\langle \hat{n} \right\rangle}{\left\langle \hat{n} \right\rangle^2} = \frac{2\bar{n}^2 + \bar{n} - \bar{n}}{\bar{n}^2} = 2 \tag{5.10}$$

This shows that it is possible to distinguish coherent light from thermal light by measuring $g^{(2)}(0)$ with a precision that allows one to distinguish $g^{(2)}(0) = 1$ from $g^{(2)}(0) = 2$.

However, a 4-port homodyne detector does not provide direct measurements of the photon number operator $\hat{n}$ but of the quadrature operator $\hat{q}_\theta$. Therefore, it is necessary to establish a link between $g^{(2)}(0)$ and measurements Q_i of the operator $\hat{q}_\theta$. The fact that $\hat{q}_\theta$ consists of a sum of two terms that are linear in $\hat{a}^\dagger$ and $\hat{a}$, respectively, provides a strategy that results in the desired link. The basic idea is to compute the moments $\langle \hat{q}_\theta^2 \rangle$ and $\langle \hat{q}_\theta^4 \rangle$, which include products of two or four ladder operators, to find suitable expressions for $\left\langle \hat{a}^\dagger \hat{a}^\dagger \hat{a} \hat{a} \right\rangle$ and $\left\langle \hat{a}^\dagger \hat{a} \right\rangle$ that can be calculated from $\hat{q}_\theta$:

$$\begin{aligned} \left\langle \hat{q}_\theta^2 \right\rangle &\overset{(2.7)}{=} \frac{1}{2} \left\langle \left(e^{i2\theta} \hat{a}^\dagger \hat{a}^\dagger + e^{-i2\theta} \hat{a}\hat{a} + \hat{a}^\dagger \hat{a} + \hat{a}\hat{a}^\dagger \right) \right\rangle \\ &\overset{(2.9)}{=} \frac{1}{2} \underbrace{\left(\left\langle e^{i2\theta} \hat{a}^\dagger \hat{a}^\dagger \right\rangle + \left\langle e^{-i2\theta} \hat{a}\hat{a} \right\rangle \right)}_{=0 \text{ for random } \theta} + \left\langle \hat{a}^\dagger \hat{a} \right\rangle + \frac{1}{2} \end{aligned} \tag{5.11}$$

$$\begin{aligned} \left\langle \hat{q}_\theta^4 \right\rangle &\overset{(2.7)}{=} \frac{1}{4} \left\langle \hat{a}^\dagger \hat{a}^\dagger \hat{a}\hat{a} + \hat{a}^\dagger \hat{a} \hat{a}^\dagger \hat{a} + \hat{a}^\dagger \hat{a}\hat{a}\hat{a}^\dagger + \hat{a}\hat{a}^\dagger \hat{a}^\dagger \hat{a} + \hat{a}\hat{a}^\dagger \hat{a}\hat{a}^\dagger + \hat{a}\hat{a}\hat{a}^\dagger \hat{a}^\dagger \right\rangle \\ &\quad + \underbrace{\left\langle \mathcal{O}\left(e^{\pm i2\theta}\right) + \mathcal{O}\left(e^{\pm i4\theta}\right) \right\rangle}_{=0 \text{ for random } \theta} \\ &\overset{(2.9)}{=} \frac{1}{4} \left(6 \left\langle \hat{a}^\dagger \hat{a}^\dagger \hat{a}\hat{a} \right\rangle + 12 \left\langle \hat{a}^\dagger \hat{a} \right\rangle + 3 \right) \end{aligned} \tag{5.12}$$

The expectation values of the phase dependent terms in Eqs. (5.11) and (5.12) become zero when the measurement is performed with a randomized phase θ. It is now possible to express the equal-time second-order correlation function in terms of the quadrature operator $\hat{q}_\theta$:

$$g^{(2)}(0) = \frac{\left\langle \hat{a}^\dagger \hat{a}^\dagger \hat{a}\hat{a} \right\rangle}{\left\langle \hat{a}^\dagger \hat{a} \right\rangle^2} = \frac{4 \left\langle \hat{q}_\theta^4 \right\rangle - 12 \left\langle \hat{q}_\theta^2 \right\rangle + 3}{\left(\left\langle \hat{q}_\theta^2 \right\rangle - \frac{1}{2} \right)^2} \tag{5.13}$$

It is important to emphasize that the use of Eq. (5.13) only produces meaningful results when two requirements are met. First, the quadrature measurement has to be performed in a phase-averaged manner. And second, the time resolution $\Delta\tau$ of the experimental setup has to fulfill $\Delta\tau < \tau_c$, as discussed in the beginning of this section.

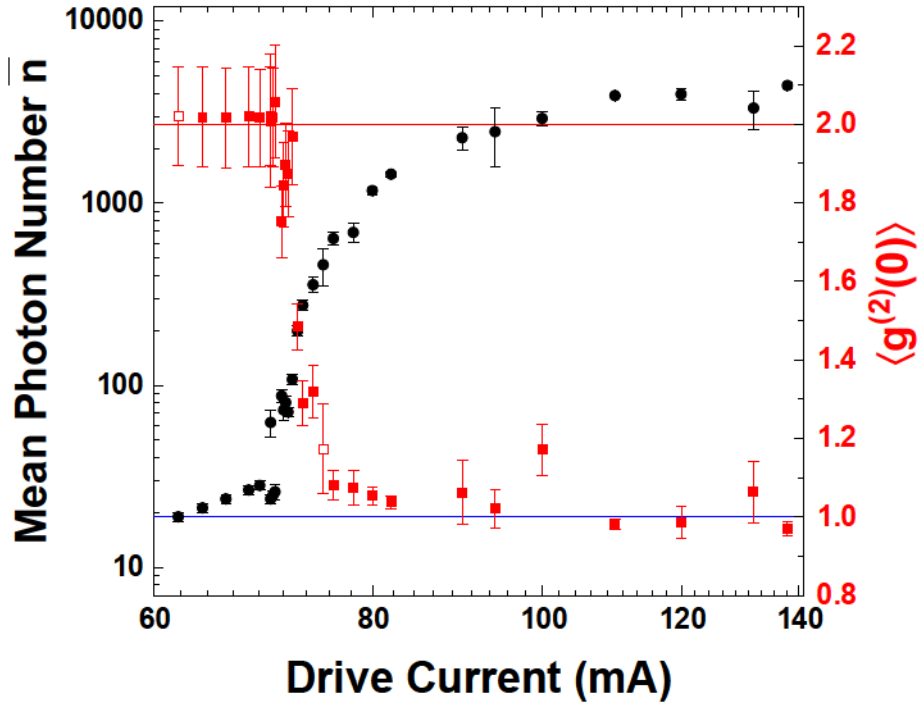

Figure 5.1.: Time-averages of equal-time second-order correlation function $\langle g^{(2)}(0)\rangle$ (red squares) and mean photon number $\bar{n}$ (black dots) for different diode laser drive currents across the lasing threshold. The two empty squares point to the drive currents investigated in Fig. 5.2. The expected values for coherent light (blue line) and thermal light (red line) are 1 and 2. Adapted from [48].

5.2. Results and Discussion

The capabilities of the 4-port homodyne detector presented in chapter 4 as a fast $g^{(2)}(0)$ monitor are demonstrated by investigating the photon correlations of the external cavity diode laser from section 4.1 across its lasing threshold. The central wavelength of the LO and the laser emission of the diode laser were set to 835 nm. Moreover, the diode laser feedback was slightly misaligned in order to prevent the laser from showing ideal single mode operation. The LO features a Fourier transform limited spectral width of 9.3 nm, while the diode laser below threshold shows a broad Gaussian shaped thermal emission with a central wavelength of 830 nm and width of 22.9 nm. In general, the requirement of homodyne detection to overlap the LO spectrally with the signal modes under study is seen as a limitation. In the experiments presented in this chapter, however, the broad LO spectrum allows for interrogating all lasing modes of the diode laser and a significant portion of its thermal modes. Furthermore, the automatic spectral filtering of the thermal signal modes is an advantage because the modes that overlap with the LO have a coherence time at least comparable to $\Delta\tau$, which is necessary for meaningful $g^{(2)}(0)$ measurements.

The data sets taken for each diode laser drive current consist of 16 million phase-

averaged consecutive quadrature measurements that are organized into 21455 batches of 754 data points each. Hence, each data set covers a time period of about 210 ms. One value of $g^{(2)}(0)$ is calculated for each batch, which results in a sampling time of $\Delta t = 10\,\mu s$. The coherence time τ_c of the emitted light is several orders of magnitude lower than Δt for each drive current and at the same time larger than the time resolution $\Delta\tau$. The former property ensures the phase-averaging requirement, while the latter one prevents the convolution of the real $g^{(2)}(0)$ values with $g^{(2)}(\tau > 1) \approx 1$. In the following, the results of analyzing the averages, the time series and the histograms of the acquired $g^{(2)}(0,t)$ data are discussed.

At the lasing threshold, $g^{(2)}(0)$ is expected to drop from 2 to 1, while the mean photon number $\bar{n}$ should rise sharply. Figure 5.1 compares the results obtained from time-averaging $g^{(2)}(0)$ and $\bar{n}$ for different drive currents. Here, the error bars correspond to the standard deviations of the averaged data. The results match the expected behavior, and the transitions take place at a threshold drive current of about 70.5 mA. Interestingly, several $\langle g^{(2)}(0)\rangle$ data points show relatively large standard deviations. For a drive current of 75 mA, for instance, the standard deviation is much larger than for the surrounding drive currents. However, it is comparable to the standard deviation for 62 mA, which is below the lasing threshold. The number of photons at a drive current of 62 mA is several orders of magnitude lower than for 75 mA and the standard deviation is therefore expected to be higher. This is also indicated by the drive currents surrounding 62 mA. Figure 5.1 does not provide enough information to find the origin of this discrepancy.

The time series shown in Fig. 5.2 illustrate that the standard deviations of $g^{(2)}(0)$ for 62 mA and 75 mA have different origins. Below the lasing threshold, at 62 mA, the fluctuations of $g^{(2)}(0)$ around the value of 2 expected for thermal light seem to be of purely statistical nature. This is supported by the fact that the magnitude of these fluctuations becomes smaller, when larger values for Δt are chosen (not shown). In contrast, the $g^{(2)}(0)$ fluctuations for 75 mA appear to have a mainly physical origin rather than a statistical one. The $g^{(2)}(0)$ values move back and forth between two distinct values around 1.1 and 1.2. The time between the switching events seems to be around several milliseconds, while there is no obvious periodicity. At the same time, also the mean photon number $\bar{n}$ moves back and forth, mostly between 550 and 450 photons. High values of $g^{(2)}(0)$ are correlated with low values of $\bar{n}$ and vice versa. This leads to the conclusion that the standard deviations of the averaged values in Fig. 5.1 are a result of averaging over both distinct states instead of averaging over only a single stable state.

A possible explanation for this behavior might be that the diode laser operates in two modes with a bistable profile, which is a sign of mode competition. Bistable operation means that only one mode is in an "on" state at a time. Multimode operation differs from bistable operation such that both modes would oscillate simultaneously. Bistabilities as well as multimode operation are well known phenomena observed in the emitted intensity, and therefore in the mean photon number $\bar{n}$, of semiconductor lasers [56]. What is interesting is that the second-order correlation function shares this bistable

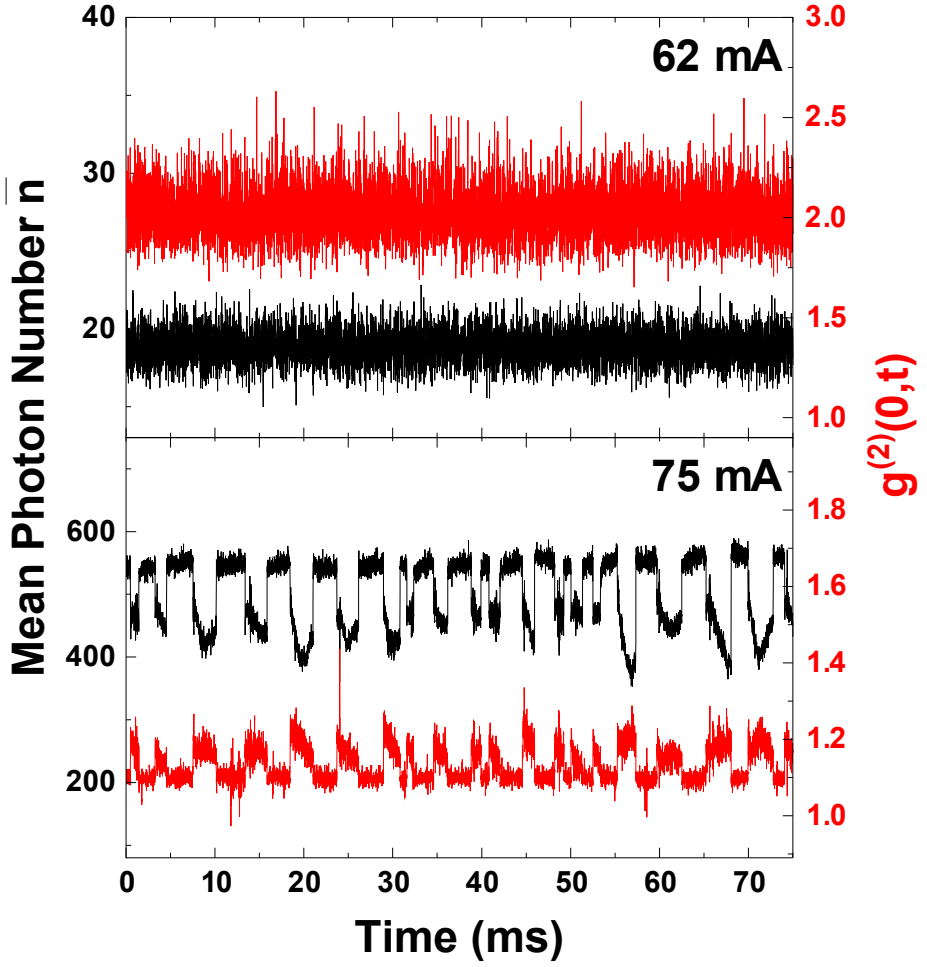

Figure 5.2.: Time series of $g^{(2)}(0)$ and $\bar{n}$ for drive currents of 62 mA and 75 mA. The threshold current amounts to 70.5 mA. At 75 mA, higher photon numbers are correlated with lower $g^{(2)}$ values and vice versa. Adapted from [48].

behavior. However, there are certain differences worth mentioning. Between 55 ms and 60 ms, for instance, the mean photon number drops from about 450 to 375 within one of the modes while $g^{(2)}(0)$ stays approximately the same at 1.2. Hence, a detailed study of the temporal dynamics of $\bar{n}$ and $g^{(2)}(0)$ may provide deeper understanding of the mode hopping behavior and the modes themselves. However, this is out of the scope of the present work.

While the time traces in Fig. 5.2 provide a detailed picture of the laser mode dynamics during a short window of time, the histograms shown in Fig. 5.3 allow for a quantitative analysis of longer time frames. They represent the relative frequencies of different $g^{(2)}(0)$ values during the 210 ms time window acquired for each drive current. The two histograms for the drive currents of 75 mA and 62 mA are drawn in red and provide additional information about the discussed mode dynamics. At 62 mA, the histogram has a broad Gaussian shape that is centered on $g^{(2)}(0) = 2$, which is expected for thermal

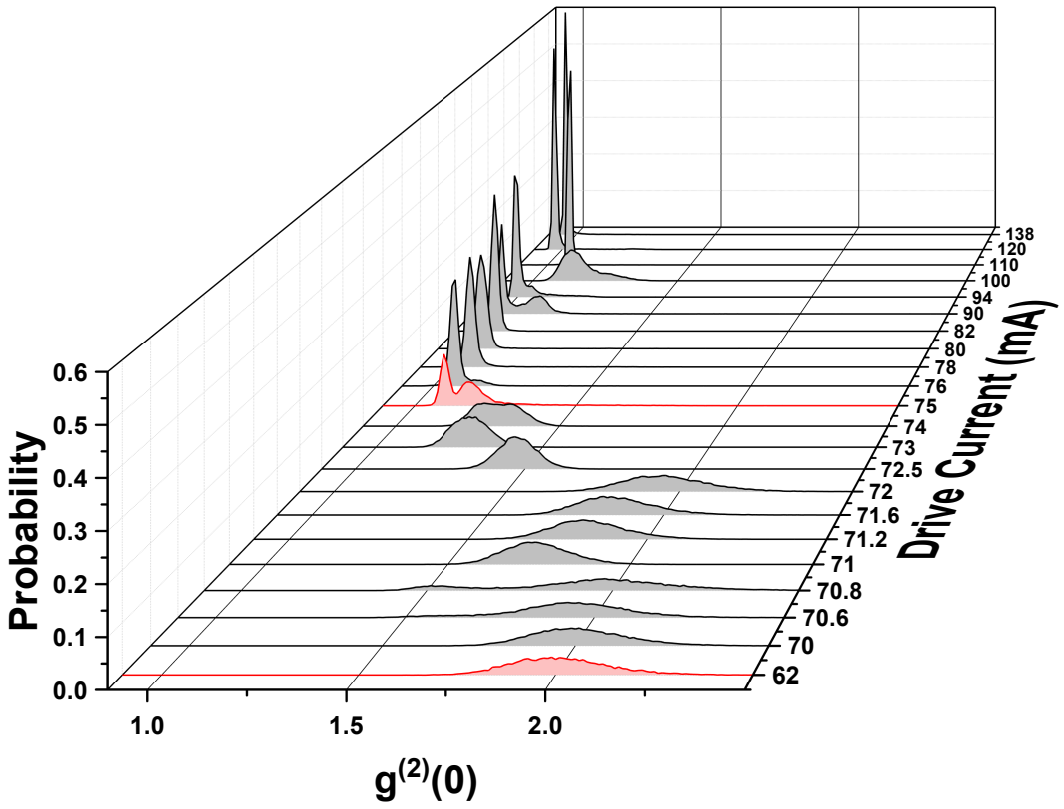

Figure 5.3.: Histograms of $g^{(2)}(0)$ for different diode laser drive currents. The time series from Fig. 5.2 are marked in red. In order to improve the visibility of the histograms, the drive current axis is not linearly scaled. Adapted from [48].

emission below threshold. For 75 mA, there are two overlapping Gaussian shaped peaks instead of one. The narrower one is centered on $g^{(2)}(0) \approx 1.1$ while the broader one is centered on $g^{(2)}(0) \approx 1.2$ and both peaks have a similar strength. This splitting is a sign of the bistability discussed above and the histogram representation allows us to access the relative strength and width of both modes. Hence, the histogram is a useful tool to distinguish physical and statistical influences on the standard deviations in Fig. 5.1.

A further investigation of the histograms in Fig. 5.3 reveals that the bistable behavior occurs at 70.8 mA for the first time with a weak narrower mode appearing close to $g^{(2)}(0) = 1.5$ while the dominant broader mode is still close to 2. The bistability vanishes with the next drive current at 71 mA, where only one broad mode around $g^{(2)}(0) = 1.75$ is visible. For higher drive currents up to 72 mA, the emission stays in a single mode but the average $g^{(2)}(0)$ value is increasing to the value of 2 again. This is surprising because higher drive currents are expected to result in more coherent light with $g^{(2)}(0)$ closer to 1. One possible explanation could be that the bistable mode dynamics at 70.8 mA change to multimode dynamics. In this case, both modes coexist independently of each other, while their relative intensities determine whether the encountered $g^{(2)}(0)$ values are closer to 1.5 or 2. In this model, the relative intensities of the two modes change for higher drive currents and therefore the second-order correlation values move closer to the one determined by the stronger mode.

Inside the transition region from thermal emission to coherent emission, histograms with one Gaussian peak, such as at 72.5 mW, alternate with histograms with two Gaussian peaks, such as at 75 mA. This might be interpreted as an alternation between stable operation and bistable operation of the diode laser. Stable lasing operation is achieved at about 80 mW with a very narrow distribution of $g^{(2)}(0)$ values around 1. The narrowest distribution seems to appear at the highest drive current shown at 138 mW. Nonetheless, there are still some regions of bistability for drive currents higher than 80 mA, such as at 90 mA, that are probably due to the slight misalignment of the diode laser feedback.

5.3. Conclusion

The purpose of the current chapter was to present an experimental technique which provides a way to monitor the equal-time second-order correlation function $g^{(2)}(0)$ in real time. The temporal resolution of the underlying quadrature measurements is about 120 fs and therefore allows for studying light fields with very low coherence times down to this value. Real time monitoring is enabled by the low sampling time of only 10 µs for each $g^{(2)}(0)$ value. However, this sampling time is not fixed but can be tailored to the specific requirements of the application by averaging over either more or fewer quadrature values, which likely results in lower or larger statistical fluctuations. The capabilities of this $g^{(2)}$ monitor were demonstrated by investigating the emission of an external cavity diode laser across the lasing threshold. Mode dynamics could be studied by monitoring the mean photon number $\bar{n}$ and $g^{(2)}(0)$ with a sampling time of 10 µs. Bistabilities as well as possible multimode emission could be successfully identified.

Possible applications range from investigating the coherence properties of nanolasers

[58] over time-resolved photon correlation measurements with respect to feedback [59] to research on spontaneously occurring phenomena that need to be studied in real time because they do not yield a trigger signal, such as superradiance [60]. The experimental setup can also be advanced by using additional homodyne detection channels. In this way, shorter sampling times become feasible by adjusting the delay between the channels accordingly. Alternatively, different modes of the same emitter can be selected with different channels to study, for example, mode competition in bimodal lasers in real time [61]. Such a setup with multiple homodyne detection channels is presented in the next chapter.

6. Non-Stationary Optical Homodyne Tomography

As mentioned in chapter 2, mixed quantum states arise during the investigation of statistical ensembles. In fact, OHT experiments perform such measurements on statistical ensembles, where the signal light field sampled within a single LO pulse is its own quantum system in its own instantaneous state. If all of these states are the same, one can say that the light field is in a pure state and all available information can be captured with stationary OHT. Otherwise, if the states change from one LO pulse to the next, the light field is in a mixed state and these changes can be interpreted as a temporal evolution of the light field. For mixed states, stationary OHT may be improved in two ways: first, when capturing additional information that allows one to assign acquired quadrature values to specific instantaneous states composing the ensemble, it can become possible to select on these states *a posteriori*. Second, being able to select on one of these instantaneous states at zero time allows one to look at the quantum state found after some delay, which allows for time-dependent studies. A technique designed to accomplish both of these tasks is introduced in this chapter.

As discussed in chapter 4, the availability of a priori information about the phase of the signal light field is central to the entire process of stationary OHT with a 4-port HD. When the light field under investigation is a statistical ensemble of distinct instantaneous states, however, its phase may fluctuate strongly. By employing a 12**-port homodyne detector** (HD) instead of a 4-port one, it becomes possible to reconstruct the quantum state of such light fields. The basic idea of a 12-port HD is to measure the phase of the signal light field with 8 of the 12 ports for each LO pulse separately and to use this as a priori information to reconstruct the quantum state detected with the remaining 4 ports. This may open up the possibility for detailed studies on light fields in mixed states, which do not have a fixed phase relationship with the local oscillator, such as thermal light fields. In fact, most light fields not emitted by processes stimulated by the local oscillator fall into this category. Hence, such a 12-port homodyne detector grants access to the Wigner function of any light field that overlaps spectrally, temporally, spatially and in polarization with the LO. By delaying the 4-port homodyne detector in time, conditional studies are possible. This means that we reconstruct a quantum state after some delay τ when specific conditions are met before. These conditions can be determined *a posteriori* from measurements of the remaining 8-port homodyne detector. Since this allows one to capture the time-dependencies of light fields in mixed states, optical homodyne tomography with a 12-port homodyne detector is called **non-stationary OHT**.

The contents of this chapter is divided into three parts. The theoretical implications

of using 12 instead of 4 ports are discussed using the example of a thermal state. First, it is shown that the additional information about the phase of the light fields results in a slightly lower precision of the measurements. Second, the 12-port homodyne detection setup is presented together with the results from phase-sensitive, but time independent measurements on thermal light generated by a diode laser below threshold. In the third part, the results of time-dependent studies on the same light source are presented and discussed. Some contents of this chapter are also part of a manuscript titled "Non-stationary optical homodyne quantum state tomography reveals hidden dynamics of light fields", which is submitted for publication (see list of publications for details).

6.1. Theory of 12-Port Homodyne Detection of a Thermal State

A 12-port HD can be considered as a combination of three 4-port HDs. Figure 6.1 illustrates the working principle of the 12-port HD used for the results presented in this chapter. In this scheme, the signal quantum state $\hat{\rho}_s$ has to be distributed onto three 4-port HDs by means of two beam splitters. For this purpose, three copies of the signal state are created. Since perfect cloning of a quantum state is impossible [62], measurements of $\hat{\rho}_s$ with this setup suffer from additional noise injected by the copying procedure itself. This section aims at quantifying the limitations of stationary OHT imposed by this experimental scheme. As a test state, the reconstructed Wigner function of a thermal state measured with a 12-port HD was computed. This allows us to derive the fundamental limitations regarding fluctuations of the reconstructed quantum state.

The first beam splitter (BS1) in Fig. 6.1 divides the signal state $\hat{\rho}_s$ into the **target state** $\hat{\rho}_t$ and the **postselection state** $\hat{\rho}_{ps}$. The second beam splitter (BS2) further divides $\hat{\rho}_{ps}$ into the two states $\hat{\rho}_{p1}$ and $\hat{\rho}_{p2}$. The three states $\hat{\rho}_{p1}$, $\hat{\rho}_{p2}$, and $\hat{\rho}_t$ are then detected separately by the three 4-port homodyne detectors HD1, HD2, and HD3. The splitting ratio of BS2 is chosen as 50 %, while the reflection coefficient r and the transmission coefficient t describe the splitting ratio of BS1. On each beam splitter input port where no signal light is present, a vacuum state is incident. A $\pi/2$ phase shifter in front of HD1 ensures that $\hat{\rho}_{p1}$ and $\hat{\rho}_{p2}$ have a phase difference of $\pi/2$ and therefore HD1 and HD2 perform measurements of the complementary observables $\hat{q}_\theta$ and $\hat{p}_\theta$.

In order to compute the Wigner function of the target quantum state $\hat{\rho}_t$, it is important to understand the setup from Fig. 6.1 in a phase space context. In that context, any quantum state of light can be described by one of infinitely many and equivalent phase space distribution functions (e.g. [26, p. 321]). However, only three of those functions are relevant for the calculations in this chapter, one being the Wigner function, which was introduced in section 2.3.1, and the other two being the Husimi–Kano Q–function[1] and the Glauber–Sudarshan P–function[2]. They are associated with symmetric, antinormal,

[1] e.g. in the textbook from Schleich [26, p. 324 ff.] or the papers from Husimi [63] and Kano [64]
[2] e.g. in the textbook of Schleich [26, p. 337 ff.] or the papers from Glauber [65] and Sudarshan [66]

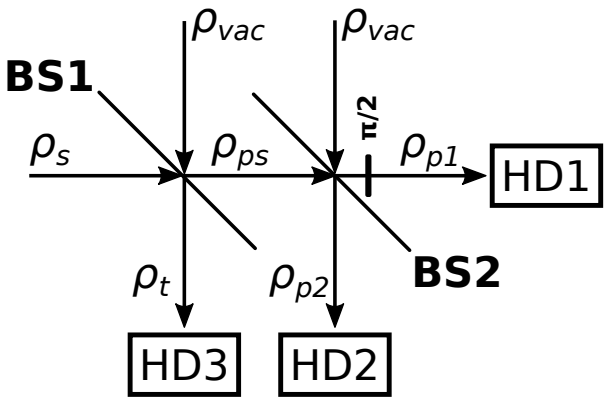

Figure 6.1.: 12-port homodyne detector for optical homodyne tomography. ρ indicates the density operator $\hat{\rho}$ of the corresponding quantum state. The signal quantum state $\hat{\rho}_s$ is distributed among the 4-port homodyne detectors HD1, HD2 and HD3 by the two beam splitters BS1 and BS2. Further details are discussed in the text.

or normal operator ordering, respectively. Hence, one can evaluate expectation values of quantum mechanical operators using one of these distribution functions provided that the operators are first ordered accordingly [26, p. 322]. In the present work, the Wigner function is the most important of them because homodyne detection allows one to directly access its integral projections.

Figure 6.2 compares the P-function, the Wigner function and the Q-function of a thermal state featuring a mean photon number of $\bar{n} = 1$. All of them are Gaussian shaped but differ in width. The narrowest distribution is the P-function followed by the Wigner function and the Q-function. Mathematically, those three phase space functions are connected to each other by a convolution with the vacuum Wigner function. Consequently, the Wigner function can be derived from the P-function and the Q-function can be derived from the Wigner function by this convolution (see Eqs. (A.5) and (A.4)). These convolutions may be interpreted as a kind of smoothing. The P-function of a coherent state, for instance, is a Dirac delta function [26, p. 338]

$$P(\alpha) = \delta(\alpha - \alpha_0) \tag{6.1}$$

since the corresponding Wigner function is a displaced vacuum Wigner function, which is the convolution of a displaced Dirac delta function with a vacuum Wigner function.

In equation (6.1), the P-function is formulated in terms of the phase space variables $\alpha_r = \mathrm{Re}(\alpha)$ and $\alpha_i = \mathrm{Im}(\alpha)$. The complex number α is the eigenvalue of the annihilation operator $\hat{a}$, and the corresponding phase space is usually called **α-space**. Especially when considering coherent states, which are eigenstates of $\hat{a}$, it is advantageous to use the α-space instead of the representation in terms of the quadrature variables q and p introduced in section 2.3.1. The two representations are connected by the following

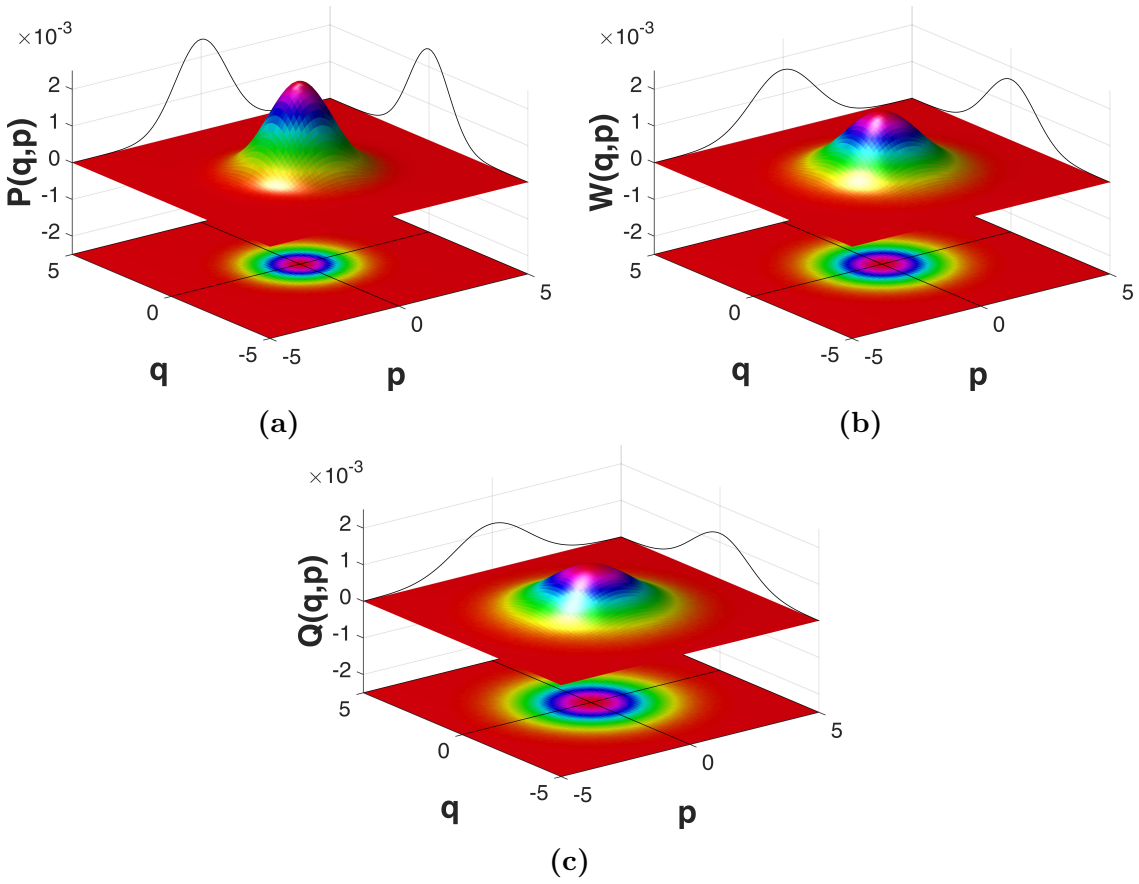

Figure 6.2.: (a) Glauber-Sudarshan P-function, (b) Wigner function, and (c) Husimi-Kano Q-function of a thermal state with $\bar{n} = 1$ photons.

substitutions[3]:

$$q \to \sqrt{2}\alpha_r \tag{6.2}$$

$$p \to \sqrt{2}\alpha_i \tag{6.3}$$

$$dqdp \to 2\alpha_r\alpha_i \tag{6.4}$$

The importance of the Q-function for subsequent calculations arises from the fact that it is directly accessible in experiments [67, 68]. To measure the Q-function, two homodyne detection channels in the configuration of an 8-port interferometer with a $\pi/2$ phase shifter in front of one channel are required. Then, the 8–port HD measures the Q–function of the input state through its count statistics [26, p. 361 ff.]. In the scheme provided in Fig. 6.1, the homodyne detection channels HD1 and HD2, together with the beam splitter BS2 and the phase shifter, represent exactly such an 8-port interferometer. This type of setup may be used to measure the Q-function of the postselection state $\hat{\rho}_{ps}$.

The P-function is required for the following calculations, because it allows us to represent any density operator $\hat{\rho}$ in a diagonal representation of coherent states, as discussed in [26, p. 337],

$$\hat{\rho} = \int P(\alpha) \left|\alpha\right\rangle \left\langle\alpha\right| d^2\alpha \tag{6.5}$$

and each quantum state of a light field can be described by a density operator. Therefore, in a diagonal representation of coherent states using the P-function, the transformation of any input quantum states on a beam splitter into output quantum states can be understood by considering only coherent states. For a lossless beam splitter, the reciprocity relations connecting the complex reflection coefficient r_1, the transmission coefficient t_1, and the corresponding coefficients r_2 and t_2 for light incident from the opposite direction are [37]:

$$|r_1| = |r_2| \tag{6.6}$$

$$|t_1| = |t_2| \tag{6.7}$$

$$|r_1|^2 + |t_1|^2 = 1 \tag{6.8}$$

$$r_1^\star t_2 + t_1^\star r_2 = 0 \tag{6.9}$$

In the case of beam splitter BS1 shown in Fig. 6.3a, the classical amplitudes i_1 and i_2 of the light modes incident on the beam splitter transform into the output amplitudes o_1 and o_2 as:

$$o_1 = t_1 i_1 + r_2 i_2 \tag{6.10}$$

$$o_2 = r_1 i_1 + t_2 i_2 \tag{6.11}$$

To make the transition to quantum mechanics, the mode amplitudes are replaced with annihilation operators of the corresponding light modes. Since coherent states are eigenstates of these operators, coherent states transform in the same way as the mode amplitudes [26, p. 354]. However, in quantum mechanics it is necessary to specify the

[3] see, for example, the discussion in [26, p. 322 ff.]

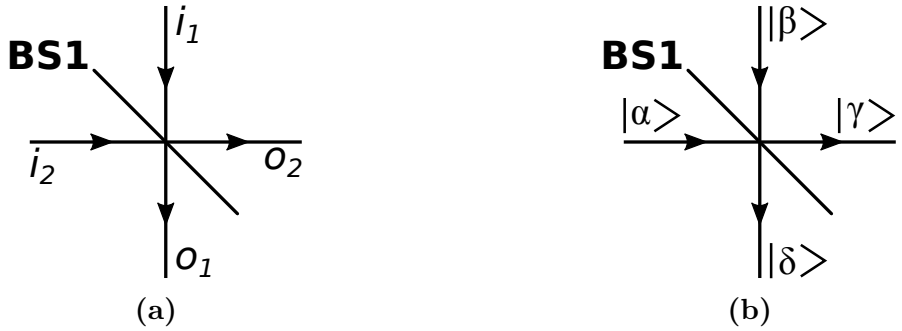

Figure 6.3.: Illustration of the lossless beam splitter BS1 from Fig. 6.1 for (a) the classical amplitudes of ingoing (i_1, i_2) and outgoing (o_1, o_2) modes of light and (b) ingoing ($|\alpha\rangle$, $|\beta\rangle$) and outgoing ($|\gamma\rangle$, $|\delta\rangle$) coherent states.

complete quantum state of the two input modes. In the simple case shown in Fig. 6.3b, the two input modes are in independent coherent states and the combined input state $|\Psi_{in}\rangle$ is just a product state of them [26, p. 354]:

$$|\Psi_{in}\rangle = |\alpha\rangle\,|\beta\rangle \tag{6.12}$$

The combined output state $|\Psi_{out}\rangle$ is then computed analogous to Eqs. (6.10) and (6.11):

$$|\Psi_{out}\rangle = |\delta\rangle\,|\gamma\rangle = |t_1\beta + r_2\alpha\rangle\,|r_1\beta + t_2\alpha\rangle \tag{6.13}$$

In the case of the beam splitter BS1 shown in Fig. 6.1, the two input states $\hat{\rho}_{vac}$ and $\hat{\rho}_s$ are independent as well. Since both states can be expanded into coherent states with the help of their P-functions $P_s(\alpha)$ and $P_{vac}(\beta)$, the combined input state $\hat{\rho}_{in}$ can then be derived by multiplying their P-function representations [26, p. 355]:

$$\hat{\rho}_{in} = \int\int P_s(\alpha)P_{vac}(\beta)\,|\alpha\rangle\langle\alpha| \otimes |\beta\rangle\langle\beta|\; d^2\beta\, d^2\alpha \tag{6.14}$$

The output state $\hat{\rho}_{out}$ can be found by applying the beam splitter transformation to the coherent states in $\hat{\rho}_{in}$ by $|\Psi_{in}\rangle \to |\Psi_{out}\rangle$:

$$\hat{\rho}_{out} = \int\int P_s(\alpha)P_{vac}(\beta)\,|t_1\beta + r_2\alpha\rangle\langle t_1\beta + r_2\alpha| \otimes |r_1\beta + t_2\alpha\rangle\langle r_1\beta + t_2\alpha|\; d^2\beta\, d^2\alpha \tag{6.15}$$

If $\hat{\rho}_s$ and $\hat{\rho}_{vac}$ describe coherent states, then P_s and P_{vac} are delta functions according to Eq. (6.1) and $\hat{\rho}_{out}$ is exactly the product state from Eq. (6.13). If at least one of the two input states is not a coherent state, the two output modes of the beam splitter are correlated via an integration over α or β. For the following computations, it is easier to represent the output state $\hat{\rho}_{out}$ in terms of the output variables $\gamma = r_1\beta + t_2\alpha$ and $\delta = t_1\beta + r_2\alpha$:

$$\hat{\rho}_{out} = \int\int P_s(t_2^\star\gamma + r_2^\star\delta)P_{vac}(r_1^\star\gamma + t_1^\star\delta)\,|\delta\rangle\langle\delta| \otimes |\gamma\rangle\langle\gamma|\; d^2\gamma\, d^2\delta \tag{6.16}$$

The star symbol * denotes complex conjugation and the substitutions for α and β can be verified by applying Eqs. (6.6) to (6.9):

$$r_1^\star\gamma + t_1^\star\delta = \beta \underbrace{\left(|r_1|^2 + |t_1|^2\right)}_{=1} + \alpha \underbrace{\left(r_1^\star t_2 + t_1^\star r_2\right)}_{=0} = \beta \tag{6.17}$$

$$t_2^\star\gamma + r_2^\star\delta = \beta \underbrace{\left(r_1 t_2^\star + t_1 r_2^\star\right)}_{=0} + \alpha \underbrace{\left(|t_2|^2 + |r_2|^2\right)}_{=1} = \alpha \tag{6.18}$$

The relation $r_1 t_2^\star + t_1 r_2^\star = 0$ is the complex conjugate of relation (6.9).

The calculation of the Wigner function for the target state $\hat{\rho}_t$ can be performed in multiple ways. Here, we make use of the Q–function measurement of $\hat{\rho}_{ps}$ by following three steps:

1. Calculating the joint Q-function $Q(q_t, q_{ps}, p_t, p_{ps})$ for the two output states $\hat{\rho}_t$ and $\hat{\rho}_{ps}$ of the first beam splitter BS1. While q_t and p_t are the quadrature variables detectable by HD3, q_{ps} and p_{ps} are the quadrature variables detectable by the 8-port homodyne detector with HD1 and HD2 measuring a Q-function.

2. Obtaining the conditional Q–function $Q(q_t, p_t)$ in the target arm by selecting on the two quadrature amplitudes q_{ps} and p_{ps} in the postselection arm. This selection procedure can be realized in an experiment by choosing only data points that are inside specific bins for q_{ps} and p_{ps}.

3. Computing the conditional Wigner function $W(q_t, p_t)$ of the target quantum state $\hat{\rho}_t$ by performing a deconvolution of $Q(q_t, p_t)$ with a vacuum state $\hat{\rho}_{vac}$.

6.1.1. Joint Q-function for a Thermal Signal State

So far, this chapter has focused on a model scheme for non-stationary OHT on light fields in mixed states and a general understanding of the lossless beam splitters used in this scheme. The following section uses these considerations to derive the joint Q-function of the combined output state of BS1 in Fig. 6.1 for the case of a thermal signal state $\hat{\rho}_s = \hat{\rho}_{th}$. The starting point of the discussion is the corresponding joint P-function $P(\alpha, \beta) = P_{th}(\alpha)P_{vac}(\beta)$ expressed in terms of the input variables α and β, which is, according to Eq. (6.16), a product of the P-functions of a thermal state and a vacuum state. Following Eq. (6.1), the P-function of a vacuum state is $P_{vac}(\beta) = \delta(\beta)$. The P-function of a thermal state with mean photon number $\bar{n}$ is given, for example, in [26, p. 341] and the joint P-function then reads:

$$P(\alpha, \beta) = \frac{1}{\pi\bar{n}} \exp\left(-\frac{|\alpha|^2}{\bar{n}}\right)\delta(\beta) \tag{6.19}$$

The joint Q-function can be derived from the joint P-function by evaluating the following convolution[4]:

$$Q(\alpha,\beta)=\frac{1}{\pi^3\bar{n}}\int\int\exp\left(-\frac{|\alpha'|^2}{\bar{n}}\right)\delta(\beta')\exp\left(-|\alpha-\alpha'|^2-|\beta-\beta'|^2\right)d^2\beta'\,d^2\alpha' \quad (6.20)$$

Integration over β' results in:

$$Q(\alpha,\beta)=\frac{1}{\pi^3\bar{n}}\int\exp\left(-\frac{|\alpha'|^2}{\bar{n}}\right)\exp\left(-|\alpha-\alpha'|^2-|\beta|^2\right)d^2\alpha' \quad (6.21)$$

One can split the integration over α' into two integrations over its real and imaginary parts by setting $\alpha'=x'+iy'$ and $\alpha=x+iy$:

$$Q(x+iy,\beta)=\frac{\exp\left(-|\beta|^2\right)}{\pi^3\bar{n}}\int\exp\left(-\frac{(x')^2+(y')^2}{\bar{n}}\right)\exp\left(-(x-x')^2-(y-y')^2\right)dx'\,dy' \quad (6.22)$$

Expanding the quadratic terms results in:

$$\begin{aligned}Q(x+iy,\beta)=&\frac{\exp\left(-|\beta|^2-x^2-y^2\right)}{\pi^3\bar{n}}\int\exp\left(-\left(\frac{1}{\bar{n}}+1\right)((x')^2+(y')^2)\right)\\&\times\exp\left(2(xx'+yy')\right)dx'\,dy'\end{aligned} \quad (6.23)$$

By making use of the algebraic relation $1/\bar{n}+1=(1+\bar{n})/\bar{n}$, the final integration can be performed with the help of formula (A.7):

$$Q(x+iy,\beta)=\frac{\exp\left(-|\beta|^2-x^2-y^2\right)}{\pi^3\bar{n}}\frac{\pi\bar{n}}{1+\bar{n}}\exp\left(\frac{\bar{n}}{1+\bar{n}}\left(x^2+y^2\right)\right) \quad (6.24)$$

After replacing $\alpha=x+iy$ and rearranging the exponential functions, the joint Q-function for the input variables α and β is found:

$$Q(\alpha,\beta)=\frac{\exp\left(-|\beta|^2\right)}{\pi^2(1+\bar{n})}\exp\left(-\frac{|\alpha|^2}{1+\bar{n}}\right) \quad (6.25)$$

$Q(\alpha,\beta)$ is a product of the Q-functions of a vacuum state (e.g. [26, p. 326]) and a thermal state (e.g. [26, p. 328]).

Since the conditional target Wigner function will be expressed in terms of the quadratures measurable in the target arm, it is useful to express this joint Q-function in terms of the output variables γ and δ. For the sake of simplicity, a reduced set of real valued

[4] see Eq. (A.6) in Appendix A

transmission and reflection coefficients t and r is used in the remainder of this chapter. Here, the necessary phase shift occurs together with the reflection corresponding to r_2:

$$t_1 = t_2 = t \tag{6.26}$$
$$r_1 = r \tag{6.27}$$
$$r_2 = e^{i\pi} r = -r \tag{6.28}$$

The joint Q-function then reads:

$$Q(\gamma, \delta) = \frac{\exp\left(-|r\gamma + t\delta|^2\right)}{\pi^2(1+\bar{n})} \exp\left(-\frac{|t\gamma - r\delta|^2}{1+\bar{n}}\right) \tag{6.29}$$

6.1.2. Wigner Function from Q-function

This section discusses a method to obtain the Wigner function in the target arm from an already known Q-function in this arm. It is analogous to a discussion in [26, p. 339 ff.] about how to obtain the P-function from the Q-function. The starting point is formula (A.4), which is used to obtain the Q-function from the Wigner function:

$$Q(\alpha = \alpha_r + i\alpha_i) = \frac{2}{\pi} \int\int W(\bar{\alpha}_r, \bar{\alpha}_i) \exp\left(-2\left(\alpha_r - \bar{\alpha}_r\right)^2 - 2\left(\alpha_i - \bar{\alpha}_i\right)^2\right) d\bar{\alpha}_r \, d\bar{\alpha}_i \tag{6.30}$$

Equation (6.30) is now inserted into the Fourier transform of the α-space Q-function from Eq. (A.8):

$$\begin{aligned}\widetilde{Q}(\widetilde{\alpha}_r, \widetilde{\alpha}_i) = \frac{2}{\pi} \int\int\int\int & W(\bar{\alpha}_r, \bar{\alpha}_i) \cdot \exp\left(-2\left(\alpha_r - \bar{\alpha}_r\right)^2 - 2\left(\alpha_i - \bar{\alpha}_i\right)^2\right) \\ & \cdot \exp\left(-i\left(\widetilde{\alpha}_r \alpha_r + \widetilde{\alpha}_i \alpha_i\right)\right) d\bar{\alpha}_r \, d\bar{\alpha}_i \, d\alpha_r \, d\alpha_i\end{aligned} \tag{6.31}$$

Before the integrations take place, two steps are necessary. First, the exponential functions are rearranged:

$$\begin{aligned}\widetilde{Q}(\widetilde{\alpha}_r, \widetilde{\alpha}_i) = & \frac{2}{\pi} \int\int W(\bar{\alpha}_r, \bar{\alpha}_i) \int \exp\left(-2\left(\alpha_r - \bar{\alpha}_r\right)^2 - i\widetilde{\alpha}_r \alpha_r\right) d\alpha_r \\ & \cdot \int \exp\left(-2\left(\alpha_i - \bar{\alpha}_i\right)^2 - i\widetilde{\alpha}_i \alpha_i\right) d\alpha_i \, d\bar{\alpha}_r \, d\bar{\alpha}_i\end{aligned} \tag{6.32}$$

And second, the substitution $\mathring{\alpha}_r = \alpha_r - \bar{\alpha}_r$ is performed:

$$\begin{aligned}\widetilde{Q}(\widetilde{\alpha}_r, \widetilde{\alpha}_i) = & \frac{2}{\pi} \int\int W(\bar{\alpha}_r, \bar{\alpha}_i) \int \exp\left(-2\left(\mathring{\alpha}_r\right)^2 - i\widetilde{\alpha}_r\left(\mathring{\alpha}_r + \bar{\alpha}_r\right)\right) d\mathring{\alpha}_r \\ & \cdot \int \exp\left(-2\left(\mathring{\alpha}_i\right)^2 - i\widetilde{\alpha}_i\left(\mathring{\alpha}_i + \bar{\alpha}_i\right)\right) d\mathring{\alpha}_i \, d\bar{\alpha}_r \, d\bar{\alpha}_i\end{aligned} \tag{6.33}$$

After these two steps, integrating over $\mathring{\alpha}_r$ and $\mathring{\alpha}_i$ with the help of the Gaussian integral from Eq. (A.7) results in:

$$\widetilde{Q}(\widetilde{\alpha}_r, \widetilde{\alpha}_i) = \frac{2}{\pi}\frac{\pi}{2} \exp\left(-\frac{\widetilde{\alpha}_r^2 + \widetilde{\alpha}_i^2}{4 \cdot 2}\right) \underbrace{\int\int W(\bar{\alpha}_r, \bar{\alpha}_i) \exp\left(-i\left(\widetilde{\alpha}_r \bar{\alpha}_r + \widetilde{\alpha}_i \bar{\alpha}_i\right)\right) d\bar{\alpha}_r \, d\bar{\alpha}_i}_{\widetilde{W}(\widetilde{\alpha}_r, \widetilde{\alpha}_i)} \tag{6.34}$$

As the integrals in equation (6.34) resemble the Fourier transform of the Wigner function, one can conclude:

$$\widetilde{W}(\widetilde{\alpha}_r, \widetilde{\alpha}_i) = \widetilde{Q}(\widetilde{\alpha}_r, \widetilde{\alpha}_i) \exp\left(\frac{\widetilde{\alpha}_r^2 + \widetilde{\alpha}_i^2}{8}\right) \tag{6.35}$$

Finally, the complete transformation formula results from applying the reverse Fourier transform (A.9) to equation (6.35):

$$W(\alpha_r, \alpha_i) = \frac{1}{(2\pi)^2} \int\int \widetilde{Q}(\widetilde{\alpha}_r, \widetilde{\alpha}_i) \exp\left(\frac{\widetilde{\alpha}_r^2 + \widetilde{\alpha}_i^2}{8}\right) \exp\left(i\left(\widetilde{\alpha}_r \alpha_r + \widetilde{\alpha}_i \alpha_i\right)\right) d\widetilde{\alpha}_r \, d\widetilde{\alpha}_i \tag{6.36}$$

6.1.3. Conditional Wigner Function from Conditional Q-function

After establishing a method to derive the corresponding Wigner function from a known Q-function, it is now applied to compute the **conditional** Wigner function in the target arm of the setup depicted in Fig. 6.1. "Conditional" means in this context that the joint phase space function for both output ports of the beam splitter is reduced by postselecting and therefore fixing the value of γ in the postselection arm. The analysis starts by replacing $\gamma = \gamma_{ps}$ in the joint Q-function given in Eq. (6.29). The index ps indicates that γ_{ps} is no longer a variable but a fixed parameter and the resulting conditional Q-function $Q(\delta)$ is now only dependent on the variable δ:

$$Q'(\gamma = \gamma_{ps}, \delta) = \frac{\exp\left(-|r\gamma_{ps} + t\delta|^2\right)}{\pi^2(1+\bar{n})} \exp\left(-\frac{|t\gamma_{ps} - r\delta|^2}{1+\bar{n}}\right) \tag{6.37}$$

At the same time, it is necessary to normalize Q' again. It now describes only the target part of the joint quantum state, but it still has to be normalized to 1 to be a valid Q-function. Some computations in this chapter are performed with the help of Mathematica [69] and the required Mathematica commands can be found in appendix A.4. For example, the required normalization factor can be found with the commands in Fig. A.1:

$$Q(\delta) = \frac{1+\bar{n}t^2}{\pi(1+\bar{n})} \exp\left(\frac{|\gamma_{ps}|^2}{1+\bar{n}t^2}\right) \exp\left(-|r\gamma_{ps} + t\delta|^2\right) \exp\left(-\frac{|t\gamma_{ps} - r\delta|^2}{1+\bar{n}}\right) \tag{6.38}$$

In order to compute the Wigner function with the help of equation (6.36), the Fourier transform $\widetilde{Q}(\widetilde{\delta})$ of $Q(\delta)$ is derived first[5] with the help of formula (A.8):

$$\widetilde{Q}\left(\widetilde{\delta}\right) = \exp\left(-\frac{1+\bar{n}}{4(1+\bar{n}t^2)}\left|\widetilde{\delta}\right|^2\right)\exp\left(i\frac{\bar{n}rt}{1+\bar{n}t^2}\left(\widetilde{\delta}_r\gamma_{ps,r}+\widetilde{\delta}_i\gamma_{ps,i}\right)\right) \tag{6.39}$$

Then $\widetilde{Q}\left(\widetilde{\delta}\right)$ is inserted into equation (6.36) to compute the Wigner function[6] $W(\delta)$:

$$W(\delta) = \frac{2\left(1+\bar{n}t^2\right)}{\pi\left(1+\bar{n}+\bar{n}r^2\right)}\exp\left(-\frac{2\left|\left(1+\bar{n}t^2\right)\delta+\bar{n}rt\gamma_{ps}\right|^2}{\left(1+\bar{n}t^2\right)\left(1+\bar{n}+\bar{n}r^2\right)}\right) \tag{6.40}$$

Before the expectation values for the experiments in this chapter can be calculated, the complex variables have to be replaced by the corresponding quadrature variables. Since we chose the commutator convention $[\hat{q},\hat{p}] = i$, it is necessary to substitute $\delta \to (q+ip)/\sqrt{2}$. The same is true for substituting γ_{ps}, but we have to take into account a second factor. The quadrature values q_{ps} and p_{ps} in the postselection arm are measured with respect to the field amplitudes observed by HD1 and HD2 behind BS2, while γ_{ps} corresponds to the field amplitude in front of BS2. Therefore, these quadratures have to be scaled by $1/r_{ps} = \sqrt{2}$ so that they correspond to $\gamma_{ps,r}$ and $\gamma_{ps,i}$. The combined substitution then reads $\gamma_{ps} \to q_{ps} + ip_{ps}$ and we arrive at:

$$\begin{aligned} W(q,p) =& \frac{1+\bar{n}t^2}{\pi\left(1+\bar{n}+\bar{n}r^2\right)}\exp\left(-\frac{\left(\left(1+\bar{n}t^2\right)q+\bar{n}rt\sqrt{2}q_{ps}\right)^2}{\left(1+\bar{n}t^2\right)\left(1+\bar{n}+\bar{n}r^2\right)}\right) \\ &\cdot\exp\left(-\frac{\left(\left(1+\bar{n}t^2\right)p+\bar{n}rt\sqrt{2}p_{ps}\right)^2}{\left(1+\bar{n}t^2\right)\left(1+\bar{n}+\bar{n}r^2\right)}\right) \end{aligned} \tag{6.41}$$

This is the Wigner function measured by the target 4-port HD when selecting the quadratures q_{ps} and p_{ps} in the 8-port HD used for postselection in the case of a thermal signal state with a mean photon number of $\bar{n}$. An example for a conditional Q-function and its corresponding conditional Wigner function is shown in Fig. 6.4. Since the conditional Q-function is a convolution of a vacuum Wigner function with the conditional Wigner function, it is broader than the conditional Wigner function. The offset of the distribution is given by the linear expectation values $\langle q\rangle$ and $\langle p\rangle$ and remains the same.

6.1.4. Expectation Values

Even though the target Wigner function in Eq. (6.41) describes the complete target quantum state, it is useful to calculate the expectation values $\langle q\rangle$, $\langle p\rangle$, $\langle q^2\rangle$ and $\langle p^2\rangle$. These values make it easier to compare the presented theory to measurements, as such expectation values are easily accessible from measurement data. To understand the

[5] for details see Fig. A.2
[6] for details see Fig. A.3

resulting formulas better, the relations $\bar{n}_{ps} = \bar{n}t^2$ and $\bar{n}_t = \bar{n}r^2$ are introduced. Here, $\bar{n}_{ps}$ is the mean photon number in the postselection arm while $\bar{n}_t$ is the mean photon number in the target arm. It is important to note that $\bar{n} = \bar{n}_t + \bar{n}_{ps}$. The results for $\langle q \rangle$ and $\langle p \rangle$ are[7]:

$$\langle q \rangle = \int_{-\infty}^{\infty}\int_{-\infty}^{\infty} W(q,p) q \, dp \, dq = -\sqrt{2} q_{ps} \frac{\bar{n} r t}{1 + \bar{n} t^2} = -q_{ps} \frac{\sqrt{2 \bar{n}_{ps} \bar{n}_t}}{1 + \bar{n}_{ps}} \tag{6.42}$$

$$\langle p \rangle = \int_{-\infty}^{\infty}\int_{-\infty}^{\infty} W(q,p) p \, dp \, dq = -\sqrt{2} p_{ps} \frac{\bar{n} r t}{1 + \bar{n} t^2} = -p_{ps} \frac{\sqrt{2 \bar{n}_{ps} \bar{n}_t}}{1 + \bar{n}_{ps}} \tag{6.43}$$

The minus sign arises from our specific choice of reflection and transmission coefficients in Eqs. (6.26)-(6.28), which determines the allocation of the phase shift occurring in the beam splitter. For example, when choosing $r_1 = -r$ and $r_2 = r$ instead, the minus sign vanishes. Next, the expectation values of the quadratic quadrature amplitudes are calculated[8]:

$$\left\langle q^2 \right\rangle = \int_{-\infty}^{\infty}\int_{-\infty}^{\infty} W(q,p) q^2 \, dp \, dq = \frac{1 + \bar{n} + \bar{n} r^2 + \bar{n} t^2 \left(1 + \bar{n} + \bar{n} r^2 \left(1 + 4 q_{ps}^2\right)\right)}{2 \left(1 + \bar{n} t^2\right)^2} \tag{6.44}$$

$$\left\langle p^2 \right\rangle = \int_{-\infty}^{\infty}\int_{-\infty}^{\infty} W(q,p) p^2 \, dp \, dq = \frac{1 + \bar{n} + \bar{n} r^2 + \bar{n} t^2 \left(1 + \bar{n} + \bar{n} r^2 \left(1 + 4 p_{ps}^2\right)\right)}{2 \left(1 + \bar{n} t^2\right)^2} \tag{6.45}$$

Finally, the variances corresponding to q and p can be calculated[9]:

$$Var(q) = Var(p) = \left\langle q^2 \right\rangle - \langle q \rangle^2 = \frac{1 + \bar{n} + \bar{n}_t}{2(1 + \bar{n}_{ps})} \tag{6.46}$$

Interestingly, the variance of the target Wigner function strongly depends on the photon numbers in the target and postselection arms. The lowest achievable variance is 1/2, which can be found for $\bar{n} = 0$ or in the limiting case for $\bar{n}_t \to 0$. It is the variance expected for the vacuum state and a coherent state. The highest possible variance is achieved in the limit for $\bar{n}_{ps} \to 0$ and is $1/2 + \bar{n}$. This is the expected variance for a thermal state measured by a single 4-port HD. Between these two extremal values, the variance can be tuned by controlling the ratio between $\bar{n}_t$ and $\bar{n}_{ps}$. For $\bar{n}_t = 1/2 \bar{n}_{ps}$ and sufficiently high $\bar{n}$, for instance, the variance is close to 1. This case becomes relevant when all three 4-port HDs depicted in Fig. 6.1 receive the same mean photon number, which is a reasonable setting in an experiment to illuminate all 3 HDs equally well. Figure 6.4 compares the conditional Wigner function in such a case with its corresponding conditional Q-function and a true coherent state. There are significant differences in the widths of these distributions, while their expectation values follow Eqs. (6.42) and (6.43).

[7] for details see Fig. A.4
[8] for details see Fig. A.5
[9] for details see Fig. A.6

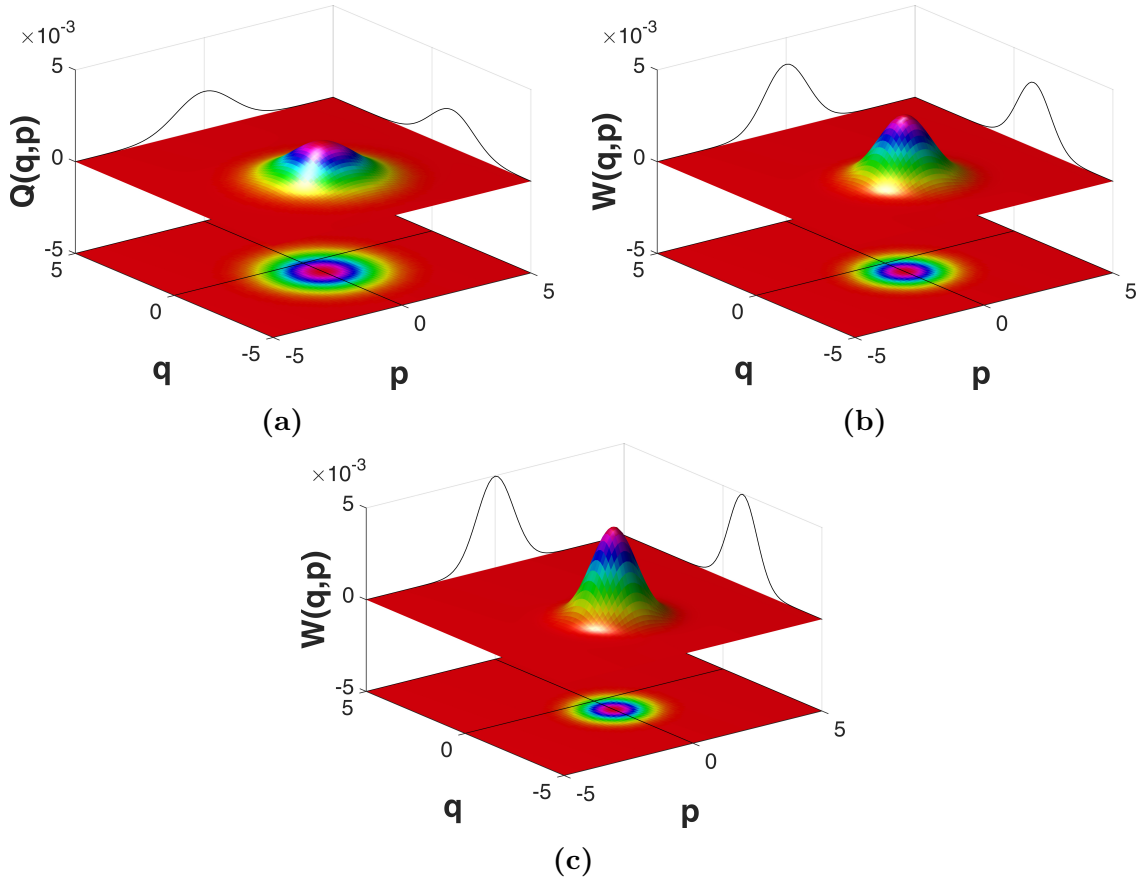

Figure 6.4.: (a) Conditional Q-function according to Eq. (6.37) and (b) conditional Wigner function according to Eq. (6.41) postselected from a thermal state with $\bar{n} = 1$ photons at amplitudes $q_{ps} = 2.5$ and $p_{ps} = 0$. The reflection coefficient of beam splitter BS1 amounted to $|r| = 1/\sqrt{3}$. For comparison, a coherent state Wigner function (c) is shown. All three phase space functions are displaced from the origin by $\langle q \rangle = -1$, which may be calculated using Eq. (6.42).

6.1.5. Conclusion

Section 6.1 introduced a 12-port homodyne detection scheme for non-stationary OHT that aims at reconstructing the Wigner function of light fields in mixed quantum states. The phase information is retrieved by employing two 4-port HDs in such a way that they are able to measure the Q-function of a part of the input quantum state. When the Q-function measurements are used to postselect on specific quadrature values q_{ps} and p_{ps}, this essentially fixes not only the phase but also the amplitude of the Wigner function measurement in the remaining 4-port HD **a posteriori**. The resulting target Wigner function for a thermal signal quantum state is a Gaussian distribution displaced from the origin. Its variance is always larger than the minimum variance given by the uncertainty relation in Eq. (2.15), because precision is lost due to the copying of the signal quantum state on beam splitters.

6.2. Stationary 12-Port Tomography on a Thermal State

This section first presents an experimental setup that allows one to test the theoretical limits derived in section 6.1 experimentally and then provide empirical evidence for this setup to operate close to these limits. Such a setup needs to overcome several challenges in order to approximate the scheme outlined in Fig. 6.1. Major challenges include maintaining the fixed phase relationship between HD2 and HD3 in Fig. 6.1, which is necessary for the Q-function measurement, and the reconstruction of a phase reference required for the reconstruction of the conditional Wigner function in the target arm. A 12-port HD based on the technology of the 4-port HD presented in chapter 4 addresses these issues.

6.2.1. Building a 100 MHz 12-Port Homodyne Detector

Building a 12-port homodyne detector is very similar to building a 4-port homodyne detector. The optical setup of the 12-port HD used in this work is illustrated in Fig. 6.6. It comprises three 4-port HDs of the type shown in Fig. 4.2. Here, the LO from the *Mira 900* is divided onto the three HDs by a combination of two beam splitters and two half-wave plates. The signal light from either the *DL pro* diode laser or the LO itself is divided into the three signal beams by a similar combination of two beam splitters and two half-wave plates.

For the experiments in this section, it is very important that the LO pulses in all three HDs sample the same part of the signal light field. Otherwise, the postselection step discussed in section 6.1 would not be possible because different HDs would measure independent parts of the signal light field. This requirement can be fulfilled by aligning all three HDs with the LO as signal at the same time. The spectral width of the signal light from the diode laser is also reduced by an optical bandpass filter for the LO to overlap with it completely. The geometry in the setup presented in Fig. 6.6 can be used to make the necessary adjustments by tuning the delay line positions and moving the

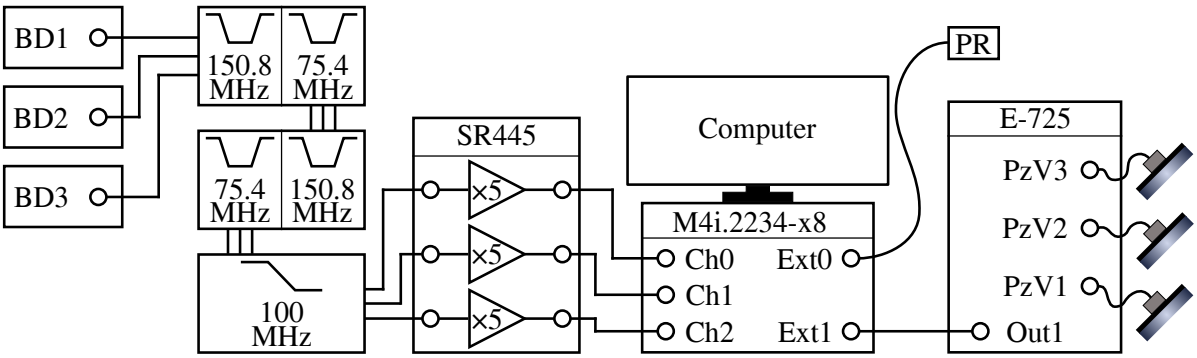

Figure 6.5.: The wiring of the electrical components of the 12-port homodyne detection setup used for the results in this chapter. See text for details.

90:10 beam splitter closer to the *DL pro* while maintaining the positions of the other beam splitters.

The wiring of the electrical components in the 12-port HD is illustrated in Fig. 6.5. While the piezo controller *E-725*, the voltage amplifier *SR445* and the data acquisition card *M4i.2234-x8* can handle two additional HDs without requiring new hardware, two additional sets of electrical filters are needed for the balanced detectors *BD2* and *BD3*. They are identical to the filters introduced in section 4.1, which are two 75.4 MHz and two 150.8 MHz band pass filters and one 100 MHz low pass filter for each HD.

Since the 12-port HD consists of three 4-port HDs, its alignment procedure is almost identical to aligning three single 4-port HDs. They can be aligned, for instance, with the help of the methods outlined in section 4.1.1. After aligning each detector with the LO as signal, the diode laser beam path can be aligned to the LO beam path of one detector and is automatically aligned to the LO beam paths of the other detectors, too. Figure 6.6 contains three different positions for CCD cameras, but only one camera is needed because it can be placed at the required positions during the alignment procedure. The alignment of the balanced detectors is identical to the alignment procedure presented in section 4.1.2.

A slightly modified version of the *complex trigger* scheme is used for the measurements presented in this chapter. The piezo actuators in front of BD1, BD2 and BD3 were modulated with 0 Hz, 50 Hz, and 0.5 Hz sinusoidal voltages, respectively. The TTL output of the piezo controller was set to gate the *simple trigger* when the position of the piezo actuator in front of BD2 is between an upper and lower threshold. In order to achieve a linear phase modulation within the acquired data sets, the thresholds were chosen to contain only the approximately linear parts of the sine function. The raw data was acquired with a sampling rate of 1.25 GHz per balanced detector simultaneously. For each detection channel, the acquired quadrature values $\{Q_{1,i}, Q_{2,i}, Q_{3,i}\}$ can then be calculated according to section 4.1.3.

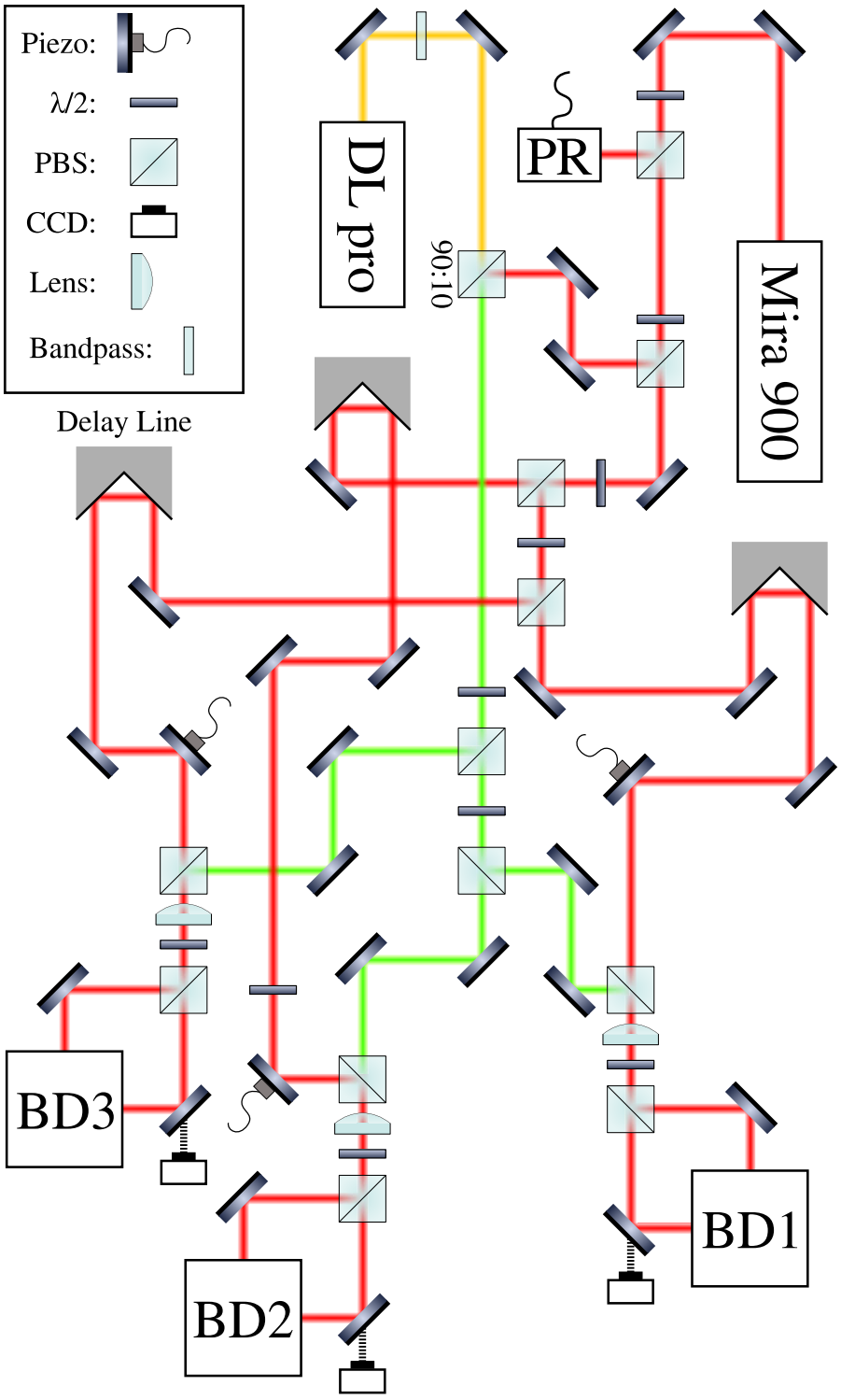

Figure 6.6.: A scheme of the 12-port homodyne detection setup used for the measurements presented in this chapter. BD1, BD2 and BD3 are balanced detectors, PR is a photoreceiver, and the only non-polarizing beam splitter has a splitting ratio of 90:10. See text for further details.

6.2.2. Phase-Sensitive Measurements on a Thermal State

In the following, BD1 is chosen to be part of the HD in the target arm, while BD2 and BD3 are placed in the postselection arm. So far, the quadratures $\{Q_{2,i}\}$ and $\{Q_{3,i}\}$ acquired in the postselection arm do not correspond to Q-function measurements, because they were not acquired with orthogonal LO phases. However, due to the modulation of the piezo actuator in front of BD2, they contain a subset of quadrature measurements where the LOs are orthogonal. In order to select only this subset, the phases $\{\phi_{2,3,i}\}$ between the LOs in channels 2 and 3 must be calculated. This can be achieved by applying the phase reconstruction algorithm from section 4.2.2 to the product quadratures $Q_{\mathrm{prod},i} = Q_{2,i} \cdot Q_{3,i}$. An argument for the validity of this approach is given next.

We know from section 3.1 that the values acquired with a HD are proportional to the signal field that is in phase with the LO:

$$Q_i \propto \mathcal{E}^q_{\mathrm{SIG}} \cos(\theta_{\mathrm{LO}}) + \mathcal{E}^p_{\mathrm{SIG}} \sin(\theta_{\mathrm{LO}}) \tag{6.47}$$

Such a linear combination of sine functions can be replaced by a general sine function with different amplitude and an additional phase offset θ_{off} [70, p. 84]. Accordingly, the quadrature amplitudes $Q_{2,i}$ and $Q_{3,i}$ can be rewritten in terms of the modified LO phase $\phi_{\mathrm{LO2}} = \theta_{\mathrm{LO2}} + \theta_{\mathrm{off}}$ in channel 2 and the relative phase $\phi_{2,3}$ between channels 2 and 3:

$$Q_{2,i} \propto \sin(\phi_{\mathrm{LO2},i}) \tag{6.48}$$

$$Q_{3,i} \propto \sin(\phi_{\mathrm{LO2},i} + \phi_{2,3,i}) \tag{6.49}$$

Equation (6.49) can be expanded with the help of an addition theorem for trigonometric functions [70, p. 81] in order to obtain an expression for the product quadratures $Q_{\mathrm{prod},i}$:

$$Q_{\mathrm{prod},i} \propto \sin^2(\phi_{\mathrm{LO2},i}) \cos(\phi_{2,3,i}) + \sin(\phi_{\mathrm{LO2},i}) \cos(\phi_{\mathrm{LO2},i}) \sin(\phi_{2,3,i}) \tag{6.50}$$

For a thermal signal state, the LO phase $\phi_{\mathrm{LO2},i}$ is random for each acquired quadrature value while the relative phase $\phi_{2,3,i}$ is mainly determined by the slow modulation of the piezo in front of BD2. Hence, the smoothing performed by the phase reconstruction algorithm before estimating the phase values averages over the sine functions that depend on $\phi_{\mathrm{LO2},i}$ but leaves the slow modulation of $\phi_{2,3,i}$ intact:

$$\langle Q_{\mathrm{prod},i} \rangle \propto \cos(\phi_{2,3,i}) \tag{6.51}$$

Thus, due to the linear phase modulation over time, it is valid to assume that $Q_{\mathrm{prod},i}$ follows a sinusoidal function, and the phase reconstruction algorithm yields the relative phase values $\phi_{2,3,i}$. Relative phase values $\phi_{1,2,i}$ between the LOs in channels 1 and 2 can be calculated in the same way.

In order to obtain a Q-function measurement, the phase values $\phi_{2,3,i}$ can be used to select quadrature amplitudes $Q^{\mathrm{ort}}_{2,i}$ and $Q^{\mathrm{ort}}_{3,i}$ in channels 2 and 3 that were acquired with orthogonal LO phases. Additionally selecting the phases $\phi_{1,2,i}$ and the channel 1 quadratures $Q_{1,i}$ corresponding to these orthogonal LO phases results in a data set $\{Q^{\mathrm{ort}}_{1,i}, Q^{\mathrm{ort}}_{2,i}, Q^{\mathrm{ort}}_{3,i}, \phi^{\mathrm{ort}}_{1,2,i}\}$ that allows us to perform the postselection step outlined in section

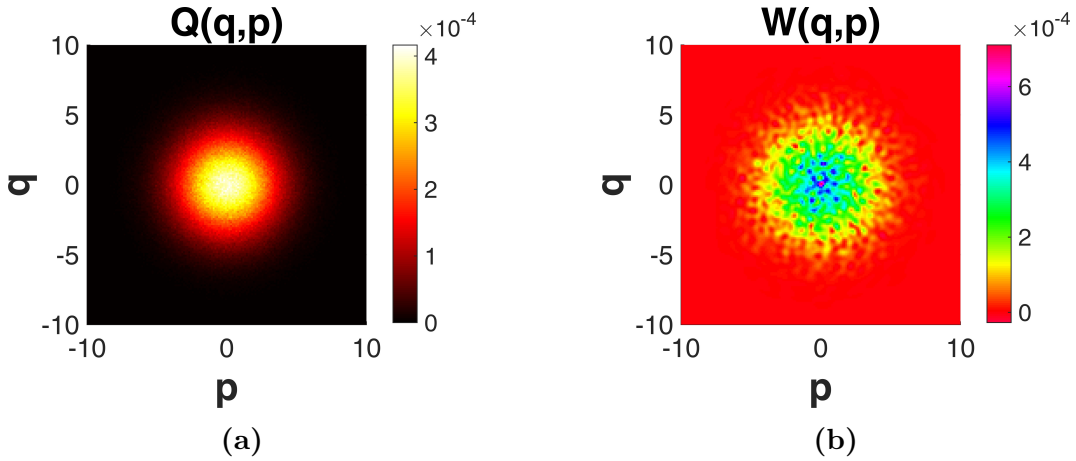

Figure 6.7.: The orthogonal selection of the quadrature values acquired with channels 2 and 3 of the 12-port homodyne detector for a thermal signal state results in a Q-function measurement (a). A thermal Wigner function (b) can be reconstructed from the quadratures recorded in channel 1 at the same times. On average, there were 5.63, 5.94, and 5.92 signal photons per LO pulse in channels 1, 2, and 3, respectively.

6.1.3. Figure 6.7 compares the Wigner function reconstructed from the quadratures $\{Q_{1,i}^{\mathrm{ort}}\}$ with the Q-function retrieved as a histogram of pairs $(Q_{2,i}^{\mathrm{ort}}, Q_{3,i}^{\mathrm{ort}})$. This data set consisted of 63 685 374 quadrature measurements per channel before the orthogonal selection and 2 288 302 thereafter. Both functions show no phase dependence, which is expected for a thermal state measurement. While the Q-function looks smooth, the reconstructed Wigner function has little spikes on top of its broad Gaussian shape. These spikes are caused by the maximum likelihood algorithm, which was operated with random phase values for the reconstruction. In general, it works much better when supplying properly reconstructed phase values.

Postselecting the quadratures $q_{t,i} \coloneqq Q_{1,i}^{\mathrm{ort}}$ in the target arm on specific sets of quadratures $q_{ps,i} \coloneqq Q_{2,i}^{\mathrm{ort}}$ and $p_{ps,i} \coloneqq Q_{3,i}^{\mathrm{ort}}$ in the postselection arm provides us with control over amplitude and phase of the reconstructed quantum state. Figure 6.8 presents two examples of conditional Wigner functions reconstructed for a range of postselected quadrature amplitudes

$$A_{ps} = \sqrt{q_{ps}^2 + p_{ps}^2} \tag{6.52}$$

and a range of postselected phases

$$\phi_{ps} = \arctan\left(\frac{q_{ps}}{p_{ps}}\right). \tag{6.53}$$

The amplitude selected conditional Wigner function has the shape of a ring, similar to the phase-averaged coherent state illustrated in Fig. 4.7. It is approximately rotationally symmetric and therefore phase independent. The radius of this ring, which corresponds to the quadrature amplitude A_t of the underlying conditional quantum state, is related

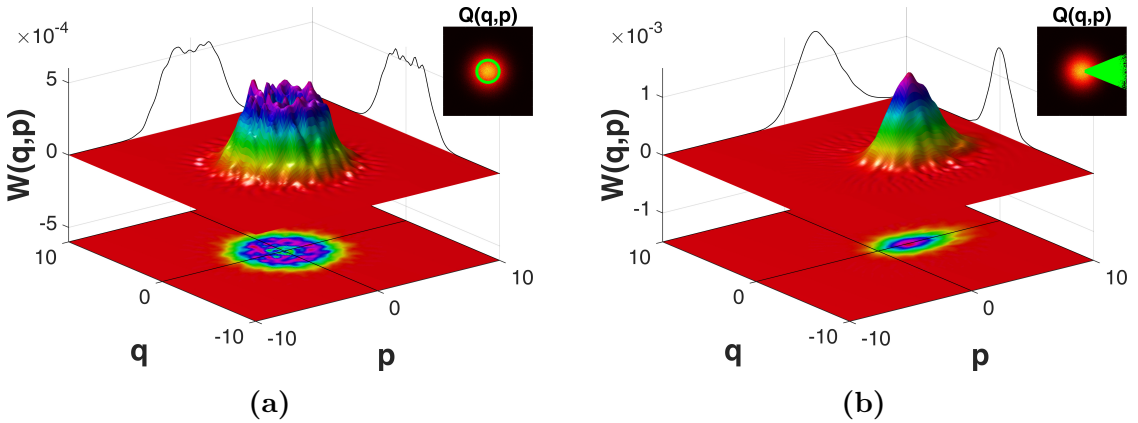

Figure 6.8.: Conditional Wigner functions in the target channel when selecting on (a) an amplitude range $A_{ps} = 2.5 \pm 0.25$ or (b) a range of phases $\phi_{ps} = 0 \pm \pi/8$ of the Q-function in the postselection arm. The insets show the selected Q-function data points in green color on top of the Q-function histogram. It is the same data set as in Fig. 6.7a.

to the postselected quadrature amplitude A_{ps}. Their relationship can be calculated from Eqs. (6.42) and (6.43):

$$A_t = \sqrt{\langle q \rangle^2 + \langle p \rangle^2} = \pm\sqrt{2} A_{ps} \frac{\sqrt{\bar{n}_{ps}\bar{n}_t}}{1 + \bar{n}_{ps}} \tag{6.54}$$

We find good agreement between the value of $A_t = 2.2465$ expected for $A_{ps} = 2.5$ and the value of $A_t = 2.2472$ retrieved from the reconstructed Wigner function. In contrast to the amplitude selected Wigner function, we find a strong phase dependence with the phase-selected conditional Wigner function in Fig. 6.8b. At the same time, its amplitude is not as well defined.

Combined control of amplitude and phase was applied to reconstruct the conditional Wigner function in Fig. 6.9a. The postselected quadratures q_t are equivalent to Fig. 6.8a. This time, however, the reconstruction algorithm received additional information in form of phases θ_t that are a combination of ϕ_{ps} and $\phi_{1,2}$. Similar to a coherent Wigner function, for example shown in Fig. 4.12, this conditional Wigner function is a Gaussian distribution displaced from the origin. The displacement amounts to $\langle p \rangle = 2.218$ and is close to the expected value of 2.2465. Taking the phases θ_t into account recovers the phase information lost with the amplitude selection and is therefore equivalent to selecting a small area around (q_{ps}, p_{ps}) of the Q-function. Consequently, equation (6.46) is expected to describe the variance of such a conditional Wigner function. The variances along the q- and p-directions of the Wigner function in Fig. 6.9a are $Var(p) = 1.123$ and $Var(q) = 1.105$. Both values are slightly higher than the expected minimum variance of $Var(q) = Var(p) = 0.938$ but are significantly lower than the variance of $Var(Q_1) = 6.133$ calculated from the quadratures recorded in the target channel. Imperfections in the experimental setup, such as differences in signal and LO overlap among the detection channels, as well as phase errors induced by the phase reconstruction algorithm, are possible explanations for the mismatch between $Var(q)$ and $Var(p)$ and for the

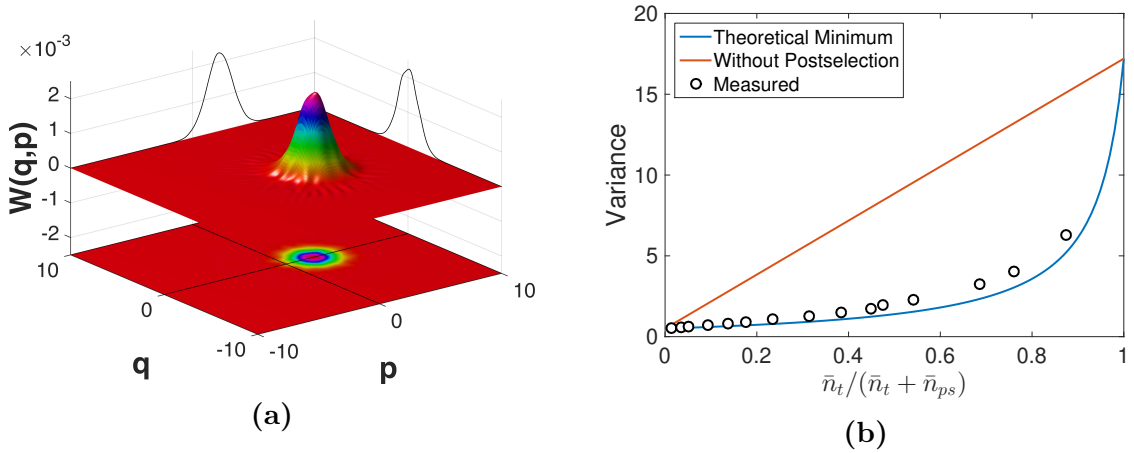

Figure 6.9.: Selecting on a range of quadrature amplitudes of $A_{ps} = 2.5 \pm 0.25$ and taking into account the phase values $\phi_{1,2}$ and ϕ_{ps} results in a narrow and phase-dependent reconstructed Wigner function (a). Figure (b) compares its average variance $\langle Var(q_{t,\theta})\rangle_\theta$ for different photon numbers $\bar{n}_t$ and $\bar{n}_{ps}$ in the target and postselection arms with the values expected from Eq. (6.46) (blue) and the variance $Var(Q_1)$ of the quadratures recorded in the target channel without postselection (red).

remaining gap between theory and experiment. Figure 6.9b compares the measured and expected variances for several configurations of photon numbers in the target and postselection arm. In order to achieve a more accurate picture of the Wigner function's width, the postselected data points (q_t, θ_t) were divided into 100 phase bins, which correspond to integral projections of the Wigner function for different phases θ_t, to compute the variance $Var(q_{t,\theta})$ of each bin separately. The average variance $\langle Var(q_{t,\theta})\rangle_\theta$ over all bins is shown in Fig. 6.9b. The measured variances follow the behavior of the expected minimum variance nicely while always being slightly larger.

The results presented in this section and the technical details of the postselection procedure may be interpreted more intuitively. On a microscopic basis, a thermal light field may be considered coherent at any given instant with a well defined amplitude and phase. Due to the random emission processes in thermal light sources, however, amplitude and phase change their values on a timescale corresponding to the coherence time of the light, which is typically in the femtosecond regime. Since these changes must happen continuously, the coherent state at some instant t_0 moves in phase space over time t [19, p. 52]. When using a 4-port HD, it is not possible to differentiate between fluctuations resulting from these movements and quantum noise from the microscopic coherent state. Tomographic reconstruction of a thermal quantum state therefore results in an averaged state, which is much broader than a coherent state and maximally uncertain in phase, because the amplitudes of the microscopic states follow an exponential distribution and their phases are equally probable. Figure 6.10 illustrates this averaging in the Wigner function representation. While the average over only 10 microscopic coherent Wigner functions in Fig. 6.10a features few similarities with the comparable thermal Wigner function in Fig. 6.10d, the average over 10 000 coherent Wigner functions in Fig. 6.10c is

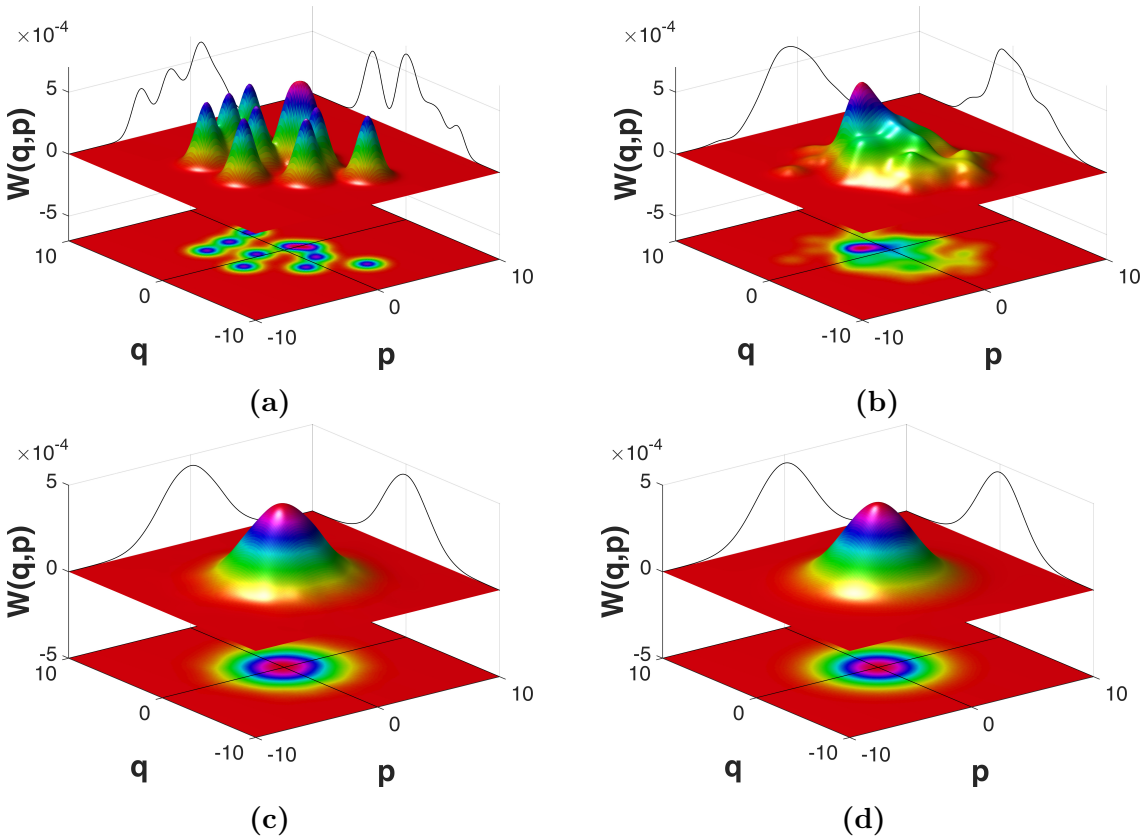

Figure 6.10.: Comparing the Wigner function of a thermal state with $n = 5$ photons (d) to the averaged Wigner function of 10 (a), 100 (b), and 10000 (c) coherent states with uniformly distributed phases and exponentially distributed photon numbers. The expectation value of the exponential distribution also amounted to $n = 5$.

almost identical to it. Our postselection protocol can be interpreted to reverse the averaging. While the Q-function's amplitude selection excludes microscopic coherent states outside the selected range, the reconstruction of phases rotates all microscopic states in phase space in order to overlap at the same angle. Since each acquired data point may belong to every microscopic state with a finite probability at the reconstructed point in phase space, the resulting Wigner function must be broader than a coherent one.

6.3. Time-Dependent 12-Port Tomography on a Thermal State

We now investigate the temporal evolution of conditional thermal quantum states. In terms of the moving coherent state interpretation, such an analysis yields insights about the motion of the microscopic coherent state in phase space. For the results in the previous section, all three LOs sampled the same part of the signal light field. In order to access the temporal evolution, we performed measurements where the LO in the target arm was delayed by a time τ. Thus, it sampled a different temporal part of the signal light field than the LOs in the postselection arm. Experimentally, the delay was realized by driving the delay line in the beam path of LO1 in the setup shown in Fig. 6.6, which allows one to achieve positive and negative delays. Figure 6.11 shows the time dependence of four key parameters of the conditional target quantum state for several postselected quadrature amplitudes A_{ps}. All measurements in this section were performed using a splitting ratio given by $2\bar{n}_t \approx \bar{n}_{ps} \approx 12$.

The target quadrature amplitude $A_t(\tau)$ has a remarkable shape with a main peak around $\tau = 0$ and two side maxima at about $\pm 1000\,\mathrm{fs}$. In order to explain this shape, we need to take into account the spectral density of the signal light field shown in Fig. 6.12a. According to the Wiener-Khintchine theorem [71, p. 59], the autocorrelation function $\Gamma(\tau)$ of a stationary random process, such as the emission of thermal light, is connected to its spectral density $S(\omega)$ via a Fourier transform:

$$\Gamma(\tau) = \int_{-\infty}^{\infty} S(\omega) e^{-i\omega\tau} d\omega. \tag{6.55}$$

Since the target amplitude decays like the autocorrelation function, the time dependence of $A_t(\tau)$ is proportional to $|\Gamma(\tau)|$. The solid lines in Fig. 6.11 provide the numerical Fourier transform of the spectral density shown in Fig. 6.12a, which is scaled for $A_t(0)$ to match the value expected from Eq. (6.54). The experimentally determined quadrature amplitudes are in good agreement with the expected behavior; they rise proportionally with A_{ps} and even reproduce the asymmetric shape of the side maxima with a steeper slope close to the main peak. In order to better understand the origin of the side maxima, we perform the Fourier transform for a general rectangular spectral density function

$$S(\omega) = \begin{cases} 1, & \text{if } \omega_1 \leq \omega \leq \omega_2. \\ 0, & \text{if } \omega < \omega_1 \text{ or } \omega > \omega_2. \end{cases} \tag{6.56}$$

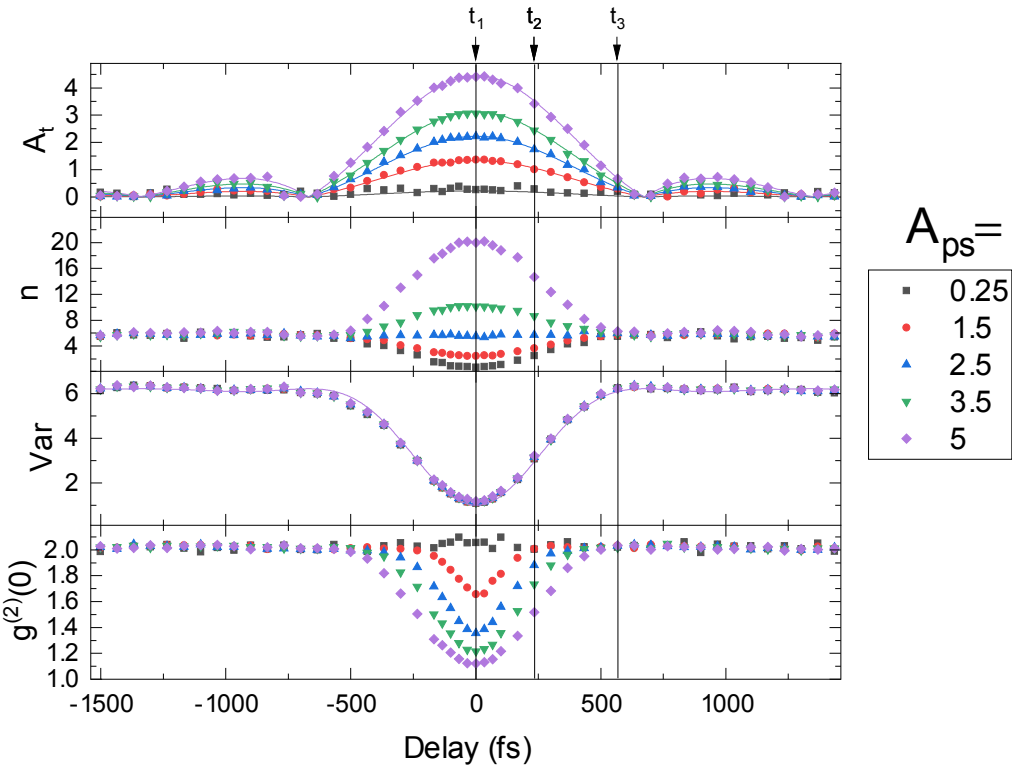

Figure 6.11.: Dependence of the target quadrature amplitude A_t, the photon number n, the average variance Var, and the equal-time second-order correlation function $g^{(2)}(0)$ on the delay between the LO in the target arm and the LOs in the postselection arm of a 12-port homodyne detector measuring a thermal quantum state. The expected dependencies are given as solid lines. The target Wigner functions corresponding to times t_1, t_2, and t_3 are shown in Fig. 6.12.

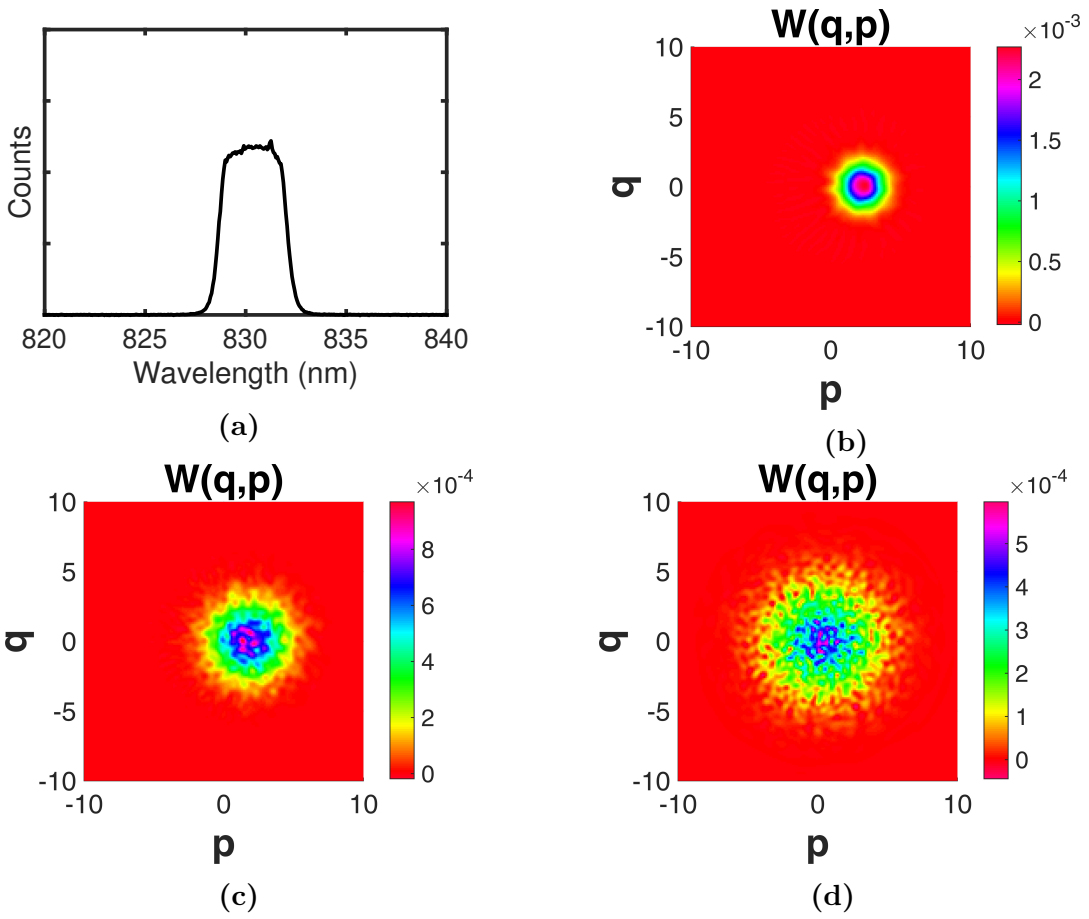

Figure 6.12.: Spectral density function of the filtered thermal signal light field (a) together with the conditional target Wigner functions for times t_1, t_2 and t_3 in Fig. 6.11.

When setting the frequencies ω_1 and ω_2 appropriately, $S(\omega)$ approximates the spectrum in Fig. 6.12a. Next, we evaluate Eq. (6.55) by introducing the difference frequency $\Delta\omega = \omega_2 - \omega_1$ and calculate the absolute value of $|\Gamma(\tau)|$:

$$\begin{aligned}\Gamma(\tau) = \int_{\omega_1}^{\omega_2} e^{-i\omega\tau} d\omega &= \frac{1}{-i\tau}\left(e^{-i(\omega_1+\Delta\omega)\tau} - e^{-i\omega_1\tau}\right) \\ &= \frac{e^{-i\omega_1\tau}}{-i\tau}\left(e^{-i\Delta\omega\tau} - 1\right) \\ &= 2e^{-i(\omega_1+\Delta\omega/2)\tau}\frac{\sin(\tau\Delta\omega/2)}{\tau} \qquad (6.57)\end{aligned}$$

$$\Rightarrow \qquad |\Gamma(\tau)| = \left|\frac{\sin(\tau\Delta\omega/2)}{\tau/2}\right| \qquad (6.58)$$

For $\Delta\omega = 1$, the result is the absolute value of the cardinal sine function; in general, $\Delta\omega$ determines the periodicity of the side maxima. The denominator τ reduces the amplitude of the sine modulation, which results in the asymmetry of the side maxima.

Equation (6.46) predicts the variance's independence of A_{ps}, which we also find in the

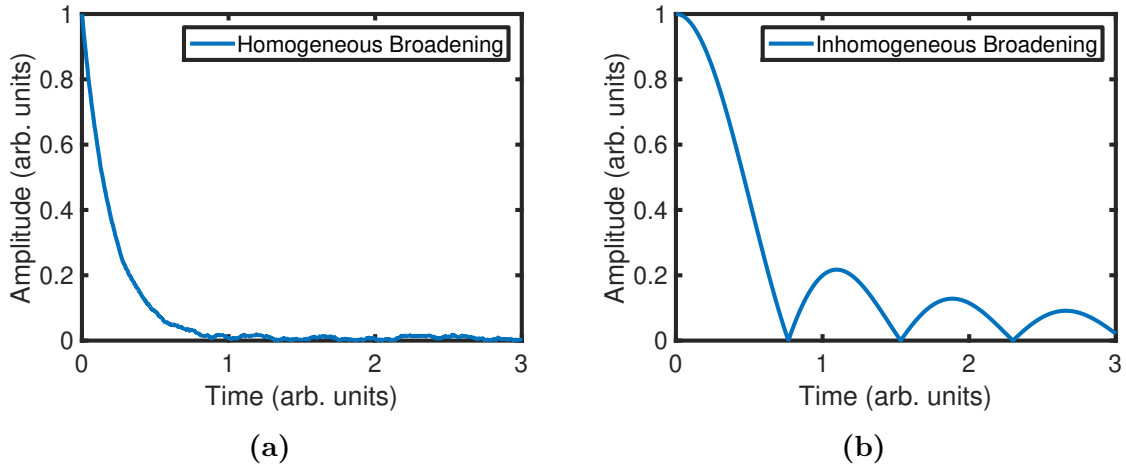

Figure 6.13.: Classical numerical simulation of the amplitude decay in an ensemble of 10 000 emitters subject to (a) homogeneous broadening and (b) inhomogeneous broadening with a rectangular spectral density.

data shown in Fig. 6.11. Since the decay of the quadrature variance is expected to scale as the square of the quadratures, it can be modeled by $-s\,|\Gamma(\tau)|^2 + \bar{n}_t + 1/2$ in form of the presented solid line. The factor s matches $Var(\tau = 0)$ with the value predicted by Eq. (6.46). Theory and experiment are in good agreement.

The variance of a Wigner function as well as its amplitude contribute to its photon number n. In the case of a coherent state, the variance contribution is zero, because it is a minimum uncertainty state. For a thermal state, however, the amplitude contribution is zero and n is determined by the variance only. In figure 6.11, $n(\tau)$ is dominated by the variance for larger values of τ and by the amplitude for small τ. This results in a steady state of about $n = 6$ for delays larger than $\tau = \pm 500\,\mathrm{fs}$ for all postselected quadrature amplitudes A_{ps} due to the quadrature variance. Within the $\tau = \pm 500\,\mathrm{fs}$ range, $n(\tau)$ dips below the steady state for $A_{ps} \lesssim 2.5$ and above it for $A_{ps} \gtrsim 2.5$. This indicates that the target state at zero delay has more similarities to a coherent state than a thermal state. In general, the hallmark indicator to distinguish coherent light from thermal light is the equal-time second-order correlation function $g^{(2)}(0)$, also shown in Fig. 6.12. For large delays or low values of A_{ps}, we find the steady state of a thermal state with $g^{(2)}(0) = 2$; for small delays or large values of A_{ps}, however, the conditional quantum state exhibits reduced photon number noise much closer to the value of 1 expected for a coherent state.

Figures 6.12(b)-(c) provide the reconstructed conditional target Wigner functions for times $t_1 = 0\,\mathrm{fs}$, $t_2 = 233.5\,\mathrm{fs}$, and $t_3 = 567.1\,\mathrm{fs}$. While they illustrate the discussed decay in amplitude and variance, they can be viewed in terms of the moving coherent state interpretation: figure 6.12(b) represents an almost coherent state $\hat{\rho}_i$ found at some instant t, whereas figures 6.12(c) and (d) represent averages of states $\hat{\rho}_i$ propagating for times t_2 and t_3. The center of the distribution shifts towards the origin, because lower amplitudes are more likely than higher amplitudes. At the same time, the variance grows, because the average propagation distance increases for larger times.

Analyzing the observed time dependencies from a microscopic point of view with re-

spect to the light source, the class of possible drivers for the coherent state's movement can be narrowed down, which is discussed qualitatively in the final part of this section. In general, there are two classes of **broadening mechanisms** for spectral lines: **homogeneous** and **inhomogeneous** [21, p. 56]. They affect the shape of spectral lines because they describe two kinds of influences on the emitters generating the light field. In the case of homogeneous broadening, all emitters show the same behavior and generate light with the same spectral shape, while in the case of inhomogeneous broadening, the emitters show different behaviors and generate light with different spectral shapes [21, p. 56]. In both cases, all emitters contribute to the final light field. An example of homogeneous broadening is collisional broadening, in which an emitter is interrupted by some collision, which may induce a random phase shift in its emission. In a very simple numerical model, the electric field from each emitter might be represented classically by Eq. (2.2) and is subject to a random phase shift with a small probability in each time step. The amplitude of the combined electric field then follows an exponential decay as shown in Fig. 6.13a. Inhomogeneous broadening, however, results from different energies and therefore different frequencies of the emitters. Even without further external influences, this results in a decreasing combined electric field amplitude due to dephasing, as shown in Fig. 6.13b. Its decay for times close to zero is approximately Gaussian and therefore less steep than in the case of an exponential decay for homogeneous broadening. The observed decay in amplitude in Fig. 6.11 closely resembles the temporal dependence expected for dephasing due to inhomogeneous broadening with its Gaussian-like decay. Emitters in the diode laser used for our experiments are probably subject to both, homogeneous and inhomogeneous broadening, while inhomogeneous broadening dominates for the chosen spectral width of the signal light field.

7. Conclusion

The primary result of this work is the introduction of a new kind of technique for optical quantum state tomography, which is called non-stationary optical homodyne tomography. It is an expansion of the established technique of stationary OHT, which is performed with a 4-port homodyne detector. An important milestone in the experiments leading up to the new technique was the development of a reliable state-of-the-art 4-port OHT setup. It follows the design of Kumar et al. [43], providing a bandwidth of 100 MHz, but is built upon a commercially available detector instead of a self-made one. While the quadrature sample rate of 75.4 MHz, which is determined by the repetition rate of the LO, made real-time studies of $g^{(2)}(0)$ with a femtosecond temporal resolution possible, there are already further technological advancements in sight with reported homodyne detector bandwidths of 300 MHz [72] and pulsed lasers with multi-gigahertz repetition rates [73, 74, 75].

Stationary OHT allows one to tomographically reconstruct the Wigner quasiprobability function describing the quantum state of a light field. While the complete reconstruction requires the LO to be phase-locked to the signal light field, some useful information, such as the state's photon number distribution, can be obtained without this a priori constraint [76]. Non-stationary OHT, on the other hand, is based on the idea of measuring the phase between LO and signal instead. This work shows that such a measurement comes at the cost of additional noise mixed into the reconstructed quantum state, which is founded in the no-cloning theorem [62]. Furthermore, it was possible to operate the non-stationary OHT setup close to this fundamental limit and it is shown that the added noise is almost independent of the average number of photons in the signal field. Due to this, its negative impact on the reconstructed quantum state is limited. The enhanced possibilities of non-stationary OHT compared to stationary OHT became most apparent on the example of thermal light from a diode laser operated below threshold. For such a mixed quantum state, stationary OHT provides only the average over all Wigner functions of all states the light field may adopt at any given instant. With non-stationary OHT, it is possible to select on these instantaneous states individually and to monitor their evolution in time. The performed measurements supported the interpretation of thermal light as a single coherent state moving in phase space over time [19, p. 52], and dephasing dominated the time evolution due to inhomogeneous broadening.

Most real quantum systems are in mixed states due to an unknown coupling to their environment. Thus, non-stationary OHT is a tool for complete quantum tomography on a large range of previously inaccessible quantum systems. Even light from a laser source is not perfectly coherent, which renders stationary OHT problematic as soon as LO and signal are not derived from the same light source. One example of a photonic quantum technology may benefit from non-stationary OHT is quantum optical memory.

In general, it stores a quantum state in order to perform a particular task on it [77]. Important performance criteria are, for example, its fidelity and storage time. It has many applications such as storing qubits to time operations in quantum computation [78], buffer entanglement in quantum repeaters for quantum communication networks [79], or single-photon generation [77]. Stationary OHT was successfully applied to reconstruct the state of a single photon retrieved on demand from a cavity-enhanced cold atom memory [80]. Since a single photon state is intrinsically pure and uncertain in phase, there was no need for non-stationary OHT. The case is different for other types of quantum memory or different kinds of states stored, such as photon echos retrieved from semiconductor spins [81]. Here, the retrieved states are probably mixed and not necessarily phase-locked to the LO. Therefore, non-stationary OHT may provide more information.

The technology developed in this work for non-stationary OHT could also be improved and tailored to specific needs. For instance, some applications may require real-time processing with FPGAs, a more compact design for on chip quantum tomography [82], or more advanced reconstruction algorithms [83]. Moreover, the detection technology presented in this work can be applied in other applications. For example, it was already shown that it is possible to measure the two-time second-order correlation function $g^{(2)}(\tau)$ by employing two homodyne detection channels [39]. With the presented homodyne detectors, higher acquisition speeds are possible, and the setup is easily scalable to more detectors which may provide access to multitime correlation functions [84].

On the path towards optical quantum technologies deployable in industrial or personal applications, quantum tomography is an essential element in the quantum engineering toolbox. However, the ability to reconstruct quantum states alone is only the starting point for debugging photonic quantum devices. Since such devices actively process incoming quantum states, the complete characterization of quantum-optical processes occurring within these devices is another important requirement already under research [85]. For this so-called quantum-process tomography (QPT), different strategies were already developed [86]. While there are strategies that are not based on quantum tomography [87], QPT can be achieved, for example, by iteratively probing a quantum-optical "black box" with coherent states and performing stationary OHT on the output [88]. Non-stationary OHT may improve QPT on multiple fronts, replacing stationary OHT. Instead of probing the quantum process with multiple coherent states, for instance, it could be probed with a single relatively high intensity thermal light field while monitoring the output and the input with non-stationary OHT. In a single measurement run, the thermal light field provides a multitude of coherent states with different amplitudes and phases, which are probed all at once. In the following data processing step, the reconstruction of the process could be possible.

I imagine this work to contribute twofold; first, it can be a building block on the road to quantum devices enriching our lives and tackling challenges of our time. Second, it may be the basis for further fundamental research with respect to light and light-matter interaction advancing our understanding of the world.

Appendices

A. Mathematical Relations

A.1. Power Series

Limit of the infinite **geometric series** for $|x| < 1$ [70, p. 19]:

$$\sum_{k=0}^{\infty} x^k = \frac{1}{1-x} \tag{A.1}$$

The limits of two other important power series can be calculated with the help of the **differentiation rule** for uniformly convergent series [70, p. 469] that allows one to differentiate a series term-by-term. It is here applied to the geometric series to get the limit of a power series linear in k for $|x| < 1$:

$$\begin{aligned}
& \left(\sum_{k=0}^{\infty} x^k\right)' = \left(\frac{1}{1-x}\right)' \\
\Leftrightarrow \quad & \sum_{k=0}^{\infty} \left(x^k\right)' = \frac{1}{(1-x)^2} \\
\Leftrightarrow \quad & \sum_{k=1}^{\infty} k x^{k-1} = \frac{1}{(1-x)^2} \\
\Leftrightarrow \quad & \sum_{k=0}^{\infty} k x^k = \frac{x}{(1-x)^2}
\end{aligned} \tag{A.2}$$

Applying the differentiation rule to Eq. (A.2) results in the limit of a power series with a quadratic dependence on k for $|x| < 1$:

$$\sum_{k=0}^{\infty} k^2 x^k = \frac{x(1+x)}{(1-x)^3} \tag{A.3}$$

A.2. Phase Space Distribution Functions

In the following, some relations regarding the phase space distribution functions that are used in this work are given. A concise theoretical treatment of these functions was published, for instance, by Lee [89]. Complex variables are written in greek letters, while other variables are considered real. The Q-function can be computed from the Wigner

function via [89, p. 169]:

$$Q(\alpha) = \frac{2}{\pi} \int W(\beta) \exp\left(-2|\alpha - \beta|^2\right) d^2\beta \tag{A.4}$$

The Wigner function can be computed from the P-function via a similar relation [89, p. 169]:

$$W(\alpha) = \frac{2}{\pi} \int P(\beta) \exp\left(-2|\alpha - \beta|^2\right) d^2\beta \tag{A.5}$$

And the Q-function from the P-function as well [89, p. 169]:

$$Q(\alpha) = \frac{1}{\pi} \int P(\beta) \exp\left(-|\alpha - \beta|^2\right) d^2\beta \tag{A.6}$$

A.3. Integration Formulas

Integrating a Gaussian function (e.g. [26, p. 340]):

$$\int_{-\infty}^{\infty} \exp\left(-ax^2 + bx\right) dx = \sqrt{\frac{\pi}{a}} \exp\left(\frac{b^2}{4a}\right) \tag{A.7}$$

Fourier transform of an α-space function $F(\alpha)$:

$$\widetilde{F}(\widetilde{\alpha} = \widetilde{\alpha}_r + i\widetilde{\alpha}_i) = \int \int F(\alpha) \exp\left(-i\left(\widetilde{\alpha}_r \alpha_r + \widetilde{\alpha}_i \alpha_i\right)\right) d\alpha_r d\alpha_i \tag{A.8}$$

Reverse Fourier transform of an α-space function $F(\alpha)$:

$$F(\alpha) = \frac{1}{(2\pi)^2} \int \int F(\widetilde{\alpha}) \exp\left(i\left(\alpha_r \widetilde{\alpha}_r + \alpha_i \widetilde{\alpha}_i\right)\right) d\widetilde{\alpha}_r d\widetilde{\alpha}_i \tag{A.9}$$

A.4. Mathematica Computations

The following figures show computations from chapter 6 that were performed with Mathematica [69].

```
In[12]:= Q[xt_, yt_] =
          1 / (Pi^2 * (1 + n)) * Exp[-((t * xps - r * xt)^2 + (t * yps - r * yt)^2) / (1 + n)] *
           Exp[(-(r * xps + t * xt)^2 - (r * yps + t * yt)^2)]

Out[12]= e^(-(r xps+t xt)^2-(r yps+t yt)^2+(-(t xps-r xt)^2-(t yps-r yt)^2)/(1+n)) / ((1 + n) π^2)

In[13]:= Simplify[Integrate[Q[xt, yt], {xt, -Infinity, Infinity}, {yt, -Infinity, Infinity}],
          n > 0 && r > 0 && t > 0]

Out[13]= e^(-((r^2+t^2)^2 (xps^2+yps^2))/(r^2+(1+n) t^2)) / (π (r^2 + (1 + n) t^2))
```

Figure A.1.: Normalization of conditional Q-function from Eq. (6.38).

```
In[30]:= Q[xt_, yt_] = (1 + n * t^2) / (Pi * (1 + n)) * Exp[(xps^2 + yps^2) / (1 + n * t^2)] *
           Exp[-((t * xps - r * xt)^2 + (t * yps - r * yt)^2) / (1 + n)] *
           Exp[-(r * xps + t * xt)^2 - (r * yps + t * yt)^2]

Out[30]= e^(-(r xps+t xt)^2+(xps^2+yps^2)/(1+n t^2)-(r yps+t yt)^2+(-(t xps-r xt)^2-(t yps-r yt)^2)/(1+n)) (1 + n t^2) / ((1 + n) π)

In[31]:= Simplify[Integrate[Q[xt, yt] * Exp[-I (xt * xst + yt * yst)],
           {xt, -Infinity, Infinity}, {yt, -Infinity, Infinity},
           Assumptions → n > 0 && r > 0 && t > 0 && r^2 < 1 && t^2 < 1], r^2 + t^2 == 1]

Out[31]= e^(-(xst^2+yst^2+n (xst^2+yst^2-4 i r t (xps xst+yps yst)))/(4+4 n t^2))
```

Figure A.2.: Fourier transform of conditional Q-function resulting in Eq. (6.39).

```
In[32]:= Qs[xst_, yst_] = e^(-(xst^2+yst^2+n (xst^2+yst^2-4 i r t (xps xst+yps yst)))/(4+4 n t^2))

Out[32]= e^(-(xst^2+yst^2+n (xst^2+yst^2-4 i r t (xps xst+yps yst)))/(4+4 n t^2))

In[34]:= W[xt_, yt_] = 1 / (2 * Pi)^2 *
           Integrate[Qs[xst, yst] * Exp[(xst^2 + yst^2) / 8] * Exp[I * (xst * xt + yst * yt)],
            {xst, -Infinity, Infinity}, {yst, -Infinity, Infinity},
            Assumptions → n > 0 && r > 0 && t > 0 && r^2 < 1 && t^2 < 1]

Out[34]= -1/(π (-1 + n (-2 + t^2))) 2 e^((2 (xt^2+yt^2+2 n t (r (xps xt+yps yt)+t (xt^2+yt^2))+n^2 t^2 (r^2 (xps^2+yps^2)+2 r t (xps xt+yps yt)+t^2 (xt^2+yt^2))))/((1+n t^2) (-1+n (-2+t^2)))) (1 + n t^2)
```

Figure A.3.: Computation of conditional Wigner with the help of Eq. (6.36) resulting in Eq. (6.39).

```
In[1]:= W[q_, p_] = (1 + n * t^2) / (Pi * (1 + n + n * r^2)) *
          Exp[-((1 + n * t^2) * q + n * r * t * Sqrt[2] * qps)^2 / ((1 + n * t^2) * (1 + n + n * r^2))] *
          Exp[-((1 + n * t^2) * p + n * r * t * Sqrt[2] * pps)^2 / ((1 + n * t^2) * (1 + n + n * r^2))]

Out[1]= e^(-(Sqrt[2] n pps r t+p (1+n t^2))^2/((1+n+n r^2) (1+n t^2)) - (Sqrt[2] n qps r t+q (1+n t^2))^2/((1+n+n r^2) (1+n t^2))) (1 + n t^2) / (π (1 + n + n r^2))

In[2]:= Integrate[W[q, p] * q, {q, -Infinity, Infinity}, {p, -Infinity, Infinity},
         Assumptions → n > 0 && r > 0 && t > 0 && r^2 < 1 && t^2 < 1]

Out[2]= -(Sqrt[2] n qps r t)/(1 + n t^2)

In[3]:= Simplify[Integrate[W[q, p] * p, {q, -Infinity, Infinity}, {p, -Infinity, Infinity}],
         Assumptions → n > 0 && r > 0 && t > 0 && r^2 < 1 && t^2 < 1]

Out[3]= -(Sqrt[2] n pps r t)/(1 + n t^2)
```

Figure A.4.: Expectation values $\langle q \rangle$ and $\langle p \rangle$ of conditional Wigner function resulting in Eqs. (6.42) and (6.43).

```
In[1]:= W[q_, p_] = (1 + n * t^2) / (Pi * (1 + n + n * r^2)) *
          Exp[-((1 + n * t^2) * q + n * r * t * Sqrt[2] * qps)^2 / ((1 + n * t^2) * (1 + n + n * r^2))] *
          Exp[-((1 + n * t^2) * p + n * r * t * Sqrt[2] * pps)^2 / ((1 + n * t^2) * (1 + n + n * r^2))]
```

$$\text{Out[1]=}\quad \frac{e^{-\frac{\left(\sqrt{2}\ n\,pps\,r\,t+p\left(1+n\,t^2\right)\right)^2}{\left(1+n+n\,r^2\right)\left(1+n\,t^2\right)}-\frac{\left(\sqrt{2}\ n\,qps\,r\,t+q\left(1+n\,t^2\right)\right)^2}{\left(1+n+n\,r^2\right)\left(1+n\,t^2\right)}}\left(1+n\,t^2\right)}{\pi\left(1+n+n\,r^2\right)}$$

```
In[2]:= Integrate[W[q, p] * q^2, {q, -Infinity, Infinity},
          {p, -Infinity, Infinity}, Assumptions → n > 0 && r > 0 && t > 0 && r^2 < 1 && t^2 < 1]
```

$$\text{Out[2]=}\quad \frac{1+n+n\,r^2+n\left(1+n+n\left(1+4\,qps^2\right)r^2\right)t^2}{2\left(1+n\,t^2\right)^2}$$

```
In[3]:= Integrate[W[q, p] * p^2, {q, -Infinity, Infinity},
          {p, -Infinity, Infinity}, Assumptions → n > 0 && r > 0 && t > 0 && r^2 < 1 && t^2 < 1]
```

$$\text{Out[3]=}\quad \frac{1+n+n\,r^2+n\left(1+n+n\left(1+4\,pps^2\right)r^2\right)t^2}{2\left(1+n\,t^2\right)^2}$$

Figure A.5.: Expectation values $\langle q^2 \rangle$ and $\langle p^2 \rangle$ of conditional Wigner function resulting in Eqs. (6.44) and (6.45).

```
In[1]:= expQ2 = (1 + n + n r^2 + n t^2 (1 + n + n r^2 (1 + 4 qps^2))) / (2 (1 + n t^2)^2)
```

$$\text{Out[1]=}\quad \frac{1+n+n\,r^2+n\left(1+n+n\left(1+4\,qps^2\right)r^2\right)t^2}{2\left(1+n\,t^2\right)^2}$$

```
In[2]:= expQ = -(n Sqrt[2] qps r t) / (1 + n t^2)
```

$$\text{Out[2]=}\quad -\frac{\sqrt{2}\ n\,qps\,r\,t}{1+n\,t^2}$$

```
In[3]:= Simplify[expQ2 - expQ^2]
```

$$\text{Out[3]=}\quad \frac{1+n+n\,r^2}{2+2\,n\,t^2}$$

Figure A.6.: Variance $Var(q)$ of conditional Wigner function resulting in Eq. (6.46).

Bibliography

[1] Maiman, T. H. Stimulated optical radiation in ruby. *Nature* **187**, 493–494 (1960).

[2] Photonics21 - European Technology Platform. Market research study photonics 2017 (2017). URL `https://www.photonics21.org/download/ppp-services/photonics-downloads/Market-Research-Report_Photonics21_Internet.pdf`.

[3] Steen, W. & Mazumder, J. *Laser Material Processing* (Springer London, 2010).

[4] Reinstein, D. Z., Archer, T. J. & Gobbe, M. The history of LASIK. *Journal of Refractive Surgery* **28**, 291–298 (2012).

[5] Smith, D. A. *et al.* Wind lidar evaluation at the Danish wind test site in Høvsøre. *Wind Energy* **9**, 87–93 (2006).

[6] Heine, F., Muhlnikel, G., Zech, H., Philipp-May, S. & Meyer, R. The European data relay system, high speed laser based data links. In *7th Advanced Satellite Multimedia Systems Conference and the 13th Signal Processing for Space Communications Workshop (ASMS/SPSC)* (IEEE, 2014).

[7] QUTE-EUROPE. Quantum manifesto - a new era of technology (2016). URL `https://qt.eu/app/uploads/2018/04/93056_Quantum-Manifesto_WEB.pdf`.

[8] Riedel, M. F., Binosi, D., Thew, R. & Calarco, T. The European quantum technologies flagship programme. *Quantum Science and Technology* **2**, 030501 (2017).

[9] O'Brien, J. L., Furusawa, A. & Vučković, J. Photonic quantum technologies. *Nature Photonics* **3**, 687–695 (2009).

[10] Kok, P. & Lovett, B. W. *Introduction to Optical Quantum Information Processing* (Cambridge University Press, New York, 2010).

[11] Lo, H.-K., Curty, M. & Tamaki, K. Secure quantum key distribution. *Nature Photonics* **8**, 595–604 (2014).

[12] Raymer, M. G. & Beck, M. *Quantum State Estimation*, chap. Experimental quantum state tomography of optical fields and ultrafast statistical sampling, 235–295 (Springer-Verlag, Berlin, 2004).

[13] Banaszek, K., Cramer, M. & Gross, D. Focus on quantum tomography. *New Journal of Physics* **15**, 125020 (2013).

[14] Lvovsky, A. I. & Raymer, M. G. Continuous-variable optical quantum-state tomography. *Reviews of Modern Physics* **81**, 299–332 (2009).

[15] Abbott, B. *et al.* Observation of gravitational waves from a binary black hole merger. *Physical Review Letters* **116**, 061102 (2016).

[16] Leonhardt, U. & Paul, H. Measuring the quantum state of light. *Progress in Quantum Electronics* **19**, 89–130 (1995).

[17] Raimond, J. M., Brune, M. & Haroche, S. Reversible decoherence of a mesoscopic superposition of field states. *Physical Review Letters* **79**, 1964–1967 (1997).

[18] Ourjoumtsev, A., Jeong, H., Tualle-Brouri, R. & Grangier, P. Generation of optical 'schrödinger cats' from photon number states. *Nature* **448**, 784–786 (2007).

[19] Siegman, A. E. *Lasers* (University Science Books, Mill Valley, California, 1986).

[20] Nolting, W. *Theoretical Physics 3* (Springer International Publishing, Switzerland, 2016).

[21] Fox, M. *Quantum Optics: An Introduction* (Oxford University Press, New York, 2006).

[22] Mohr, P. J., Newell, D. B. & Taylor, B. N. CODATA recommended values of the fundamental physical constants: 2014. *Reviews of Modern Physics* **88**, 035009 (2016).

[23] Boutet, E. Onda electromagnética (2007, CC-BY-SA-3.0). URL `https://commons.wikimedia.org/wiki/File:Onde_electromagnetique.svg`.

[24] Schawlow, A. L. & Townes, C. H. Infrared and optical masers. *Physical Review* **112**, 1940–1949 (1958).

[25] Dirac, P. A. M. *The Principles of Quantum Mechanics* (Oxford University Press, Oxford, 1947), third edn.

[26] Schleich, W. P. *Quantum Optics in Phase Space* (Wiley-VCH, Berlin, 2001), first edn.

[27] Heisenberg, W. Über den anschaulichen Inhalt der quantentheoretischen Kinematik und Mechanik. *Zeitschrift für Physik* **43**, 172–198 (1927).

[28] Bellac, M. L. *Quantum Physics* (Cambridge University Press, New, York, 2006).

[29] Nolting, W. *Theoretical Physics 6* (Springer International Publishing, Switzerland, 2017).

[30] Nolting, W. *Theoretical Physics 8* (Springer International Publishing, Switzerland, 2018).

[31] Wigner, E. On the quantum correction for thermodynamic equilibrium. *Physical Review* **40**, 749–759 (1932).

[32] Schrödinger, E. Der stetige Übergang von der Mikro- zur Makromechanik. *Die Naturwissenschaften* **14**, 664–666 (1926).

[33] Vogel, K. & Risken, H. Determination of quasiprobability distributions in terms of probability distributions for the rotated quadrature phase. *Physical Review A* **40**, 2847–2849 (1989).

[34] Smithey, D. T., Beck, M., Raymer, M. G. & Faridani, A. Measurement of the Wigner distribution and the density matrix of a light mode using optical homodyne tomography: Application to squeezed states and the vacuum. *Physical Review Letters* **70**, 1244–1247 (1993).

[35] Yuen, H. P. & Chan, V. W. S. Noise in homodyne and heterodyne detection. *Optics Letters* **8**, 177 (1983).

[36] Abbas, G. L., Chan, V. W. S. & Yee, T. K. Local-oscillator excess-noise suppression for homodyne and heterodyne detection. *Optics Letters* **8**, 419 (1983).

[37] Ou, Z. Y. & Mandel, L. Derivation of reciprocity relations for a beam splitter from energy balance. *American Journal of Physics* **57**, 66–67 (1989).

[38] Raymer, M. G., Cooper, J., Carmichael, H. J., Beck, M. & Smithey, D. T. Ultrafast measurement of optical-field statistics by dc-balanced homodyne detection. *Journal of the Optical Society of America B* **12**, 1801 (1995).

[39] Roumpos, G. & Cundiff, S. T. Multichannel homodyne detection for quantum optical tomography. *Journal of the Optical Society of America B* **30**, 1303 (2013).

[40] Lvovsky, A. I. Iterative maximum-likelihood reconstruction in quantum homodyne tomography. *Journal of Optics B: Quantum and Semiclassical Optics* **6**, S556–S559 (2004).

[41] Pérez-Jordá, J. M. On the recursive solution of the quantum harmonic oscillator. *European Journal of Physics* **39**, 015402 (2017).

[42] Thewes, J. & Lüders, C. Matlab toolbox for quantum state tomography (2018). URL `https://doi.org/10.5281/zenodo.1480298`.

[43] Kumar, R. *et al.* Versatile wideband balanced detector for quantum optical homodyne tomography. *Optics Communications* **285**, 5259–5267 (2012).

[44] Sibbett, W., Lagatsky, A. A. & Brown, C. T. A. The development and application of femtosecond laser systems. *Optics Express* **20**, 6989 (2012).

[45] Hamamatsu Photonics K.K., Solid State Division. *Datasheet for S5971, S5972, and S5973 Series Si PIN Photodiodes* (2015). URL `https://www.hamamatsu.com/resources/pdf/ssd/s5971_etc_kpin1025e.pdf`.

[46] Kallner, A. Formulas. In *Laboratory Statistics*, 1–119 (Elsevier, 2014).

[47] Landi, G. & Zampini, A. *Linear Algebra and Analytic Geometry for Physical Sciences* (Springer International Publishing, Switzerland, 2018).

[48] Lüders, C., Thewes, J. & Aßmann, M. Real time g(2) monitoring with 100 kHz sampling rate. *Optics Express* **26**, 24854 (2018).

[49] Magde, D., Elson, E. & Webb, W. W. Thermodynamic fluctuations in a reacting system—measurement by fluorescence correlation spectroscopy. *Physical Review Letters* **29**, 705–708 (1972).

[50] Kimble, H. J., Dagenais, M. & Mandel, L. Photon antibunching in resonance fluorescence. *Physical Review Letters* **39**, 691–695 (1977).

[51] Brown, R. H. & Twiss, R. Q. A test of a new type of stellar interferometer on sirius. *Nature* **178**, 1046–1048 (1956).

[52] Ulrich, S. M. *et al.* Photon statistics of semiconductor microcavity lasers. *Physical Review Letters* **98**, 043906 (2007).

[53] Boitier, F., Godard, A., Rosencher, E. & Fabre, C. Measuring photon bunching at ultrashort timescale by two-photon absorption in semiconductors. *Nature Physics* **5**, 267–270 (2009).

[54] Hayat, A., Nevet, A. & Orenstein, M. Ultrafast partial measurement of fourth-order coherence by HBT interferometry of upconversion-based autocorrelation. *Optics Letters* **35**, 793 (2010).

[55] Aßmann, M., Veit, F., Bayer, M., van der Poel, M. & Hvam, J. M. Higher-order photon bunching in a semiconductor microcavity. *Science* **325**, 297–300 (2009).

[56] Gray, G. R. & Roy, R. Bistability and mode hopping in a semiconductor laser. *Journal of the Optical Society of America B* **8**, 632 (1991).

[57] Aßmann, M. *et al.* Ultrafast tracking of second-order photon correlations in the emission of quantum-dot microresonator lasers. *Physical Review B* **81**, 165314 (2010).

[58] Wang, T., Puccioni, G. P. & Lippi, G. L. Dynamical buildup of lasing in mesoscale devices. *Scientific Reports* **5**, 15858 (2015).

[59] Albert, F. *et al.* Observing chaos for quantum-dot microlasers with external feedback. *Nature Communications* **2**, 366 (2011).

[60] Jahnke, F. *et al.* Giant photon bunching, superradiant pulse emission and excitation trapping in quantum-dot nanolasers. *Nature Communications* **7**, 11540 (2016).

[61] Leymann, H. A. M. *et al.* Intensity fluctuations in bimodal micropillar lasers enhanced by quantum-dot gain competition. *Physical Review A* **87**, 053819 (2013).

[62] Wootters, W. K. & Zurek, W. H. A single quantum cannot be cloned. *Nature* **299**, 802–803 (1982).

[63] Husimi, K. Some formal properties of the density matrix. *Proceedings of the Physico-Mathematical Society of Japan. 3rd Series* **22**, 264–314 (1940).

[64] Kano, Y. A new phase-space distribution function in the statistical theory of the electromagnetic field. *Journal of Mathematical Physics* **6**, 1913–1915 (1965).

[65] Glauber, R. J. Photon correlations. *Physical Review Letters* **10**, 84–86 (1963).

[66] Sudarshan, E. C. G. Equivalence of semiclassical and quantum mechanical descriptions of statistical light beams. *Physical Review Letters* **10**, 277–279 (1963).

[67] Walker, N. & Carroll, J. Simultaneous phase and amplitude measurements on optical signals using a multiport junction. *Electronics Letters* **20**, 981 (1984).

[68] Walker, N. G. & Carroll, J. E. Multiport homodyne detection near the quantum noise limit. *Optical and Quantum Electronics* **18**, 355–363 (1986).

[69] Wolfram Research, Inc. Mathematica, Version 11.2. Champaign, IL, 2017.

[70] Bronshtein, I., Semendyayev, K., Musiol, G. & Mühlig, H. *Handbook of Mathematics* (Springer-Verlag, Berlin, Heidelberg, 2015).

[71] Mandel, L. & Wolf, E. *Optical coherence and quantum optics* (Cambridge University Press, New York, 1995).

[72] Huang, D., Fang, J., Wang, C., Huang, P. & Zeng, G.-H. A 300-MHz bandwidth balanced homodyne detector for continuous variable quantum key distribution. *Chinese Physics Letters* **30**, 114209 (2013).

[73] Ishizawa, A. *et al.* Phase-noise characteristics of a 25-GHz-spaced optical frequency comb based on a phase- and intensity-modulated laser. *Optics Express* **21**, 29186 (2013).

[74] Endo, M., Ito, I. & Kobayashi, Y. Direct 15-GHz mode-spacing optical frequency comb with a kerr-lens mode-locked yb:y2o3 ceramic laser. *Optics Express* **23**, 1276 (2015).

[75] Mangold, M. *et al.* Pulse repetition rate scaling from 5 to 100 GHz with a high-power semiconductor disk laser. *Optics Express* **22**, 6099 (2014).

[76] Munroe, M., Boggavarapu, D., Anderson, M. E. & Raymer, M. G. Photon-number statistics from the phase-averaged quadrature-field distribution: Theory and ultrafast measurement. *Physical Review A* **52**, R924–R927 (1995).

[77] Lvovsky, A. I., Sanders, B. C. & Tittel, W. Optical quantum memory. *Nature Photonics* **3**, 706–714 (2009).

[78] Kok, P. *et al.* Linear optical quantum computing with photonic qubits. *Reviews of Modern Physics* **79**, 135–174 (2007).

[79] Sangouard, N., Simon, C., de Riedmatten, H. & Gisin, N. Quantum repeaters based on atomic ensembles and linear optics. *Reviews of Modern Physics* **83**, 33–80 (2011).

[80] Bimbard, E. *et al.* Homodyne tomography of a single photon retrieved on demand from a cavity-enhanced cold atom memory. *Physical Review Letters* **112**, 033601 (2014).

[81] Langer, L. *et al.* Access to long-term optical memories using photon echoes retrieved from semiconductor spins. *Nature Photonics* **8**, 851–857 (2014).

[82] Raffaelli, F. *et al.* A homodyne detector integrated onto a photonic chip for measuring quantum states and generating random numbers. *Quantum Science and Technology* **3**, 025003 (2018).

[83] Shang, J., Zhang, Z. & Ng, H. K. Superfast maximum-likelihood reconstruction for quantum tomography. *Physical Review A* **95**, 062336 (2017).

[84] Heuer, A. Information content of multitime correlation functions for the interpretation of structural relaxation in glass-forming systems. *Physical Review E* **56**, 730–740 (1997).

[85] Lobino, M. *et al.* Complete characterization of quantum-optical processes. *Science* **322**, 563–566 (2008).

[86] Mohseni, M., Rezakhani, A. T. & Lidar, D. A. Quantum-process tomography: Resource analysis of different strategies. *Physical Review A* **77**, 032322 (2008).

[87] da Silva, M. P., Landon-Cardinal, O. & Poulin, D. Practical characterization of quantum devices without tomography. *Physical Review Letters* **107**, 210404 (2011).

[88] Anis, A. & Lvovsky, A. I. Maximum-likelihood coherent-state quantum process tomography. *New Journal of Physics* **14**, 105021 (2012).

[89] Lee, H.-W. Theory and application of the quantum phase-space distribution functions. *Physics Reports* **259**, 147–211 (1995).

List of Publications

(1) J. Thewes, C. Lüders, and M. Aßmann.

Non-stationary optical homodyne quantum state tomography reveals hidden dynamics of light fields.

Submitted.

(2) C. Lüders, J. Thewes, and M. Aßmann.

Real time $g^{(2)}(0)$ monitoring with 100 kHz sampling rate.

Optics Express **26**, 24854 (2018).

(3) M. Aßmann, J. Thewes, D. Fröhlich, and M. Bayer.

Quantum chaos and breaking of all anti-unitary symmetries in Rydberg excitons.

Nature Materials **15**, 741-745 (2016).

(4) J. Thewes, J. Heckötter, T. Kazimierczuk, M. Aßmann, D. Fröhlich, M. Bayer, M. A. Semina, and M. M. Glazov.

Observation of high angular momentum excitons in cuprous oxide.

Physical Review Letters **115**, 027402 (2015).

(5) F. Schöne, S.-O. Krüger, P. Grünwald, H. Stolz, S. Scheel, M. Aßmann, J. Heckötter, J. Thewes, D. Fröhlich, and M. Bayer.

Deviations of the exciton level spectrum in Cu_2O from the hydrogen series.

Physical Review B **93**, 075203 (2016).

(6) F. Schöne, S.-O. Krüger, P. Grünwald, M. Aßmann, J. Heckötter, J. Thewes, H. Stolz, D. Fröhlich, M. Bayer, and S. Scheel.

Coupled valence band dispersions and the quantum defect of excitons in Cu_2O.

Journal of Physics B: Atomic, Molecular and Optical Physics **49**, 134003 (2016).

(7) J. Heckötter, J. Thewes, D. Fröhlich, M. Aßmann, and M. Bayer.

Landau-level quantization of the yellow excitons in cuprous oxide.

Physics of the Solid State **60**, 1625-1628 (2018).

Acknowledgments

Finally, I want to thank everyone who supported me during the years leading up to the creation of this thesis.

I would like to thank Jun.-Prof. Dr. Marc Aßmann, who gave me the opportunity to work on the quantum state tomography research project and encouraged me to pursue my own paths, and Prof. Dr. Manfred Bayer for introducing me to E2. Further, I want to thank Prof. Alexander Lvovsky, Ph. D., for the fruitful discussions about high bandwidth homodyne detection. Also, many thanks to my former master student Carolin Lüders, who is always eager to learn and ready to contribute with high quality, and my former bachelor student Lea Platzbecker for the collaboration.

I am grateful to all current and former members of E2 for the great atmosphere at work and their willingness to help. In particular, I appreciated the jokes and discussions with my office colleagues Alexey Danilov, Bernd Berger, Daniel Schmidt, Walter Warkentin, and Pavel Sokolov keeping up our motivation. Special thanks for the perfect administrative support to Michaela Wäscher, Nina Collette, and Katharina Sparka, for the fast help with electrical and mechanical issues to Thomas Stöhr, Lars Wieschollek, and the scientific workshops, and for access to liquid nitrogen and helium to Klaus Wiegers and Daniel Tüttmann.

Furthermore, I like to thank Dennis Kudlacik, Nicole Appel, and Jan Freiwald for proofreading. My special gratitude goes to my family and friends, especially to my girlfriend Lena and to my parents Therese and Elmar, supporting me throughout all ups and downs of life.

Thank you very much!